Charge Dynamics in Hybrid and Organic-Inorganic Light Harvesting Thin Films followed with Femtosecond Transient Absorption Spectroscopy

by

Iulia Minda

Thesis presented in partial fulfilment of the requirements for the degree of

Doctor of Philosophy

at the University of Stellenbosch

Supervisor:

Prof. Heinrich Schwoerer

December 2017

Declaration

By submitting this dissertation electronically, I declare that the entirety of the work contained therein is my own, original work, that I am the sole author thereof (save to the extent explicitly otherwise stated), that reproduction and publication thereof by Stellenbosch University will not infringe any third party rights and that I have not previously in its entirety or in part submitted it for obtaining any qualification.

Date: December 2017

Abstract

In order to bridge the gap between traditional sources of electricity and the increasing global demand for it, as a society we must move towards renewable sources of energy such as solar radiation. Photovoltaic devices (PVs) harness solar power and convert it to electrical power. In order to be commercially viable, they need to be efficient, cost effective, simple to fabricate and environmentally friendly. To address these requirements, the class of emerging PVs arose, which includes dye sensitised solar cells (DSSCs) and perovskite solar cells. Femtosecond transient absorption spectroscopy (TAS) is an experimental technique which allows us to follow the ultrafast photoinduced charge dynamics in real time in light harvesting thin films and PVs. By assigning time and rate constants to various processes governing the charge generation and extraction in solar cells, we construct charge dynamics models, and therefore learn the fundamental photophysics reasons behind what makes the power conversion efficiencies (PCEs) of some solar cells superior. In particular, this study focused on the charge transfer processes in indoline dye (DN216) sensitised electrodeposited ZnO solar cells, and the charge recombination dynamics in $FA_{0.85}MA_{0.15}PbI_{2.55}Br_{0.45}$ perovskite thin films. To construct the simplest fully consistent charge dynamics models, we match the visible and near-infrared spectroscopic signals of our samples to the allowed electronic transitions, and follow their temporal evolutions on the femtosecond and picosecond time scales. From our measured time and rate constants we observed that ZnO based DSSCs are less efficient than their TiO_2 counterparts because the electron injection from the photoexcited indoline dye into the ZnO CB doesn't just occur directly (< 200 fs), but also stepwise via neutral (~ 2 ps) and ionic (~ 10 ps) intermediate charge transfer states, resulting from surface trap states characteristic of electrodeposited ZnO. Moreover, $FA_{0.85}MA_{0.15}PbI_{2.55}Br_{0.45}$ is an excellent hybrid photoabsorber in record efficiency perovskite solar cells because even at high charge carrier densities of 10^{19} cm^{-3}, the third order non-radiative Auger recombination mechanism is not dominant. Furthermore we determined the associated geminate, non-geminate and Auger recombination rate constants as $A = 5 \times 10^{9}$ s^{-1}, $B = 10^{-10}$ $s^{-1}cm^{3}$ and $C = 50 \times 10^{-32}$ $s^{-1}cm^{6}$.

Opsomming

Die gaping tussen tradisionele bronne van elektrisiteit en die aanvraag daarvoor moet oorbrug word, as 'n wêreld gemeenskap moet ons beweeg in die rigting van herwinbare energie bronne soos son krag. Fotovoltaïse toestelle (PVs) omskep son krag na elektriese krag. Om ekonomies vatbaar te wees, moet hulle effektief, koste effektief en eenvoudig wees om te vervaardig in 'n omgewings vriendelike manier. Om hierdie vereistes aan te spreek het 'n klas PVs ontstaan waaronder kleursel-gesensiteerde-sonselle (DSSCs) en perovskiet son-selle val. Femtosekonde leeftyd absorpsie spektroskopie (TAS) is 'n eksperimentele tegniek wat ons toelaat om die super vinnige foto-geinduseerde dinamika soos dit plaas vind in lig opnemende dun film materiaal waar te neem. Deur leeftyds konstante waardes toe te ken vir die verskillende prosesse wat by dra tot ladings generasie en ekstraksie in son-selle kan ons dinamiese modelle saam te stel om sodoende iets te leer oor die fundamentele fotofisika agter die sonsel kragopwekking effektiwiteit (PCEs). In hierdie studie het ons meer spesifiek gefokus op die ladings-oordrag prosesse van indolien kleursel (DN216) gesensiteerde sink elektrolities gedeponeerde son-selle sowel as die ladings herkombinasie dinamika in $FA_{0.85}MA_{0.15}PbI_{2.55}Br_{0.45}$ perofskiet dun films. Om sodanig die eenvoudigste heeltemal konsistente ladings dinamika modelle op te stel vind ons die ooreenkomstige sigbare en naby-infrarooi spektroskopiese seine van ons monsters wat korrek vir die toelaatbare elektroniese transisies is en volg hulle evolusie in tyd op 'n femtosekonde tydskaal. Vanaf ons gemete tyd konstantes neem ons waar dat ZnO gebaseerde DSSCs minder effektief is as TiO_2 omdat die elektron inspuiting vanaf die foto-opgewekte indolien kleursel na die ZnO CB nie net direk plaas vind (< 200 fs), maar ook stapsgewys via natuurlike (~ 2 ps) en ioniese (~ 10 ps) interim ladings oordrag toestande as gevolg van die oppervlak vasvang toestand eienskappe van elektronies gedeponeerde ZnO. Verder ook, $FA_{0.85}MA_{0.15}PbI_{2.55}Br_{0.45}$ is 'n uitstekende hibriede fotoabsorbeerder in rekord effektiwiteit perovskiet son-selle omdat selfs by hoër ladingsdraer digthede van 10^{19} cm^{-3} is die nie-stralende Auger herkombinasie meganisme dominant. Verder het ons ook vasgestel dat die geassosieerde geminatus, nie-geminatus en Auger herkombinasie tyd konstantes $A = 5 \times 10^9$ s^{-1}, $B = 10^{-10}$ $s^{-1}cm^3$ en $C = 50 \times 10^{-32}$ $s^{-1}cm^6$ is.

Acknowledgements

My first thank you is towards Prof. Heinrich Schwoerer, my supervisor. Your guidance over the last five years has lead to who I am as a researcher. Your drive and love for experimental physics is something we all admire. Thank you for welcoming us all into your mind and into your family. It is because of you that I can call myself a laser physicist.

Thank you to Prof. Derck Schlettwein and the entire research group at Justus-Liebig University. You have always made me feel welcome. Christoph and Jonas, especially, thank you for all the samples over the years and always answering my many questions.

I would especially like to thank current and past members of the ultrafast transient absorption research group, Egmont, Gabriele, Essraa, Xavier and Neway - this work was truly a group effort. Gabriele, thank you for helping me with my project long after it was no longer your responsibility.

The people which make up the Stellenbosch University Physics department - over the last 9 years this has been my home. You have been both my teachers and my friends.

Thank you to the National Research Foundation (NRF) and the South African Research Chair Initiative for the financial assistance supporting this project.

Finally, thank you to my family for teaching me to believe that I could do whatever it was that I set my mind to. Thank you to my parents for encouraging me to follow a passion in life rather than a job. I appreciate you and the many prayers over the years. Thank you God for this wonderful journey. To my husband Charlie, my biggest fan, thank you for the hours you spent proof reading my work and listening to me ramble off about renewable energy, solar cells and charge transfer models. Your belief in me is unmatched.

Jonah and Mila, this thesis is for you. You can become whatever it is you set your hearts on.

Contents

1. Motivation

As time progresses, mankind's dependence on technology continues to grow, resulting in an increased energy consumption. Our current heavy reliance on the limited availability of fossil fuels to meet our energy needs, is having a negative effect on the planet as a whole. Their regeneration timescales are unrealistic for human demand and the byproducts produced upon the consumption of fossil fuels for energy have been shown to play a dominant role in climate change and global warming. As an increasing number of facets of our lives rely on interaction with the digital world, it is unreasonable to expect that our overall energy consumption would decrease or even plateau. We must therefore adapt to the demand and instead seek alternate energy sources which are naturally replenished on a reasonable timescale, environmentally friendly as well as abundant and simple to implement.

Some examples of renewable energy sources include wind, waves and tides, geothermal heat and the sun. Of these examples, solar energy is mostly independent of the geographical location where it can be harnessed and its abundance far surpasses our current energy requirements. Photovoltaic devices are employed to harness the solar energy available to us and convert it to electrical energy. Currently, silicon based solar cells dominate the commercial photovoltaic market, however their high costs and difficulty of manufacturing have opened the way for a class of emerging photovoltaics such as dye sensitised, organic, inorganic, perovskite and quantum dot solar cells. These devices, although not as efficient, are cost effective and simple to fabricate on large scales without requiring large energies to do so.

The development of photovoltaic devices towards higher power conversion efficiencies and lower costs has been at the focus of many research institutes and laboratories, and includes synthesising new materials or bettering the ones which are currently in use and altering the device architectures. The approach of material scientists and engineers is to permutate the chemical composition of the various materials employed and optimise the cells which show the greatest promise in terms of long term stability and efficiency.

In parallel, spectroscopic measurement techniques allow us to observe the behaviour of these materials from a microscopic point of view and learn about the physics and chemistry processes responsible for their response to illumination. We are therefore able to follow the charge generation and dynamics occurring on an ultrafast timescale and identify the mechanism behind the conversion of solar energy to electrical energy. Knowing the fundamental physics which underpins the charge extraction process is of great value towards the improvement of photovoltaic materials and thus solar cell devices.

However, spectroscopic measurements are extremely time consuming in comparison to electrochemical characterisation of the devices and therefore cannot be employed in real time during the synthesis of new materials. With that said, the fun-

damental limit to power conversion efficiencies is determined through these measurements, and therefore an understanding of the reasons behind a given material's performance in a photovoltaic device. This knowledge can then be employed toward the synthesis of novel photovoltaic materials and device architectures.

Therefore, our basis for selecting a material to investigate spectroscopically, either lies with its high efficiency and stability within a solar cell device or rather due to its interesting electronic properties and unique fundamental physics processes.

In particular, we employed femtosecond transient absorption spectroscopy (TAS) to investigate the photoinduced charge dynamics of photoabsorbing materials and solar cell devices. Our attention was focused on the electron transfer processes which are characteristic to fully operational indoline dye sensitised electrodeposited ZnO solar cells due to its versatility and ease of fabrication. Furthermore we studied, in detail, the recombination dynamics occurring in formamidinium methylammonium mixed halide perovskite thin films, due to the high efficiencies obtained when employed as a photoabsorber in solar cells.

This measurement technique enables us to monitor the population and depopulation dynamics of electronic states in a material upon illumination, as long as the material in question has spectroscopic signatures in the visible and infrared spectral regions. These signatures include excited state absorption, ground state bleaching, or fluorescence and correspond to electronic transitions within the material. By following the temporal evolution of the aforementioned spectroscopic signals, we were able to observe the ultrafast changes in transmission in real time and assign rate constants to well known and previously unknown processes. We achieved this through the comparison of the lifetimes of states among themselves, as well as with respect to known spectroscopic signatures associated to the transitions.

Additionally, with the use of femtosecond transient absorption spectroscopy, we identified new electronic states from their transient behaviours which were not previously known prior to this work, and were able to directly determine their role in charge transfer dynamics.

Although TAS is a small window into the particulars of charge generation, recombination and extraction, the technique provides valuable information about the charge dynamics dominating early times following illumination of photoabsorbing materials and complete solar cells. With this information, better suited materials and more efficient devices can potentially be engineered.

In this work, emerging solar cell technologies are introduced together with the materials which constitute them and their associated electronic characteristics. Using TAS in an optical ultrashort pump – broadband probe architecture, the initial photophysics occurring in the above mentioned materials was investigated and is discussed together with kinetic models pertaining to the flow of charge carries in the perovskite photoabsorbers and the indoline dye sensitised solar cells. The photophysics knowledge presented aims to serve as a scientific contribution towards the development of more efficient solar cells in order to provide cheaper clean energy with a minimal footprint on planet.

2. Introduction to Emerging Solar Cells

The average rate at which the Sun's electromagnetic radiation falls incident on the plane perpendicular to the direction of the light propagation is 1.37 kilowatts per square meter [1]. This value is conventionally referred to as the solar constant, however fluctuating with the Earth's distance from the Sun as well as atmospheric conditions. Photovoltaic devices were developed to harness the Sun's abundant radiation (solar radiation spectrum shown in Figure 2.1) and convert it to electrical energy. With a back of an envelope calculation, Hagfeldt *et al.* estimated an approximate 60 TW of power which can be generated with the use of solar farms, assuming 10% efficiency [2]. Therefore, with the implementation of photovoltaics on a large scale, the majority of the world's electricity needs could be met. Theoretically, solar farms operating at below 20% efficiency and covering less than 10% of the total area of the Sahara dessert could supply the Earth's primary electricity demand [3].

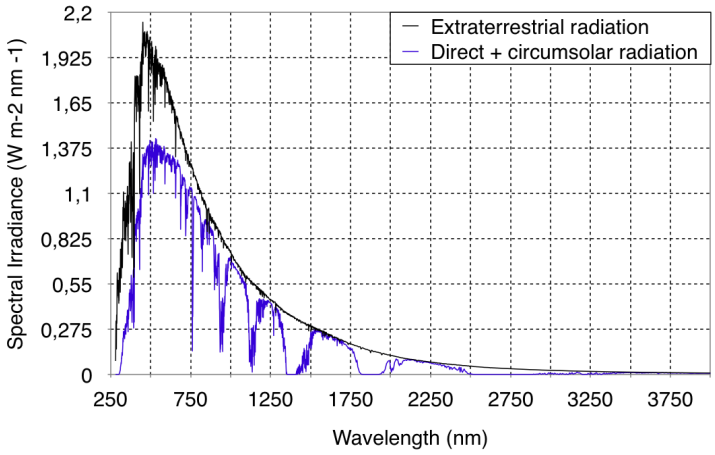

Figure 2.1: A graph of the solar irradiation spectrum plotted as spectral irradiance ($Wm^{-2}nm^{-1}$) as a function of the associated wavelength of the incident photons. The line in black shows the extraterrestrial radiation, while the direct and circumsolar radiation is depicted in blue. The data was obtained from the National Renewable Energy Laboratory website [4]. We therefore need to develop absorbers for photovoltaics with absorption maxima in the visible and near infrared spectral regions.

2.1 Power conversion efficiency

To date, a large number of photovoltaic technologies have been established and can be subclassed as first, second and third generation solar cells depending on their device architectures and introduction into the commercial photovoltaic market. First generation solar cells are fully commercialised and are based on either single crystalline

or multicrystalline silicon wafers. The second generation solar cells are identified by thin film technologies and are not yet fully integrated into the photovoltaic market. Finally, the emerging solar cell technologies are novel, not yet fully commercialised, and are classified as third generation photovoltaics, including concentrator and organic-inorganic solar cells [5].

Photovoltaic devices are constantly being developed to further increase their power conversion efficiencies (PCEs) as well as long term stabilities in ambient conditions [6]. The PCE (η) of a device is calculated as the ratio of generated electrical power (P_{max}) to incident light power (P_{in}). It is determined from the curve of extracted photocurrent density versus applied voltage of a solar cell device under constant illumination (I-V curve), according to $\eta = \frac{J_{SC} \times V_{OC} \times ff}{P_{in}}$ where J_{SC} is the short circuit current density (maximum current produced by the cell), V_{OC} is the open circuit voltage (maximum voltage extracted from the cell) and ff is the fill factor [2]. Please refer to Figure 2.2 for a graphical representation of the solar cell efficiency measurement. The fundamental restriction to solar cell efficiency is determined by the Shockley-Queisser limit [5, 7]. This limit considers that the absorption of a single photon yields one electron hole pair with a given energy separation, characteristic to the photoabsorbing material bandgap or absorption maximum. All excess photon energy with respect to this energy separation is assumed to be lost thermally, while photons with insufficient energy are not absorbed at all. To overcome this quantum defect, third generation multi junction solar cell devices were developed, such as tandem and multi-band photovoltaics [8].

Record research-cell efficiencies are reported regularly by *Progress in Photovoltaics* and the National Renewable Energy Laboratory [9, 10]. While this includes all categories of solar cell devices of a 1 cm^2 area which are illuminated under one sun conditions (AM1.5 global solar radiation, 1 kWm^{-2}), this work will only introduce some of these state of the art devices and focus primarily on dye sensitised and perovskite solar cells.

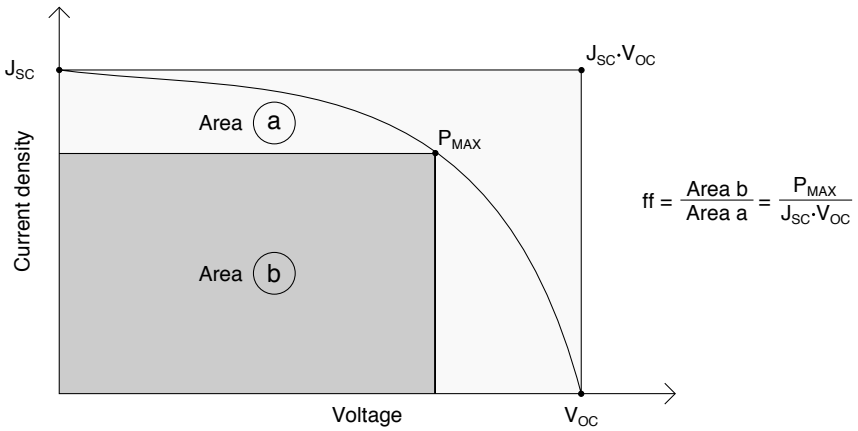

Figure 2.2: A schematic depicting a typical I-V curve associated to a solar cell as obtained under one sun conditions (AM1.5 global solar radiation, 1 kWm^{-2}). The current density is plotted as a function of the applied voltage. The short circuit current (J_{SC}) and open circuit voltage (V_{OC}) points are marked on the sketch together with their product, as well as the maximum power (P_{MAX}). The graphical calculation of the fill factor is shown as the ratio between the areas b and a, as depicted in the sketch, equivalent to the ratio of the generated electrical power to the product of maximum current and voltage.

Although the attention of the scientific community is shifting towards emerging photovoltaic devices, crystalline silicon solar cells are to date the market dominating

photovoltaics. Their success can be attributed to high PCEs exceeding 25%, abundance of silicon and long term device stabilities [9, 11]. Furthermore, multijunction solar cells with and without concentrators currently provide the best research-cell efficiencies (Figure 2.3) [10].

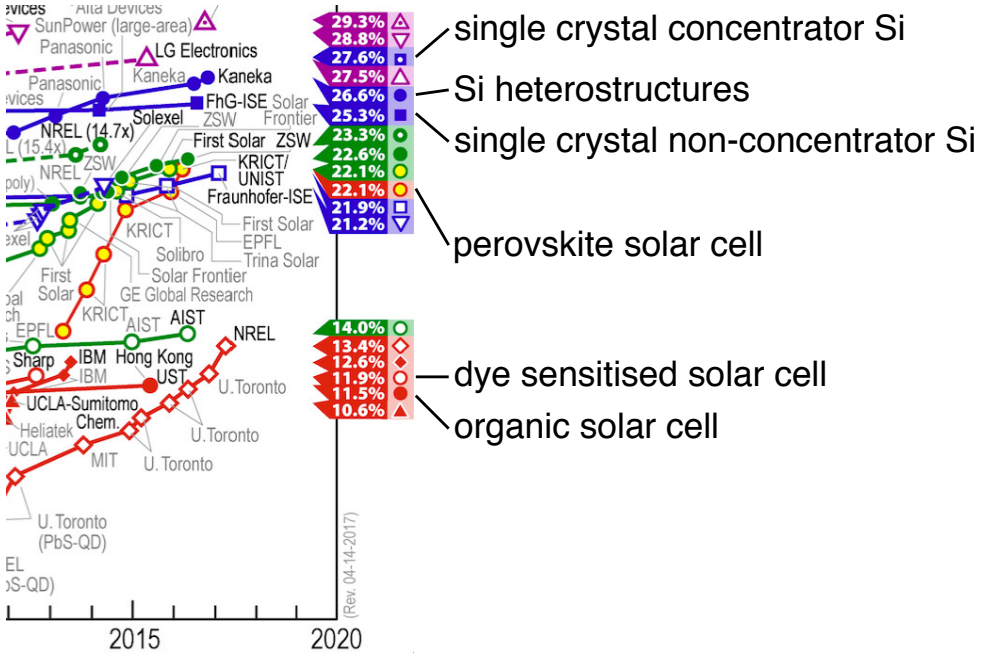

Figure 2.3: An excerpt of the best research-cell efficiencies table published by the National Renewable Energy Laboratory [10]. The graph depicts the record power conversion efficiencies obtained for various emerging solar cells versus the year in which the records were achieved. The emerging solar cell devices introduced in this work are pointed out together with the commercially available silicon solar cell technologies, for comparison.

2.2 Silicon solar cells

In general, the working principle of solar cells consists of the absorption of light, followed by efficient charge separation and transport within the photoabsorbing material. Alternatively, charge separation may require a physical interface between two materials, in which case charge transport occurs within either an electron (ETM) or hole (HTM) transport material. The extraction of charges is then facilitated by two electrodes thus producing a current in the external circuit, see Figure 2.4. In the case of fully inorganic silicon based solar cells, an electron hole pair is generated in the depletion zone upon illumination (panel a). Due to the difference in potential energy, the electron and hole diffuse to the n- and p-type materials respectively, from which they are extracted into the external circuit [12]. The maximum voltage which can be obtained from these devices is determined by the energetic separation between the conduction band (CB) of the n-type material and the valence band (VB) of the p-type material, and is approximately 0.7 V for crystalline silicon solar cells, to be compared with the Si bandgap of 1.1 eV, demonstrating the intrinsic unavoidable loss of efficiency [9].

Although silicon based solar cells are currently the most common commercially, their drawbacks include high energy and monetary cost of manufacturing. This re-

sults in long energy payback times of approximately 2 years [2]. Additionally, rigid substrates are required to support the single crystals, further increasing the cost and reducing the versatility and portability of the devices. The category of emerging photovoltaic devices arose to address these drawbacks as well as open up the absorption of solar cells further into the infrared spectral region [12]. Some examples of emerging photovoltaics include fully organic, organic-inorganic and hybrid solar cells. An advantage is that they can be solution deposited, vapour deposited, electrodeposited and even roll-to-roll printed at low temperatures on flexible substrates such as polymers or fabrics. The energy payback times of these devices are considerably shorter than that of their silicon based counterparts, and are often less than 1 year [2]. Moreover, their light weights together with the ability to deposit these photovoltaics as sandwich cells onto flexible plastic surfaces has opened a wide range of applications in terms of portable and integrated electricity generating devices.

2.3 Organic solar cells

Fully organic solar cells were not investigated in this work, however they form a large portion of emerging photovoltaics and were a building block towards the development of perovskite solar cells. They will therefore be introduced, although only briefly. The working principle of organic solar cells requires two materials: an electron donor, usually a low bandgap polymer or dye, and an electron acceptor, which is most often a fullerene derivative [13, 14]. Conventionally the donor material is employed as the photoabsorber, and its absorption maximum is chemically tuned towards the near infrared spectral region through the introduction of various ligands. Although this facilitates the harvesting of lower energy photons, the tradeoff lies with a higher quantum defect and therefore a lower maximum photocurrent density [12].

Upon illumination, an exciton (Coulombically bound electron hole pair) with a typical binding energy of $0.3 - 1$ eV, is generated within the donor [15], see Figure 2.4 panel b. This exciton is free to propagate in the material until it reaches a donor|acceptor interface, barring that it is first scattered in the photoabsorbing material and relaxes. Unfortunately, in planar devices, this is often the case as the exciton diffusion length within an organic semiconductor is in the order of $1 - 10$ nm [16]. To address the issue, organic solar cells are fabricated employing a mixture of donor and acceptor materials. This is referred to as a bulk heterojunction (BHJ) architecture, and allows for a large donor|acceptor interface, while maintaining sufficient active material. Due to the potential difference at this interface, the exciton dissociates via a charge transfer state and the electron is injected into the acceptor. The lowest unoccupied molecular orbital (LUMO) of both donor and acceptor materials is selected and chemically tuned to ensure an energetically favourable electron transfer. Traditionally, the hole will diffuse within the photoabsorber to be extracted at an electrode, however an additional hole transport material can also be contacted to the donor. The maximum voltage which is extracted from fully organic solar cells, is determined by the potential energy separation between the LUMO of the electron accepting material and the HOMO (highest occupied molecular orbital) of the electron donor material or hole conductor [12, 13]. Currently, it is 0.78 V for the best performing organic research solar cells [9].

The benefits of fully organic solar cells include their very simple and energy efficient manufacturing techniques which have low production costs, such as roll-to-roll

printing. The materials employed for their fabrication are abundant and environmentally friendly and result in lightweight flexible devices [12, 17]. However, the current drawback of mainstreaming these photovoltaic devices for commercial use lies with the low power conversion efficiencies obtained, caused by the high quantum defect and losses during exciton propagation and charge separation.

2.4 Dye sensitised solar cells

In addition to organic solar cells, the category of emerging photovoltaic devices includes dye sensitised solar cells (DSSCs). The working principle of these devices is similar to that of the fully organic solar cells introduced above, however the organic electron acceptor is replaced by an inorganic semiconductor. They were developed as low cost alternatives to inorganic solar cells, and boast advantages over silicon solar cells in their many design opportunities brought upon by their transparency and colour variations, mechanical flexibility and light weight. Their enhanced performance in diffuse light and at elevated temperatures results in their excellent suitability in realistic outdoor conditions and indoor applications [2]. Inorganic metal oxide semiconductors such as TiO_2, ZnO, SnO_2 and Nb_2O_5 are commonly employed in DSSCs, however TiO_2 and ZnO are most popular as they are widely available, cheap and easy to deposit [18, 19]. Their use as photoabsorbers is however limited by their large bandgaps corresponding to absorptions in the ultraviolet spectral region. Therefore through the inclusion of a coupled light harvesting material, a dye characterised by an absorption maximum in the visible spectral region, the absorption of these semiconductors is sensitised towards longer wavelengths [20, 21].

Charge extraction

The DSSC device architecture comprises of a photoanode consisting of a highly porous semiconductor nanostructure which is sensitised with a monolayer of dye to avoid losses in exciton propagation before charge separation, see Figure 2.4 panel c. Upon illumination, the dye molecules are photoexcited thus generating electron hole pairs. Charge separation occurs at the dye|semiconductor interface where electrons are injected, on an ultrafast timescale, into the conduction band of the neighbouring semiconductor thus resulting in oxidised dye molecules. From within the semiconductor, the injected electrons can then be extracted to the external circuit and towards the cathode. The circuit of the cell is traditionally closed with a liquid electrolyte solution utilising iodide/triiodide as the redox couple, however many variations including solid hole conductors have since been employed [22]. In the event that the former is used, the oxidised dye is reduced through electron transfer from the redox couple, itself reduced at the cathode. Conversely, in the event that the latter is employed, the reduction of the oxidised dye occurs via hole transfer to the solid hole conductor, and hole diffusion to the cathode [21]. The maximum voltage which can be extracted from these devices is typically 0.75 V [9]. It is determined by the potential difference between the quasi-Fermi level of the semiconductor under illumination and the redox potential, and is therefore independent of the dye used.

Pioneering devices

Employing a bulk dye layer in a DSSC is beneficial in increasing the absolute amount of absorbed light. However, the charge diffusion length within a compact dye layer is not sufficiently long, and recombination is likely to take place before the electron can be transported out of a dye aggregate. A solution to this problem was first presented in 1991 by Grätzel and O'Regan through the introduction of a highly porous semiconductor nanostructure sensitised with a monolayer of dye. Their solar cells were fabricated by sensitising TiO_2 nanoparticles with an organometallic ruthenium complex. By making this change to the device architecture, they increased the efficiency of the DSSC devices at the time from 1% to above 7% [23]. To date, the highest efficiency dye sensitised solar cells were fabricated by sensitising nanoporous TiO_2 with a porphyrin dye and closing the circuit with a cobalt electrolyte [24]. Even though efficiencies of up to 13% were reported for these devices, they were not officially recognised in the record research-cell efficiency tables.

Photoelectrode

Although the TiO_2 – ruthenium dye combination is the most common DSSC photoanode, the deposition of a highly porous TiO_2 nanostructure requires high temperature annealing (450°C) and therefore a rigid glass substrate. In contrast, ZnO can be electrodeposited at low temperatures (70°C). The low energy deposition of ZnO thus allows for the usage of flexible substrates resulting in a lower cost of fabrication and increased device versatility. Moreover, both semiconductors are stable in contact with other chemical compounds, more so TiO_2 than ZnO [25], and have comparable bandgaps (approximately 3.2 eV) as well as very similar conduction and valence band energies. The electron mobility of ZnO is superior to that of TiO_2 approximately $200 - 300\ cm^2V^{-1}s^{-1}$ versus $0.1 - 4\ cm^2V^{-1}s^{-1}$ [18]. Additionally, more cost effective and easily available organic dyes, such as the indoline dye D149, are used together with ZnO resulting in reasonable power conversion efficiencies [26]. The introduction of organic dyes as a replacement for the expensive organometallic metal complex dyes (due to their rare earth metal centres), further decreased the cost of DSSCs in comparison to their silicon counterparts. Over the last 26 years, a multitude of variations of semiconductors and dyes have been developed for implementation in DSSCs and have been studied in great detail [19].

Charge dynamics

The injection of photoexcited electrons from the organic dye into the ZnO conduction band is an important process with respect to cell optimisation and has been well studied [27–37], including by us [38–42]. It has been found that this electron transfer occurs on a femtosecond to picosecond timescale, slower than measured for TiO_2. Furthermore the role of ZnO surface states in the electron injection process has been determined to be non-negligible, however the exact mechanism has, prior to this work, not yet been observed.

Our approach

Throughout this work, novel indoline dye sensitised electrodeposited ZnO solar cells were investigated with the use of transient absorption spectroscopy (TAS). The devices were either closed with the traditional iodide/triiodide liquid electrolyte solution or with a solid hole conductor. TAS enables us to follow the charge transfer mechanisms occurring within the fully operational devices in real time. By extending our measurement window from the visible spectral region further into the infrared (IR), we were able to probe the population dynamics of the ZnO conduction band (CB) and determine the exact electron injection pathway from the photoexcited dye into ZnO. Furthermore this gave us access to observe new spectral features in the near IR spectral region with 200 fs temporal resolution.

As will be explained in more detail in the chapters to follow, the injection of electrons from the photoexcited indoline dye into the ZnO CB can take place directly on an ultrafast timescale. With our measurements, we discovered that electron injection can also occur in a slower stepwise manner via intermediate charge transfer states. Moreover, this phenomenon is a direct result of the surface electronic structure of electrodeposited ZnO and chemistry which occurs at the dye|ZnO interface. It is thus not observed in cells prepared with TiO_2, but similar charge transfer via surface trap states has also been suggested for hole injection into NiO [43].

By developing our TAS setup to probe further into the near IR spectral region, we directly observed the broad absorption of these intermediate charge transfer states and determined their lifetimes. Prior to this study the stepwise injection of electrons into the ZnO CB was not directly observed. By systematically comparing the temporal evolution of a multitude of temporal traces throughout our entire probed spectral region, we could assign time constants to the charge transfer processes directly and not just infer the processes from the population dynamics of the ZnO CB. Please refer to Chapters 4 and 5 for further details regarding the DSSC solar cell devices as well as our spectroscopic measurements.

By learning the charge transfer dynamics which occur in these novel indoline dye sensitised electrodeposited ZnO solar cells, we hope to provide valuable fundamental physics and chemistry reasons pertaining to the stability and efficiency of indoline DSSCs. Based on our results, new better materials can be synthesised by chemists and material scientists for use in dye sensitised solar cell devices. As this technique is time consuming, it is not possible to apply it to all new materials as a characterisation method, but we rather strive to complement and explain the macroscopic properties of photovoltaic devices, and try to draw general conclusions valid beyond the specific material combination.

2.5 Perovskite solar cells

As a natural progression in the development of DSSCs and organic solar cells, we investigated perovskite solar cells. Perovskite materials were first introduced as sensitisers for traditional DSSCs by Kojima *et al.* in 2009, however only resulting in an efficiency of 3.8% [44]. Through the improvement of device architectures and fine-tuning of the material chemical composition, there has been a meteoric rise in perovskite solar cell efficiencies over the last 8 years, thus sparking much interest in the scientific community, see Figure 2.3.

Perovskite materials

The class of perovskite materials obtained their name from sharing a crystal structure with the chemical compound calcium titanate ($CaTiO_3$) named after Lev Perovski, a Russian mineralogist [45]. In the context of photoabsorbers, perovskites are hybrid organic-inorganic materials with the cubic crystal structure ABX_3 where A is most commonly a large organic cation such as methylammonium (MA^+) or formamidinium (FA^+) or a monovalent metal such as caesium (Cs^+) and is surrounded by BX_6 octahedra. To date, only these three cations have been found to stabilise the 3D perovskite crystal structure. B is a divalent metal cation such as lead (Pb^{2+}), tin (Sn^{2+}) or germanium (Ge^{2+}), and X is a halide anion (I^-, Cl^-, Br^-), refer to Figure 2.5 [46]. The variation in sizes of ions leads to a distortion of the ideal cubic crystal structure of their namesake calcium titanate, thus resulting in the more stable orthorhombic or tetragonal crystal structures as the common perovskite crystal structures at room temperature [13, 45].

The electronic nature of halide perovskites in general, is qualitatively very similar, barring a few minor differences which arise from crystal symmetry. The electronic structure of the highest valence and lowest conduction bands is determined by the divalent metal cation and halide anion. The valence band maximum is generated through the hybridisation of the metal ion s and halogen ion p orbitals, while the conduction band minimum is mostly generated from the empty metal ion p orbital. The electronic states of the cation are not close to the highest valence and lowest conduction bands of the perovskite, therefore they do not contribute to the bandgap, however the permutation of divalent metal and halogen ions do contribute [46, 47].

The traditionally used perovskite photoabsorber is $MAPbI_3$ with an associated optical bandgap of 1.55 eV. Substituting the iodide ion by lighter halides increases the optical bandgap to 2.24 eV for Br^- and 2.97 for Cl^- [48–51]. The presence of chlorine was additionally found to increase the photovoltaic performance of the solar cells [52], however a large increase in device stability was rather achieved by mixing iodine and bromine ions into the perovskite structure [51]. The increased stability occurs due to the smaller size of Br^- with respect to I^-, therefore favouring the more stable cubic crystal structure as opposed to the tetragonal $MAPbI_3$ room temperature structure [13]. By mixing the organic cations, the perovskite absorption is broadened spectrally and it's chemical stability is improved leading to larger photocurrents and therefore higher device efficiencies [53–58]. The currently best performing solar cells employ a lead iodide based perovskite fabricated with a mixture of MA^+, FA^+, Cs^+ and Rb^+ cations, and I^-; or a mixture of MA^+, FA^+ and Cs^+ cations, and a mixture of I^- and Br^- anions [59, 60].

Preceding and in parallel to their use as photoabsorbers, perovskites materials were studied in the context of light emitting diodes [61–63], within devices for stimulated emission [64], as well as in the field of transistor technology as field-effect transistors [65–67]. Reports have also been published of their use as hard radiation detectors as well as in photocatalytic water splitting cells [68, 69].

The versatility of these materials lies within their optical and electronic properties. High absorbance coefficients (in the order of 10^5 cm^{-1} [48]) are complimented with broad absorption spectra thus resulting in efficient harvesting of solar electromagnetic radiation. Low exciton binding energies (< 0.05 eV [70]) eliminate the need for an interface to mediate charge separation, while high electron and hole mobilities ($2 - 10$ $cm^2V^{-1}s^{-1}$ and $5 - 12$ $cm^2V^{-1}s^{-1}$ respectively [71]) and long charge carrier

diffusion lengths (> 1 μm [68, 72]) ensure that charges can be harvested efficiently [13, 45].

Moreover, perovskites exhibit multiple phase transitions at various temperatures. For example, the well studied, $MAPbI_3$ crystal is orthorhombic below 160 K (low temperature phase), tetragonal in the range between 160 K – 330 K (room temperature phase), and cubic above 330 K (high temperature phase) [47]. As these phase transitions alter the electronic band structure of the perovskite, they in turn affect the associated optoelectronic properties of the perovskite materials, and must therefore be taken into account when investigating the photoinduced charge dynamics processes [73].

What makes perovskite solar cells so groundbreaking is the combination of the aforementioned optical and electronic properties of the photoabsorber together with the simplicity of device preparation, as well as the low cost and wide availability of the materials required.

Pioneering devices

The device architecture of perovskite solar cells has evolved over the years mirroring the rise in efficiencies. As mentioned above, perovskites were first introduced into the mesoscopic DSSC structure to replace the photoabsorbing dye [44]. However, a direct contact to the liquid electrolyte solution lead to degradation of the perovskite material ($MaPbI_3$) to produce the PbI_2 precursor, resulting in poor device stabilities. It was therefore replaced with the solid hole transport material Spiro-OMeTAD, leading to a sandwich planar cell architecture. This is referred to as the normal device structure in the perovskite community and inverted device structure in the organic solar cell community [13, 45]. This, although simple change, resulted in the first notable increase in the efficiency of perovskite solar cells toward 10% [74, 75].

Charge transport materials

The function of electron and hole transport materials in the context of perovskite photovoltaic devices, is to facilitate single directional charge transport towards the electrodes, whereby it can be extracted into the external circuit. Common electron transport materials include TiO_2, ZnO and PCBM, while frequently used hole transport materials may be organic (Spiro-OMeTAD), polymers (P3HT, PEDOT:PSS) and even inorganic materials (NiO, CuI). Currently, the highest efficiency perovskite solar cell device is contacted to Li-doped mesoporous TiO_2 and Spiro-OMeTAD electron and hole transport materials respectively [60]. The perovskite and charge transport materials have been well studied and carefully selected resulting in state of the art photovoltaic devices. However, in reality, the journey toward higher efficiencies is rather characterised by a multitude of permutations [45, 76–78]. For a summary of additional charge transport materials, refer to the work of Chueh *et al.* [79].

Charge extraction

The charge generation and extraction processes which occur in perovskite solar cells are somewhat a mixture of those introduced for DSSCs and organic solar cells above and are outlined in Figure 2.4 panel d. Excitons are generated in the perovskite photoabsorber upon illumination, whereby they dissociate into free charge carriers due

to the low exciton binding energies and high mobilities [70, 80–82]. Although the low binding energies suggest the generation of free charge carriers in these materials immediately following photoexcitation, these photogenerated excitons have been found to be stable in perovskites at room temperature and above [46]. This is especially true for perovskites with a large concentration of bromine ions as the substitution of iodide by lighter halides was found to increase the excitonic nature of the perovskite materials [49]. Following the dissociation of excitons, the charges are extracted into the external circuit by means of the aforementioned contacted electron and transport materials. The maximum voltage which can be extracted from these photovoltaic devices is given by the potential difference between the conduction band of the electron transport material and the valence band of the hole transport material and is approximately 1.3 V if just radiative recombination processes are taken into account [13, 83]. However, as will become more evident in the chapters to follow, the recombination mechanisms dominant in perovskites are also non-radiative and can depend nonlinearly on charge carrier density, therefore decreasing the maximum extractable voltage to roughly 1.1 V [57, 84, 85].

Device fabrication

The fabrication of perovskite thin films is carried out predominately with the use of two methods: spin coating and vapour deposition. The spin coating method can either be followed in one or two steps. It is advantageous in its simplicity and low cost. It entails the preparation of a stoichiometrically predetermined precursor solution which is spin coated onto a substrate, and subsequently heated to remove excess solvent. For better control of the film morphology, the vapour deposition method produces more uniform and reproducible results. Its shortfall however, appears in terms of monetary and energy cost of perovskite fabrication, therefore reducing its commercial scalability. The most common deposition method for highly efficient perovskite solar cells is the anti-solvent assisted crystallisation spin coating approach (ASAC). This method entails the addition of a second solvent, the so called anti-solvent, in which the perovskite is insoluble. The presence of this non-dissolving solvent is believed to cause supersaturation and aid in the formation of a highly uniform, densely packed perovskite layer free of pinholes [13, 45, 73, 86, 87].

The photovoltaic device performance is highly reliant on the crystallisation of the perovskite layer in terms of both grain size and morphology. Even though large grain domains are favourable in terms of improving cell efficiencies due to increased light scattering, the grain boundaries present in perovskite materials are electrically indistinguishable from the bulk, in contrast to Si and GaAs photovoltaic devices. In the deposition of perovskite layers, pinholes must be reduced to avoid the device short circuiting. Although not necessary due to its high absorption coefficient, the active layer thickness can be increased in perovskite solar cells, without a tradeoff in the extracted photocurrent density [13, 45]. In addition, it has been found that the charge carrier mobilities are dependent on the perovskite fabrication procedure [46]. Preparation details of the perovskite thin films which were investigated in this work are available in Chapter 6.

Shortfalls of perovskite solar cells

As mentioned above, the immense interest in perovskite solar cells over the last 8 years arose from their unmatched rise in power conversion efficiencies. However as they remain an emerging photovoltaic technology, and since the focus of the scientific community has mostly been on improving their efficiencies, there continue to be a number of drawbacks which must be addressed before these devices can compete with state of the art silicon solar cells and are ready for mainstream commercial production.

The first and most pressing issue is that of their low long term stabilities in ambient conditions. It has been reported that in the presence of water, even in small quantities, the perovskite structure degrades, somewhat reversibly, back into its precursors. In the case of $MAPbI_3$, the crystal breaks down into PBI_2 and the volatile MAI compound [49, 88–90]. Furthermore, it has also been reported that the aforementioned degradation process is accelerated in the presence of heat (above 100°C) [45]. Towards a possible solution, a phosphonic acid ammonium compound was added during the deposition of a $MAPbI_3$ thin film, resulting in a considerable increased stability of the perovskite in the presence of moisture [91]. Furthermore, perovskite layers which contain a mixture of MA^+, FA^+ and Cs^+ cations have been reported to be most resilient to degradation. This is due to the increased stability of the actual crystal structure, and even resulted in improved device efficiencies [60]. Alternatively, the low stability of the perovskite crystals has most commonly been addressed through the complete encapsulation of the device with glass or a polymer sealant such as PMMA. The instability of perovskite solar cells under UV illumination has also been reported and assigned to TiO_2 trap states rather than the perovskite material itself [13].

Moreover, the commercial scalability of perovskite solar cells proves to be a challenge. While state of the art research-cells with high efficiencies have been prepared, the surface area of these devices is often less than 1 cm^2. A high efficiency, stable perovskite photovoltaic module with surface area of a commercially acceptable size has yet to be developed [45].

Another notable drawback of perovskite solar cells lies with the toxicity of lead, the most common divalent metal cation employed in the best efficiency generating perovskite solar cells. Many studies have focussed on replacing the lead ion with a non-toxic alternative such as tin or germanium, however these perovskite analogues are not stable in ambient air due to the oxidation of the metal ions [46]. Lee *et al.* succeeded in developing a Sn^{4+} metal salt (Cs_2SnI_6) which is stable in ambient conditions, and employed it as a hole conductor in porphyrin dye sensitised TiO_2 solar cells. Even though the fabricated solar cells were stable in the presence of moisture, they did not match the efficiencies obtained from their lead based perovskite counterparts [92]. Studies have thus instead focused their attention on quantifying the environmental impact of the lead, should it be used in large scale solar farms. The possible lead pollution was found to be vastly less significant in comparison to that caused by the fossil fuel and mining industries, as well as through the manufacturing and incorrect disposal of batteries [45, 93–98].

Spectroscopic measurements

Even though these aforementioned macroscopic alterations have proved to aid with increasing the stability and efficiency of perovskite solar cells considerably, and address the issue of the toxicity of lead, the changes have most often not been as a result

of detailed spectroscopic studies, but rather as hands-on solutions. Therefore, to better understand the material as well as its optoelectronic characteristics, one must study the electronic nature of the perovskite itself, together with the fundamental physics and chemistry processes responsible for the generation and extraction of free charges.

Due to the multi-band electronic nature of perovskites, the exact conduction and valence bands contributing to the initial photophysics processes, have yet to be agreed upon within the scientific community. Furthermore as a result of the many degrees of freedom, especially in perovskites containing a mixture of organic cations and halide atoms, the computation of the exact energies and momentum distributions of the many valence and conduction bands becomes progressively difficult and thus increases the charge dynamics channels available within the material.

Figure 2.6 consists of a simplified sketch of the band structure (panel a) alongside the steady state absorption spectrum of $MAPbI_3$ (panel b), as shown in the review paper of L. M. Herz [47]. The band structure diagram of $MAPbI_3$ was drawn as a summary of the calculated band structures of Even *et al.* [99, 100] and serves as a general sketch of the lowest energy conduction and highest energy valence bands present in lead based perovskite materials. As depicted in the sketch, the lowest energy conduction band (CB1) is a spin orbit split-off band (marked as SO in the figure), while CB2 comprises of heavy and light electron states (depicted as HE and LE). Furthermore, the inclusion of spin orbit coupling in the calculations for the electronic band structure of perovskite materials, has shown to lift band degeneracy, therefore the mixed cation lead halide perovskites are known to have fewer degenerate conduction and valence bands [101–103]. As mentioned above, the electronic character of the conduction and valence bands, is determined mostly by the metal cation and somewhat by the halogen anion orbitals, and is thus very similar for all lead based perovskite materials. The strong connection between the M- and R- points in reciprocal space allows for the generation of electron hole pairs in the entire spectral region between these two points, upon photoexcitation [104–106]. This feature can be directly observed in the very broad absorption spectra of perovskite materials, and is depicted with the various colour arrows in Figure 2.6 panels a and b.

In general, the ultrafast transient spectroscopic data of perovskite materials is characterised by two ground state bleaching signals corresponding to electronic transitions in the visible spectroscopic region: corresponding to the optical bandgap at the R-point (1.6 eV, $\lambda = 775$ nm) as well as at the higher resonant energy of approximately 2.6 eV ($\lambda = 480$ nm), the origin of which is not yet well understood and agreed upon. Some studies suggest the higher energy bleaching signal arises from the depopulation of a lower energy valence band (VB2) and assign it to the VB2 – CB1 transition [107]. Alternatively it is thought to correspond to the depopulation of the highest energy valence band at the R-point, and therefore assign it to the VB1 – CB2 transition. While both these R-point transitions (shown as dashed arrows in Figure 2.6 panel a) are dipole-allowed, their associated oscillator strengths were determined to be much weaker than the VB1 – CB1 transition away from the optical bandgap[108]. Therefore the higher energy bleaching signal is most often assigned to the VB1 – CB1 electronic transition away from the R-point [99]. Moreover, suggestions for the origin of this signal centred about 2.6 eV ($\lambda = 480$ nm) have also included the presence of a charge transfer state inferring the possible spectroscopic contribution from electronic states of ionic lead halide complexes, also known to be present in perovskite thin films [109–111]. It is possible to interpret the latter of the two as equivalent to the contribution assigned to

the electronic band structure of the perovskite material as the conduction and valence bands are created from the lead halide orbital hybridisation [47, 107, 108, 112–114].

As an additional note, upon photoexcitation of the ionic compound, PbI_2, a broad associated ground state bleaching signal centred around 510 nm is evident in spectroscopic measurements. The presence of this signal is employed as an indication that the perovskite thin film has partially degraded back into its precursor solutions [115].

A further discussion point within the field of spectroscopy applied to perovskite materials, is that of the spectral wing of the optical bandgap bleaching signal (1.6 eV, $\lambda = 775$ nm) [107, 109, 116–118]. The photoinduced features which occur slightly above the bandgap (as observed at approximately 760 nm) are believed to be a mixture of excitonic and free charge carrier effects and the associated dynamics at the band edge are assigned to the hot charge carriers in the conduction band [116, 118]. Furthermore at high charge carrier densities, these excitonic features are broadened through scattering [47].

In order to better our knowledge of the physics and chemistry occurring in perovskites immediately following photoexcitation, we must learn how charges are generated and the processes through which they can be extracted, or recombine, and the reasons underlying their dynamics. While this is not the complete picture behind the high efficiencies achieved with perovskites as photoabsorbers in photovoltaic devices, it does give us insight into the internal mechanism responsible for their versatility and determines the ultimate limits of efficiency.

Femtosecond transient absorption spectroscopy (TAS) follows the change in absorption of a sample upon photoexcitation on an ultrafast timescale. It provides a direct measure of the population and depopulation dynamics of various electronic states, in real time. This method has been employed together with similar spectroscopic techniques such as photoluminescence, optical pump terahertz probe, time delayed collection field and microwave photoconductivity spectroscopy, in numerous investigations, to study the charge dynamics and transfer processes within perovskite materials upon optical excitation [47, 107, 109, 116–118].

Charge dynamics

Charge generation, ultrafast cooling upon high energy non-resonant excitation and nonlinear recombination processes have been observed for perovskites and modelled similar to other inorganic semiconductors.

Initial charge carrier relaxation

The initial charge carrier relaxation processes which occur in perovskites upon high energy photoexcitation, have been studied extensively, especially within the $MAPbI_3$ system, and are shown using dashed arrows in Figure 2.6 panel a [107–110, 112–118]. A hot charge carrier distribution is generated upon non-resonant photoexcitation, which thermalises on an ultrafast timescale to the band edges, via carrier-carrier scattering. Subsequently, charge carrier cooling takes place via charge carrier interactions with the crystal lattice [47]. Experimentally, an associated time constant of approximately 500 fs was determined, and is generally agreed upon for the charge carrier cooling process, and is supported by density functional theory (DFT) calculations [108].

High charge carrier densities

Furthermore, the cooling of hot charge carriers has been found to slow down upon high intensity photoexcitation due to a hot phonon bottleneck occurring at the conduction band edge. In this case, phonon reabsorption results in a high phonon occupancy thus extending the time for which the charge carriers remain hot [119, 120]. In addition to the aforementioned bottleneck, other many-body effects have also been reported for the behaviour of perovskites considering a large charge carrier density, including state filling effects as well as bandgap renormalisation. In the case of bandgap renormalisation, the band edge corresponding to the optical bandgap bleaching signal, shifts towards lower energies. This is caused by the fact that no two electrons with the same spin may fill the same unit cells (Pauli principle). Conversely, state filling effects refer to a higher energy shift of the optical bandgap bleaching signal band edge. This shift, also referred to as the Burstein-Moss effect, is caused by the fact that there are a finite number of states available near the bandgap, which can be occupied by electrons (Fermi particles) [47, 109].

Charge recombination processes

From reported time resolved terahertz photoconductivity combined with photoluminescence measurements, it has been shown that in the event that the perovskite material is optically excited with a varied photon flux, the electron hole recombination dynamics depend on the generated charge carrier densities (n) in the conduction and valence bands [70]. This dependence on excitation photon fluence was found to be non-linear and described mathematically as per $\frac{\mathrm{d}n(t)}{\mathrm{d}t} = -\mathrm{A}n(t) - \mathrm{B}n(t)^2 - \mathrm{C}n(t)^3$. The rate constants A and B correspond to the monomolecular and bimolecular recombination processes respectively due to the number of charged species required, while C corresponds to the trimolecular or many-body recombination. A more detailed explanation of the rate constants and their characteristics is given in Chapter 7.

Our approach

Our goal in this study was to observe the processes through which charge carriers are generated and extracted in methylammonium formamidinium mixed halide perovskite materials, specifically $FA_{0.85}MA_{0.15}PbI_{2.55}Br_{0.45}$. We were interested in distinguishing the possible recombination channels and assigning rates to them respectively and therefore learning about their associated probabilities, especially under the influence of varying pump pulse fluence. With the use of this knowledge we aimed at building the simplest consistent model describing the photoinduced charge carrier dynamics in $FA_{0.85}MA_{0.15}PbI_{2.55}Br_{0.45}$. This was done in order to learn why charge transport is so good within mixed perovskite materials in general, while more specifically the potential reasons behind the high efficiencies achieved when these materials are employed as photoabsorbers in photovoltaic devices. Based on our findings, mixed perovskites can be chemically tuned to further improve device stabilities and efficiencies.

In order to achieve the aforementioned goals, we employed femtosecond transient absorption spectroscopy in the visible and near infrared spectral regimes, the details of which are outlined in Chapter 3. By linking the spectral signatures of the $FA_{0.85}MA_{0.15}PbI_{2.55}Br_{0.45}$ thin films to their approximate electronic band structure, and thus connecting the temporal evolutions of the many spectroscopic signatures, we were able to

model the photoinduced charge dynamics which occur together with the lifetimes of the associated states.

As will be discussed in great detail in Chapter 7, we selected a perovskite material which yields high power conversion efficiencies when employed in solar cell devices and observed how it behaves microscopically upon illumination. This was done by photoexciting the thin film with different photon energies and comparing the temporal evolution of its associated transient absorption signals. A multitude of temporal traces spanning the entire probed spectral region were mathematically fitted with the analytic solution of the the recombination rate equation presented above and linked to obtain the simplest consistent charge dynamics model possible. Additionally, by varying the pump pulse fluence, we were able to directly obtain values for the rate constants A, B and C corresponding to the monomolecular, bimolecular and trimolecular recombination mechanisms in perovskites, for a given crystal domain of the $FA_{0.85}MA_{0.15}PbI_{2.55}Br_{0.45}$ thin film. Furthermore, the spectral features observed in the transient absorption spectra of $FA_{0.85}MA_{0.15}PbI_{2.55}Br_{0.45}$ thin films, are unique to this particular chemical stoichiometry.

Finally, as will be evident in the chapters to follow, the use of a spectroscopic technique such as femtosecond transient absorption spectroscopy in the visible and near infrared spectral regions, enables us to follow the microscopic charge dynamics and transfer process which occur in photoabsorbing materials. From the results, we are able to learn the fundamental physics and chemistry reasons pertaining to the macroscopic spectroelectrochemical characteristics of fully operational solar cells and photoabsorbing materials to be used in photovoltaic devices. While device engineering is an important tool into bettering the solar cells used to harvest solar energy and convert it to electrical energy, the results obtained using TAS serve to aid, in parallel, with the development of new better photovoltaic materials for green energy.

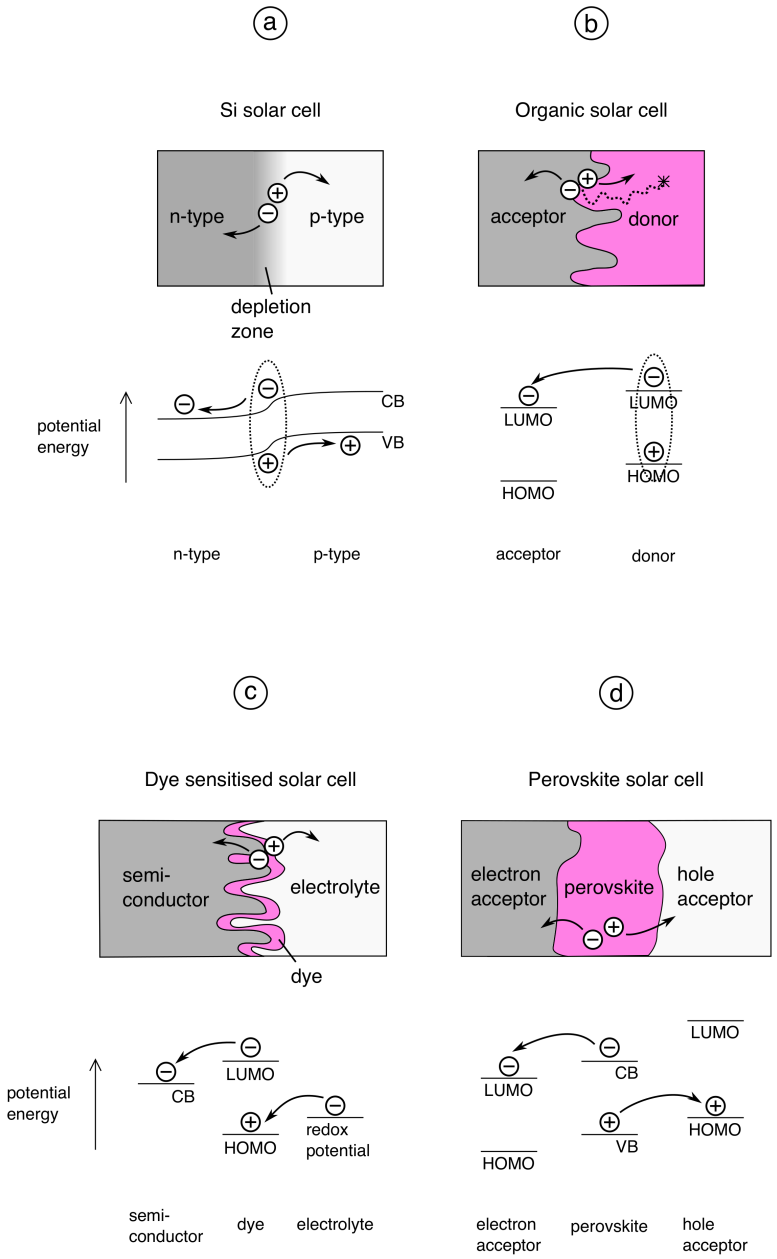

Figure 2.4: Diagrams of the processes which are responsible for the conversion of solar energy into electrical energy in typical solar cell devices, are shown together with a schematic of the associated energy levels of the various materials employed. **Si solar cells (panel a):** an electron hole pair is generated in the depletion zone upon photoexcitation, the electron is extracted to the n-type material and the hole to the p-type material due to the favourable potential energy minimisation. **Organic solar cells (panel b):** an exciton is generated in the donor material upon photoexcitation, barring recombination it diffuses to the material interface with the acceptor material where it dissociates into free charge carriers. The electron is extracted into the acceptor material and the hole remains in the donor material due to the energetic separation between the respective highest occupied molecular orbitals (HOMOs) and lowest unoccupied molecular orbitals (LUMOs). **Dye sensitised solar cells (panel c):** photoexcitation of the dye monolayer results in the generation of electron hole pairs on the surface of the highly porous semiconductor material, the electrons are injected into the conduction band (CB) of the semiconductor leaving behind oxidised dye molecules which are reduced with the use of the redox couple present in the electrolyte solution. **Perovskite solar cells (panel d)**: excitons are generated in the perovskite photoabsorber upon illumination which mostly dissociate into free charge carriers immediately. The electrons are injected into an electron transport material, while the holes are harvested with the use of a hole transport material.

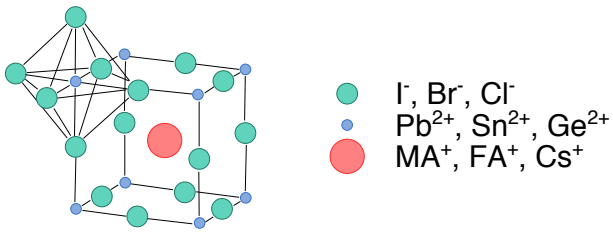

Figure 2.5: A diagram of the cubic crystal structure of hybrid organic-inorganic perovskite photoabsorbing materials. The central ion (shown in red) is most commonly a large organic cation such as methylammonium (MA^+) or formamidinium (FA^+) or a monovalent metal such as caesium (Cs^+). It is surrounded by eight divalent metal cations (shown in blue) such as lead (Pb^{2+}), tin (Sn^{2+}) or germanium (Ge^{2+}) which sit at the centre of octahedra, coordinated to halide anions (shown in green) such as I^-, Cl^-, Br^-. While perovskite materials can be fabricated with one ion from each of the three categories, they can also be prepared with most mixtures and combinations thereof.

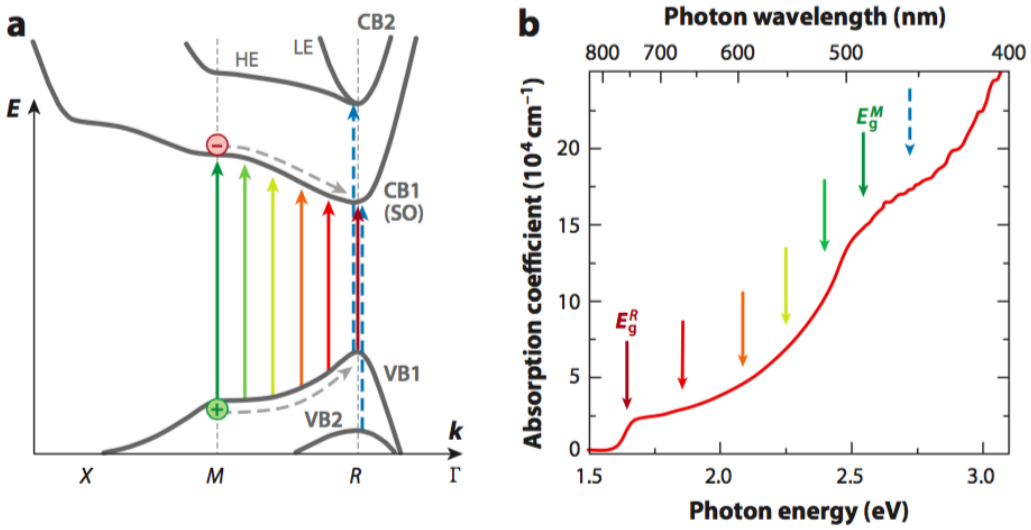

Figure 2.6: **Panel a:** A diagram depicting a summary sketch of the electronic band structure of $MAPbI_3$ which was drawn with the help of density functional theory calculations. The lowest energy conduction bands, CB1 (spin-orbit split off band, SO) and CB2 (showing both heavy electron and light electron states, HE and LE), and highest energy valence bands, VB1 and VB2, are marked in the sketch together with the allowed electronic transitions which are depicted with the use of the vertical colourful arrows. The dashed horizontal arrows depict the hot charge carrier cooling to the band edges. **Panel b:** The steady state absorption spectrum of $MAPbI_3$ depicting the absorption coefficient as a function of both photon energy (bottom axis) and photon wavelength (top axis). The colour arrows correspond to the allowed electronic transitions depicted in panel a, and serve as indication that the continuum of allowed transitions between the M- and R-points result in the very broadband absorption of perovskites. Furthermore the bandgap energies corresponding to the M- and R-points are shown on the graph as E_g^M and E_g^R respectively. The figure presented above was obtained from the review article of L. Herz [47].

3. Femtosecond Transient Absorption Spectroscopy

In order to observe the charge dynamics which occur in photoabsorbing materials as well as fully operational solar cells, we utilise femtosecond transient absorption spectroscopy (TAS). With the use of this measurement technique in a pump-probe architecture we are able to follow, in real time, the population and depopulation dynamics of electronic states from their spectroscopic signatures in the visible and infrared spectral regimes. By linking the absorption signals of the material to its electronic band structure we can follow electronic excitations in time. This in turn enables us to link the electronic structure of the material to possible photoinduced charge dynamics processes which occur. Of course, to be able to do this effectively, we must be looking on the correct timescale, therefore we employ TAS in the femtosecond regime.

This chapter will serve as an introduction to the pump-probe measurement technique, as well as give a detailed explanation of our experimental setup together with a description of how we acquire our data. Finally, an example transient absorption spectrum is presented below with an introduction into our analysis approach, to aid with the interpretation of the experimental results in the chapters to follow. For further physics and mathematical details which underpin the processes described in this chapter as part of our experimental setup, a detailed description is presented as a part of my MSc work [39].

3.1 Pump-probe measurement technique

The population and depopulation dynamics of electronic states in photoabsorbing materials often occur on femtosecond and picosecond timescales. In order to observe these processes in real time, an appropriate measurement technique of comparable magnitude and dimension must be employed. However, these charge dynamics are too fast to be measured using an electronic detector as 1 fs is equivalent to 1 PHz repetition rate. Electronic circuits cannot be made small enough to provide these readout frequencies, therefore requiring an alternative approach for the use of conventional spectroscopic cameras. As a solution, we employ an optical pump – optical probe measurement technique.

Stroboscopic photography

Pump-probe spectroscopy can be likened to the stroboscopic photography of a particular dynamic which reveals information about its associated structure and velocity, refer to Figure 3.1. In the photograph, a gymnast is performing a Giant. The dynamic

is initiated by telling the gymnast to begin his acrobatic manoeuvre. This verbal command can be compared to the optical pump pulse of pump-probe transient absorption spectroscopy, and needs to be temporally shorter than the dynamic itself.

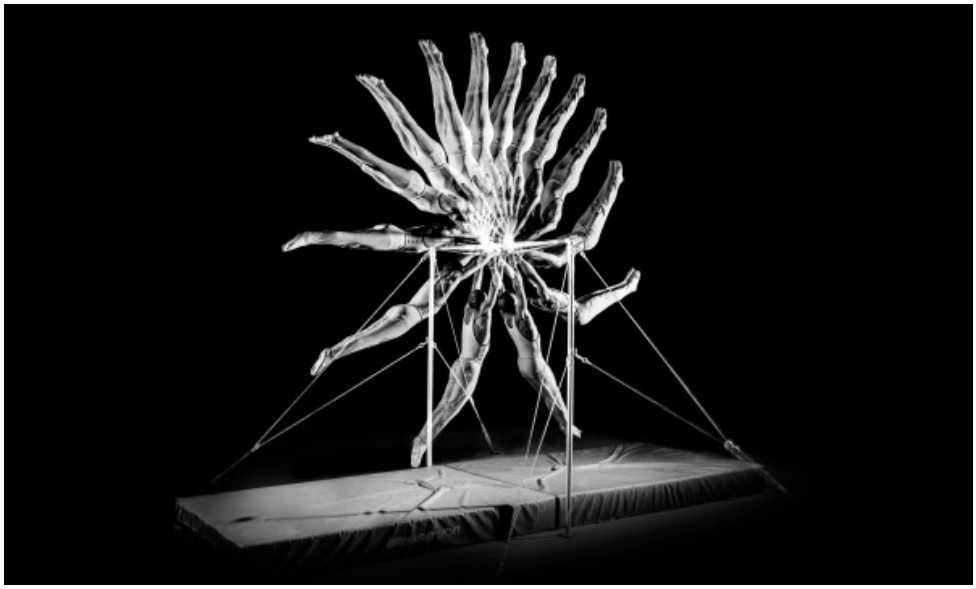

Figure 3.1: A stroboscopic photograph of a gymnast performing a giant. Used with permission from the photographer, Tom Hegen, please refer to reference [121] for copyright information.

The structure and dynamics of the gymnast performing a Giant, cannot be recorded with the use of a conventional photography camera in one go. Even though the camera's shutter speed is perhaps fast enough to capture a well resolved image of the gymnast at a given moment, the time the camera takes to reset itself in order to take a new photograph is too long to capture the dynamics. Therefore with the use of a conventional photography camera, both the structure and dynamics of the gymnast performing the Giant cannot be acquired in one measurement. What is done to address this issue, in the case of stroboscopic photography, is the following: the photograph is acquired in a dark room with a 'slow' photography camera and with the help of a stroboscope. The photographer sets the camera up with an open shutter and acquires an image every time the stroboscope flashes a light pulse.

Once the gymnast is told to begin the Giant, the dynamics are initiated and can be probed, through photography, at regular temporal intervals determined by the frequency at which the stroboscope operates. The resolution of each image is then given by the temporal duration of the light pulses of the stroboscope. As may seem obvious, the temporal duration of the acrobatic manoeuvre needs to be substantially longer than the duration of the probe pulses, and the frequency at which the stroboscope is run should be high enough that sufficient photos are acquired of the dynamic in order to determine the gymnast's change in velocity around the bar. This stroboscope probe can be likened to the optical probe pulse employed in pump-probe transient absorption spectroscopy, and the different signals can be separated by the slow detector, in this case spatially. Of course this is equivalent to employing many cameras to each take one photograph and delaying the time between when each photo is acquired. However this is not financially and experimentally feasible.

In the event that a stroboscope with a high enough frequency is not available, or in the case that the fast train of light flashes affects the ability of the gymnast to perform the Giant correctly, an alternative second solution is employed. The gymnast is asked to perform the Giant multiple times. Each time he performs the move he is photographed once, but at a different time during his acrobatic manoeuvre, following the verbal instruction to begin. The collection of photographs is then combined and one image is presented of the gymnast performing a Giant, providing us with information about both his orientation and velocity during his acrobatic manoeuvre. This method assumes that the gymnast can perform a Giant in an identical manner for each photo which is acquired, which of course is unrealistic.

The link to pump-probe TAS

In order to probe the sub picosecond dynamics which occur within photoabsorbing materials, we employ a pump-probe experimental technique which can be compared directly to the stroboscopic photography example introduced above. In order to access the ultrafast dynamics, we employ a commercially available femtosecond pulsed laser source.

As mentioned above, in an equivalent way to the verbal command, the photoinduced dynamics which occur within photoabsorbing materials are initiated with an optical pump pulse. This pulse is tuned to match electronic transitions of the material that are of interest to us. It is referred to as the 'pump' as it deposits energy into the sample, and it must be temporally much shorter than the dynamics which we would like to observe. The photoexcited material then decays via different mechanisms back to its ground state. This can be compared to the gymnast performing the Giant. At a given time following the excitation, the absorption of the photoexcited material is probed with the use of a second optical pulse – the 'probe', similar to the photograph which is acquired with the use of the stroboscope pulse. Once again, this laser pulse is required to be much shorter in duration than the kinetics which we would like to observe.

As we probe the absorption of the material with a second light pulse, we also deposit energy into the sample during the probing procedure. Therefore if we were to probe too many times during one relaxation cycle of the excited material, we would deposit too much energy into it and produce undesired nonlinear effects. For this reason, we rather employ a repetitive procedure similar to the second approach outlined in the explanation above: where we measure the absorption of the sample only once following its photoexcitation. After allowing enough time for the material to equilibrate fully and relax back to its ground state, we photoexcite it once again, and probe its absorption after a different temporal delay. By combining the many acquired absorption spectra we can determine the structure of the sample's spectral features and temporal evolution of the dynamics which occur during its relaxation. This is similar to how the final photograph of the gymnast, gives us information of both his orientation and velocity. In the case of pump-probe TAS however, the assumption that the system behaves in an identical manner for each photoexcitation is more realistic, given that we probe a large ensemble of molecules. Furthermore to increase the sensitivity of the measurement technique, we average over 3000 absorption measurements for each time step.

The temporal resolution achieved by pump-probe transient absorption spectroscopy

is determined by the cross correlation of the pump and the probe laser pulses, and is therefore on the femtosecond timescale, sub 200 fs in our experimental setup. With the use of transient absorption spectroscopy in a pump-probe architecture we are able to follow, in real time, the population and depopulation dynamics of electronic states pertaining to a photoabsorbing material, as our measurement technique is of comparable magnitude and correct dimension.

3.2 Our experimental setup

Our experimental pump-probe transient absorption setup is depicted in Figure 3.2. As can be seen from the sketch the setup comprises of a femtosecond laser source which is used to generate both the pump and the probe pulses. The pump pulse generation is achieved with the use of a non-collinear parametric amplifier (NOPA) which allows us to tune the central wavelength of the pump pulse, and contains a pulse compression component as well as a mechanical delay stage which is used to adjust the absolute temporal delay between the pump and probe pulses. The probe pulse is obtained either through white light generation thus producing broadband white light continua (WLC) or through the use of a second NOPA system for the generation of near infrared probe pulses. The acquisition of absorption spectra is achieved with the use of either a visible or an infrared spectrometer with attached CCD (charge coupled device) linescan cameras [122, 123].

Our femtosecond source is a ClarkMXR CPA2101 amplified femtosecond Titanium:Sapphire laser system. This chirped pulse amplifier (CPA) generates polarised broadband pulses ($\Delta\lambda = 8$ nm) centred around $\lambda = 775$ nm with a temporal duration of 150 fs and pulse energy of approximately 0.8 mJ. The fundamental laser beam has a pulse train frequency of 1 kHz and is split into two portions by means of a beam splitter, which are employed in the generation of pump and probe laser pulses.

Pump pulses

Approximately 30% of the fundamental pulse energy is directed to be employed in the generation of pump pulses. As mentioned above, the central wavelength of the pump laser pulses is selected to correspond to interesting electronic transitions of the photoabsorbing materials, with the use of a NOPA.

The NOPA setup consists of a 2 mm thick β-barium borate (BBO) crystal cut at an angle with respect to the optical axis for maximum seed pulse amplification. A horizontally propagating pump pulse centred about 387.5 nm is seeded by a chirped WLC in the BBO crystal, which is aligned at a vertical angle to respect the phase matching conditions for optical parametric amplification. The 387.5 nm pump pulse is generated by frequency doubling 90% of the fundamental laser pulse energy which enters the NOPA with the use of an additional BBO crystal, while the WLC is produced by means of focusing the remaining 10% of the pulse energy in a sapphire crystal. By employing the aforementioned non-collinear geometry, we achieve efficient phase matching between the various spectral components of the WLC seed pulse and the 387.5 nm pump pulse for the entire length of the BBO crystal, thus producing an amplified signal in the visible spectral regime. To achieve maximum parametric amplification, the k vector component of the WLC seed pulse along the pump pulse axis must be equal to the

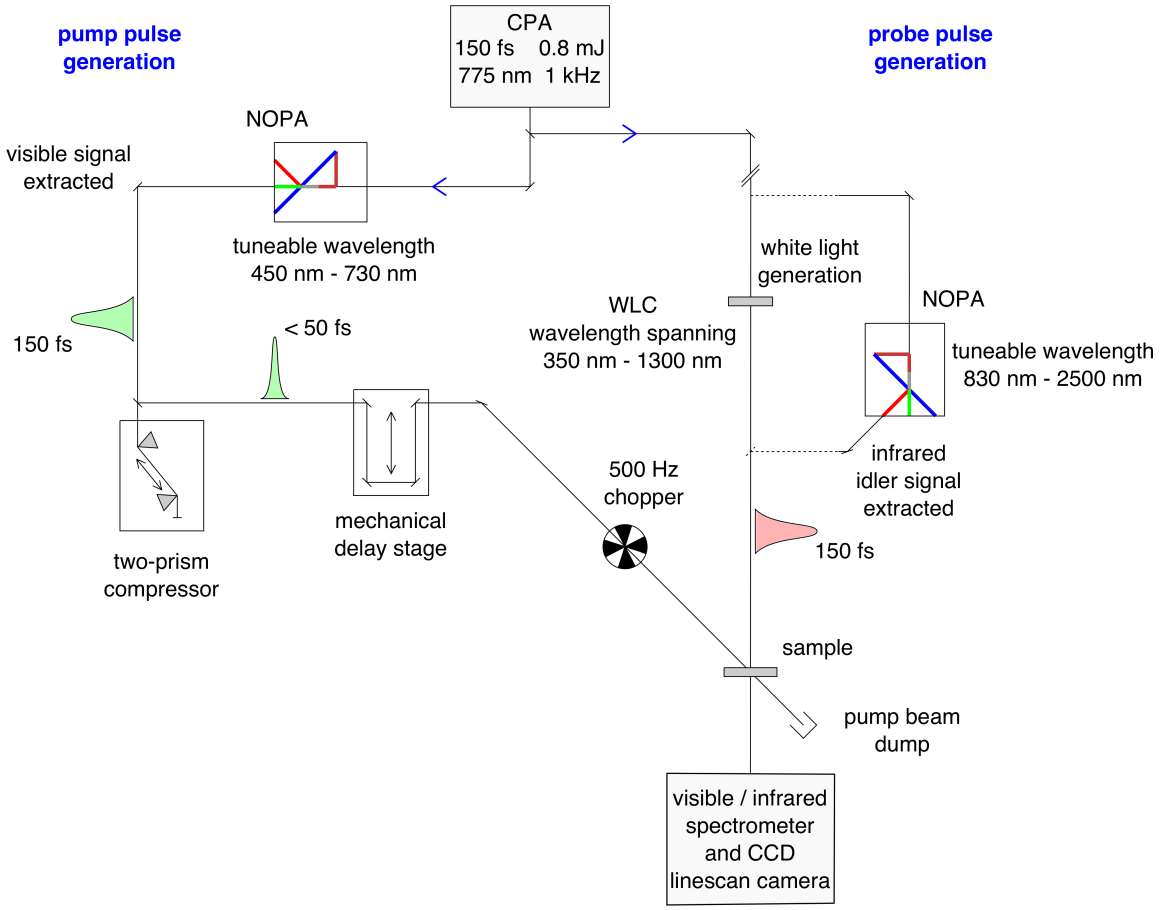

Figure 3.2: A sketch of our pump-probe transient absorption spectroscopy experimental setup in the laboratory. Both the optical pump and optical probe pulses are generated from a common femtosecond chirped pulse amplifier (CPA) laser source. The central wavelength of the pump pulses is tuned with the use of a non-collinear parametric amplifier (NOPA), before they are temporally compressed to below 50 fs. The probe pulses are either broadband white light continua (WLC) or near infrared pulses extracted from the idler signal of a second NOPA setup. The pump and probe pulses are temporally and spatially overlapped in the sample, and the temporal delay between them is adjusted with a mechanical delay stage. Light transmission is recorded with the use of either a visible or an infrared spectrometer and attached charge coupled device (CCD) linescan cameras. This is done for photoexcited samples and referenced against ground state samples with the use of an optical chopper in the pump beam path. In this way, change in optical density $\Delta\mathrm{OD}(\lambda, t)$ spectra similar to the one presented in Figure 3.5 are obtained.

k vector of the 387.5 nm pump pulse.

Therefore, as a result of the conservation of energy and momentum with respect to the group velocity of the photons in the 387.5 nm pump pulse, the amplified signal propagates along the same axis as the WLC seed pulse and an additional infrared signal is generated at a vertical angle with regards to the amplified visible signal. This is referred to as the idler signal and its spatial separation from the amplified signal is advantage of the non-collinear geometry employed. These broadband signal and idler pulses, with central wavelengths spanning from $\lambda = 450$ nm to $\lambda = 2500$ nm, are selected out by means of a mechanical aperture to be used as pump or, as will be explained below, probe pulses in the transient absorption experiment. The typical signal pulse energy is approximately 10 μJ, however if two amplification stages are employed,

signal pulse energies of $20 - 30\ \mu$J are obtained. Please refer to Figure 3.3 for examples of signal and idler pulses which have been generated with the use of our NOPA setup.

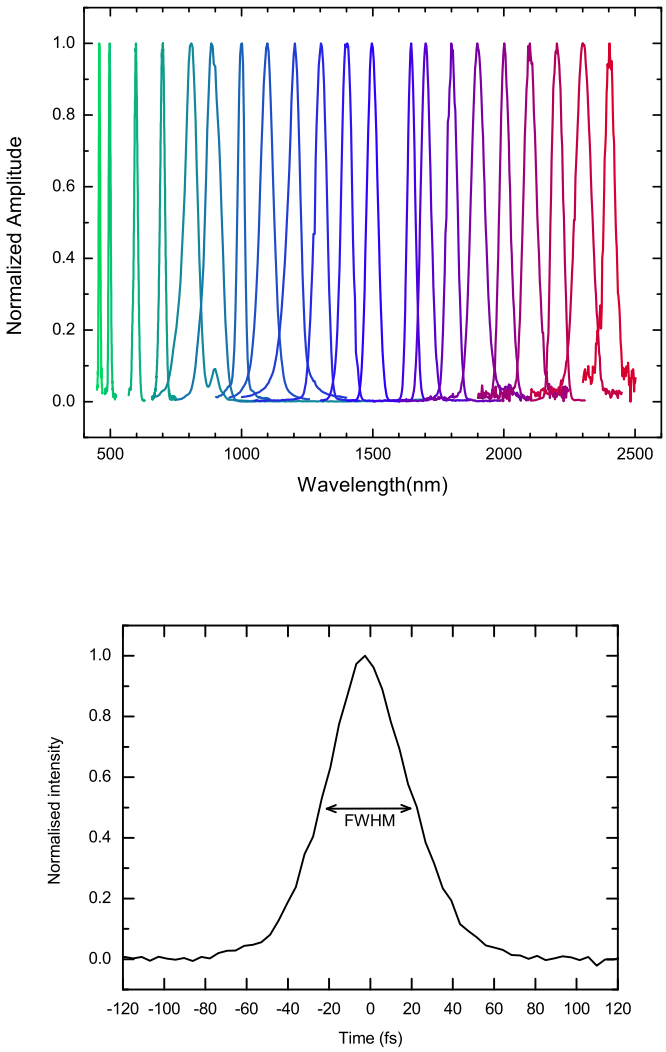

Figure 3.3: Example normalised spectra of pulses generated with the use of a non-collinear parametric amplifier (NOPA) are shown in the figure at the top. The spectra shown in green were obtained from the visible signal produced and their central wavelengths can be tuned from 450 nm – 730 nm. These visible pulses are often employed as pump pulses in our setup. The remaining spectra shown in blue and red correspond to the near infrared idler pulses, and are usually employed as probe pulses. Their central wavelength can be tuned to span the 830 nm – 2500 nm spectral region. The graph below corresponds to an autocorrelation signal of a compressed NOPA pulse centred about 530 nm. From the full width at half maximum (FWHM) of the autocorrelation signal (48 fs), a pulse duration of 34 fs can be calculated.

As an additional note, with the use of this non-collinear parametric amplification technique, the resulting signal pulses are spectrally broad (spectral width of 5% – 7% of central wavelength) and span the spectral region 450 nm – 730 nm. Therefore through the use of a two-prism compressor, the NOPA signal pulses are temporally compressed to a sub 50 fs duration. The corresponding compression limit for a pulse centred around 460 nm is 50 fs, while a 580 nm pulse can be compressed to sub 30 fs.

Please refer to Figure 3.3 for an example autocorrelation signal of a NOPA pulse centred at $\lambda = 530$ nm. The full width at half maximum (FWHM) of the autocorrelation signal is 48 fs, corresponding to a pulse duration of 34 fs.

The pump pulse fluence plays an important role when investigating materials whose dynamics depend on the charge carrier density in a nonlinear manner. This value is presented as an energy per area and is calculated as a ratio of the pump pulse energy to the pump beam focus area. Typical pump fluences which we employ in our experimental setup are in the order of 50 μJcm^{-2} thus relating to a pump pulse energy of 100 nJ and a pump beam focus diameter of 500 μm. The fluence is selected to achieve a large enough absorption change in the spectroscopic signals which we measure (approximately $5 - 10\%$) without inducing additional nonlinear effects such as two photon absorption or stimulated emission within the duration of the pump pulse.

Probe pulses

Approximately 10% of the fundamental pulse energy is directed to be employed in the generation of spectrally broad WLC probe pulses, or 30% in the case of near infrared NOPA probe pulses. The two sections that follow, outline the characteristics of these two types of probe pulses. In addition, for an improved temporal resolution, compressed visible NOPA probe pulses generated in a second NOPA setup are also employed as probe pulses in our laboratory. Although this limits the broadness of the spectrum which can be measured simultaneously (in comparison to a WLC), the temporal resolution which we can achieve is below 100 fs.

White light continua

Spectrally broad, uncompressed white light continuum probe pulses are produced by focusing the fundamental laser beam into one of three nonlinear crystals: 3 mm thick yttrium aluminium garnet (YAG), 3 mm sapphire or 5 mm calcium fluoride (CaF_2). The remainder of the 775 nm fundamental beam is removed from the resulting WLC pulses by means of one of the following dielectric filters: longpass (transmitting $\lambda > 900$ nm), shortpass (transmitting $350 < \lambda < 750$ nm) or notch (centred around $\lambda = 785$ nm). The sapphire crystal is often preferred as the probe pulse in the visible spectral region as the white light supercontinuum generated in this crystal is most stable and therefore results in the best measurement sensitivity.

The spectra of the WLC probe pulse are plotted in Figure 3.4 together with the crystals and filters which were employed in their generation. From the figure, it can be noticed that the use of WLC probe pulses gives us access to spectroscopic signals which appear in the 350 nm – 1300 nm spectral window. Even though the WLC above 1200 nm appears weak, its stability allows excellent TAS measurements, even up to 1400 nm. This, of course, is if the sample does not scatter too much light, but mainly absorbs. However, in order to probe further into the infrared spectral region, spectrally narrower near infrared probe pulses are generated as idler signals with the use of a NOPA as described above.

As a result of the group velocity dispersion (GVD) which takes place following the generation of the WLC in the nonlinear crystals, the white light supercontinuum is positively chirped at the sample. Due to the chirp, the temporal duration of the uncompressed WLC probe pulse is approximately 1 ps, with the temporal duration of its

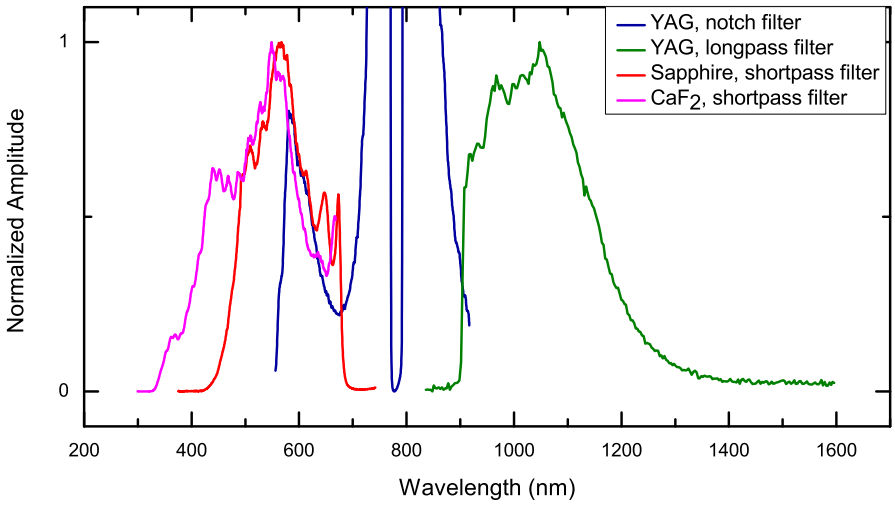

Figure 3.4: Normalised spectra corresponding to white light supercontinuum probe pulses spanning the spectral region of 350 nm – 1300 nm. The spectrum plotted in magenta was obtained from white light generation (WLG) in a CaF_2 crystal and remnant fundamental photons removed with the use of a shortpass dielectric filter (transmitting $350 < \lambda < 750$ nm). The spectrum plotted in red was obtained from WLG in a sapphire crystal and filtered with the use of a shortpass dielectric filter (transmitting $350 < \lambda < 750$ nm). The spectrum plotted in blue was obtained from WLG in a YAG crystal and filtered with the use of a notch dielectric filter (centred around $\lambda = 785$ nm). The spectrum plotted in green was also obtained from WLG in a YAG crystal and filtered with the use of a longpass dielectric filter (transmitting $\lambda > 900$ nm).

spectral components being 150 fs as determined by the duration of the fundamental CPA laser pulses. This chirp can be observed in the TAS measurements and is corrected for manually by shifting the resulting transient absorption spectrum such that the zero time points of all wavelengths coincide. As previously mentioned, the temporal resolution of our experimental technique is below 200 fs for a NOPA pump – WLC probe measurement, as determined by the convolution of the pump and spectral components of the probe pulses in the sample at time zero. It can therefore be observed directly as the temporal width of the time zero coherent artefact present in the transient absorption spectrum.

Near infrared NOPA pulses

The extension of our measurement window further into the infrared spectral region was driven by our experiments on operational dye sensitised solar cells, and the desire to probe the electrons in the conduction band (CB) of ZnO. As introduced in the preceding chapter, these electrons were transferred from the adsorbed photoexcited indoline dye, and are known to have an associated absorption signal above 2000 nm. Our goal was to follow the population dynamics of the ZnO conduction band and learn about the mechanisms underpinning the charge transfer processes from the dye into the ZnO CB.

Initially we attempted to generate a WLC in a YAG nonlinear crystal which could potentially span to beyond 2000 nm, however unsuccessfully. The idea rested on the

fact that this WLC could either be employed directly as a near infrared broadband probe pulse, or as a seed pulse in an additional NOPA, thus producing near infrared amplified signal pulses. The procedure which in the end was most feasible in our laboratory setup, was to employ a visible NOPA and extract the near infrared idler signal to be used as the probe pulse.

As introduced above, the idler signal is generated as a result of the conservation of energy and momentum in the amplification process and therefore contains a distribution of photon energies and momenta. This results in an untidy idler beam mode, which is corrected for with the use of a mechanical aperture. Selecting only a portion of the beam causes a drop in the idler pulse energy, however the amplitude remains sufficiently high to employ the pulse as a probe in our TAS setup. If we optimise the angle and temporal delay between the 387.5 nm pump and WLC seed pulses in the NOPA for stability of the idler signal rather than the visible signal, very stable near infrared pulses are generated tuneable in range of 830 nm – 2500 nm, Figure 3.3. With the use of this manual optimisation, we ensure that we don't sacrifice the sensitivity of our measurement technique. Lastly, the temporal duration of these idler pulses is below 150 fs, therefore we continue to achieve sub 200 fs temporal resolution, even when probing in the near infrared spectral region.

In order to determine the temporal duration of the near infrared idler pulses at the sample position, we employed cross correlation frequency resolved optical gating (XFROG). This procedure entails the frequency mixing of the idler pulse, with unknown amplitude and phase, with a pre-characterised pulse in a 3 mm thick BBO crystal. Varying the temporal delay between the two pulses results in a delay scan, from which we were able to retrieve both the phase and temporal width of the idler pulse. These measurements formed part of the MSc work of E. Ahmed and are presented in great detail in her thesis [124].

3.3 Acquiring transient absorption spectra

Central to the pump-probe architecture in transient absorption spectroscopy, is the temporal delay between the pump and probe laser pulses, which must be very well controlled. In our experimental setup, this is a mechanical delay stage (Newport) which is located in the beam path of the pump laser pulse, refer to Figure 3.2. By taking advantage of the fixed speed of light in air ($c_{\text{air}} = \delta x / \delta \tau$), we mechanically vary the time ($\delta \tau$) between the pump and probe pulses at the sample, to a maximum of 600 ps. The step accuracy of the mechanical delay stage is approximately 2 μm translating into an accuracy of 13 fs as the stage is operated in reflection. Moreover the reproducibility of the delay stage is absolute and approximately 2 μm. Therefore neither the accuracy nor the reproducibility of the delay stage are of any limitation to the experimental technique's temporal resolution as the duration of both the pump and probe laser pulses is much larger.

In order to measure the absorption of a photoexcited material as a function of time, the pump and probe beams are focused and overlapped in the sample, both spatially and temporally. To obtain a better sensitivity in the measurement technique, the probe beam focus is considerable smaller than the pump beam focus. This procedure ensures that the entire probed area has been photoexcited by the pump pulse, and allows us direct access to an absolute measure of the percentage of molecules within the ensemble

which are excited upon illumination. After the sample, the transmitted pump beam is directed to a beam dump and the probe beam is focused into one of two grating spectrometers, sensitive to either the visible or the near infrared spectral regions. Data is collected by means of an attached visible or infrared CCD linescan camera with 1 kHz readout rates (Entwicklungsbüro Stresing Gmbh), which provide a combined spectral window from below $\lambda = 350$ nm to $\lambda = 2500$ nm. As the readout rate of both CCD cameras matches the frequency of the pulse train produced by the CPA, the light transmission can be recorded for every probe pulse individually.

To avoid any nonlinear multiphoton absorption and sample heating effects, it is important to ensure that the material which is being measured relaxes back to the ground state with the period of the laser pulse train. If this relaxation is in the order of, or longer than 1 ms, a fresh sample must be used for each laser shot. This is achieved through the use of a flow cell in the case of a liquid state sample, or a mechanical rotating sample mount in the case of a solid state sample.

In order to separate the dynamic absorption spectrum of the photoexcited sample, from the static absorption spectrum of the sample in its ground state, a simple referencing technique is employed. Before being focused onto the sample, the pump beam is aligned through an optical chopper which blocks out every second pump pulse. This is achieved by setting the operating frequency of the chopper to 500 Hz, half of the operating frequency of the CPA. We therefore detect the transmission spectrum of a pumped sample (I_{pump}), immediately followed by a reference transmission spectrum of a sample in its ground state (I_{unpump}). The change in absorbance (optical density) as a function of wavelength $\Delta OD(\lambda)$ is calculated from the ratio of these two spectra as per Equation 3.1.

$$\begin{aligned} \Delta OD(\lambda) &= OD(\lambda)_{pump} - OD(\lambda)_{unpump} \\ &= -\log\left(\frac{I_{pump}}{I_0}\right) + \log\left(\frac{I_{unpump}}{I_0}\right) \\ &= -\log\left(\frac{I_{pump}}{I_{unpump}}\right) \end{aligned} \tag{3.1}$$

Through this procedure, we record the change in absorbance as a function of wavelength for a given temporal delay ($\delta\tau$) between the pump and probe laser pulses. The resulting $\Delta OD(\lambda, \tau)$ spectrum is generated by combining these change in absorbance temporal slices.

By employing a sufficiently intense and very stable probe pulse, and averaging over 6000 laser shots we obtain a measurement sensitivity in the order of 10^{-4}. This sensitivity is routinely achieved for liquid samples as well as non light scattering thin films, however such high sensitivities are not obtained for highly light scattering greatly absorbing samples such as multicrystalline perovskite thin films.

3.4 A typical transient absorption spectrum

An example transient absorption spectrum, acquired through the experimental procedures outlined above, is shown in Figure 3.5. The change in optical density $\Delta OD(\lambda, t)$ is plotted using a colourmap as a function of wavelength and temporal delay between

the pump and probe laser pulses. Red and blue are used to indicate positive and negative changes in optical density respectively, while green indicates no change in optical density, as can be seen in the spectral region preceding time zero. As a reminder, the change in optical density is determined by subtracting the reference ground state absorbance spectrum of a sample from the excited state absorbance spectrum of the photoexcited sample. With that in mind, a red spectroscopic signal thus indicates an increased absorption (decreased light transmission detected) upon illumination, while a blue signal indicates a decreased absorption (increased light transmission detected). These changes in detected light transmission can be caused by one of the following three processes.

Excited state absorption (ESA) refers to the increased light absorption of the excited sample. These signals correspond to newly populated electronic states upon photoexcitation and are therefore associated with positive spectroscopic signatures (red).

The absorption of newly generated **photoproducts** (for example isomers) will also lead to a decrease in light transmission at the wavelengths associated with the electronic transitions of these materials. These signals correspond to the electronic states of newly produced molecules upon photoexcitation and are therefore also associated with positive spectroscopic signatures (red).

In contrast, **ground state bleaching** (GSB) refers to the decreased light absorption of the sample in its ground state. Upon photoexcitation, fewer molecules are present in the ground state with respect to the reference measurement. Therefore a decrease in absorption is observed at the photon energies corresponding to the ground state absorption bands. In other words, these signals correspond to newly depopulated electronic states upon photoexcitation and are therefore associated with negative spectroscopic signatures (blue).

As our detector simply measures light transmission, **fluorescence by stimulated emission** is also observed as a spectroscopic signal. Fluorescence refers to the radiative relaxation of a molecule from its excited state to the ground state. Our probe pulse stimulates this process in the direction of the detector, thereby an increase transmission is recorded at those particular wavelengths, with respect to the reference measurement. This produces a negative spectroscopic signature (blue) in the transient absorption spectrum. Theoretically, this could also be observed for phosphorescence. However, the yield of phosphorescent photons is too low and their lifetimes too long to be detected using femtosecond TAS. Additionally, while fluorescence signals are often detected for liquid samples, they are not usually observed for our solid state solar cell samples.

The amplitudes of our spectroscopic signals, depend on the relative population of molecules in the various associated states. By following their temporal evolution, we are able to link the observed absorption signals to a kinetic model and learn about the photoinduced charge dynamics which occur in the material under investigation. The oscillator strengths and thus transition probabilities of the transient states are generally unknown, therefore the respective amplitudes obtained from their spectroscopic signatures are not necessarily directly comparable. With that said however, the ground state bleaching signal provides a quantitative measure of the absolute percentage of molecules within our probed measurement area which were excited upon illumination due to the pump pulse (typically 1-2%). This value is directly extracted from the change in optical density ΔOD which relates to the molar concentration of photoexcited molecules in the ensemble (c) via the Beer-Lambert law for transmission

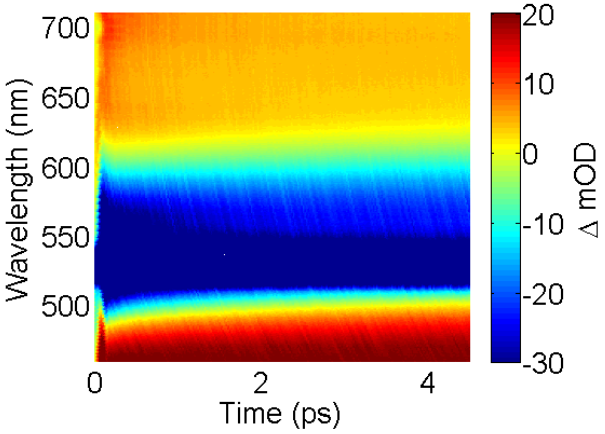

Figure 3.5: An example transient absorption spectrum depicting the change in optical density $\Delta OD(\lambda, t)$ as a function of wavelength and temporal delay between the pump and probe laser pulses, using a colourmap. Red is used to indicate a positive change in optical density (decreased transmission upon photoexcitation) and is characteristic of excited state absorption (ESA) and photoproduct absorption signals. Blue is used to indicate a negative change in optical density (increased transmission upon photoexcitation) and is characteristic of ground state bleaching (GSB) and fluorescence signals. Green indicates no change in optical density and thus no change in transmission.

$T = 10^{-\epsilon lc}$, where $OD = -\epsilon lc$. ϵ is the molar extinction coefficient which is determined by the absorption cross section of the material, and l is the length (thickness) of the sample through which light propagates. So at least for the initially excited state, we are able to determine the oscillator strength.

The temporal dependence of the spectroscopic signatures corresponding to various electronic transitions is visible in the example transient absorption spectrum depicted in Figure 3.5. In order to characterise this temporal behaviour we take a multitude of horizontal traces throughout the entire measured spectral region, and analyse them as a complete system. These lineouts offer us information about the change in optical density as a function of time $\Delta OD(t)$ for a fixed wavelength range. We typically select a 10 nm wavelength range over which we average the data when extracting horizontal traces.

Furthermore, the lineouts, can be related to the charge population and depopulation dynamics of the electronic states to which the associated TAS signatures belong. If these dynamics depend linearly on the charge carrier densities of the electronic states, we fit them with a sum of exponential growth and decay functions of a minimal order of free parameters. In this way, we obtain decay constants and relative amplitudes which are linked via a kinetic model. However, if the processes are characterised by a nonlinear dependence on charge carrier density, a more detailed analysis procedure is required, as is explained in detail in Chapter 7.

To complicate matters further, transient absorption signals often overlap spectrally or shift along the wavelength axis within the duration of our experimental window. Furthermore, the spectral span of one complete measurement often comprises of more than three transient absorption spectra, each acquired using either WLC or near infrared NOPA probe pulses. This, together with the aforementioned nonlinear dependancies observed in some materials, makes the use of an automatic global analysis procedure that simultaneously allows for the deconvolution of the transient absorption spectrum and fits the temporal traces to a kinetic model, virtually impossible. We therefore apply the time consuming manual analogue analysis procedure, which leads

us to developing a charge transfer model as described below.

We first assign all of the spectral signatures in the transient absorption spectrum to allowed, and perhaps already known, electronic transitions in the sample. By fitting their temporal evolutions to a kinetic model, we directly gain information about the photoinduced charge dynamics processes. In this way, we employ TAS to construct the simplest possible fully consistent charge transfer models for perovskite photoabsorbing materials and fully operational dye sensitised solar cells. In the event that the spectral signatures in the transient absorption spectrum were not previously observed, our resulting kinetic model enables us to assign them to electronic transitions in the sample. This was in fact the case for the indoline dye sensitised ZnO solar cells investigated in this work and presented in Chapter 5.

The pump-probe TAS experimental setup described in this chapter was employed together with the analysis procedure detailed above to study the photoinduced ultrafast charge dynamics processes which take place in dye sensitised and perovskite solar cells during the conversion of solar energy to electrical energy. From our charge transfer models, one can learn about the underlying mechanisms and fundamental physics processes responsible for, as well as limiting the generation of an electrical current with the use of these photovoltaic devices. The chapters which follow first introduce the samples which were investigated in this study, together with some of their macroscopic electrochemical characteristics. Immediately following, our results are directly presented in the form of charge dynamics models, and are succeeded by a detailed discussion of our analysis.

4. Dye Sensitised Solar Cells

We investigated two different types of fully operational dye sensitised solar cells (DSSCs) in this study, containing either a liquid electrolyte solution or a solid hole conductor. Two example cells are presented in the photographs of Figure 4.1. Both types of cells contain the same photoanode: a highly porous ZnO nanostructure electrodeposited onto a fluorine-doped tin oxide (FTO) coated glass slide, sensitised with the organic indoline dye DN216. As is evident in the photos, the indoline pigment is bright pink in colour and therefore has a strong absorption in the green spectral region. The sample shown on the left hand side was fabricated as a sandwich cell with an additional FTO coated glass slide as the cathode, and a liquid electrolyte solution. The sample shown on the right hand side of the photograph, contains a solid hole conducting material layer which was spin coated over the photoanode as well as four silver fingers which form the cathode.

This chapter serves to introduce the chemical composition of the different samples together with their fabrication methods. The samples were all made in the material science group of Prof. D. Schlettwein at Justus-Liebig Universität in Giessen, Germany. Some spectroelectrochemical measurements will also be presented in this chapter, followed by previous transient absorption spectroscopy results obtained by myself and our research group [38, 39].

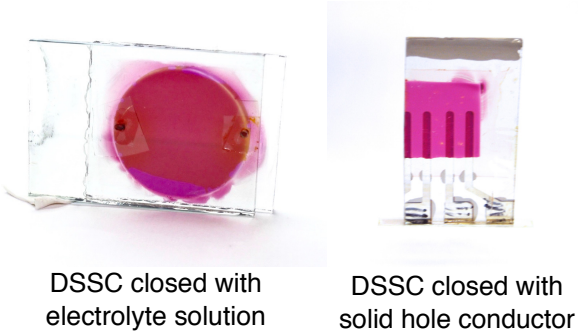

Figure 4.1: Photographs of example fully operational DSSCs which were investigated in this work. Both cells were fabricated with a highly porous ZnO electrode sensitised with the organic indoline dye DN216. The device on the left was closed with the iodide/triiodide redox couple in electrolyte solution and sealed as a sandwich cell with a fluorine-doped tin oxide (FTO) coated class slide as the cathode. The device on the right was closed with the solid hole conductor Spiro-OMeTAD and four silver fingers as the counter electrode. The transparency of the cells was not optimised to maximise the photocurrent conversion efficiency of the cells, but rather for transient absorption spectroscopy in transmission.

4.1 The possible charge transfer processes

The basic working principle of DSSC solar cells was already introduced in the introductory chapter (Chapter 2). It will therefore only be repeated here briefly. The sketch shown in Figure 4.2 depicts the basic charge transfer processes which occur in DSSCs in the conversion of solar energy to electrical energy with blue arrows. Upon photoexcitation (process 1), an electron hole pair is generated in each excited dye molecule adsorbed to the surface of the ZnO. The electrons are injected out of the dye's lowest unoccupied molecular orbital (LUMO) and into the ZnO conduction band (CB) thereby generating oxidised dye molecules (process 2). These electrons in the ZnO CB are then free to be extracted into the external circuit towards the cathode in order to produce an electrical current (process 3). The circuit of the cells is traditionally closed with an electrolyte solution containing a redox couple. The purpose of the redox couple is to reduce the oxidised dye molecules (process 4). It is itself reduced at the cathode (process 5). The maximum voltage extractable from the cell, also referred to as the open circuit voltage in an I-V measurement, is determined by the potential difference between the quasi-Fermi energy of the ZnO under illumination and the Nernst potential of the redox couple and is typically $0.6 - 0.7$ V for indoline dye sensitised ZnO solar cells.

In the event that a solid hole transport material is rather used to close the circuit of the cell, the oxidised dye molecules are reduced through hole injection from the highest occupied molecular orbital of the dye (HOMO) into the HOMO or valence band (VB) of the hole conducting material. The maximum voltage extractable from the cell is then given by the potential difference of the quasi-Fermi energy of the ZnO under illumination and the HOMO or VB energy of the hole transport material.

Unfortunately the conversion of solar to electrical energy with the use of DSSCs is not 100% efficient, even after taking into account the inherent fundamental losses due to the Shockley-Queisser limit. Counter charge transfer process are also present in these devices and are depicted in Figure 4.2 with red arrows. The photoexcited dye molecule can relax back into its ground state (process 6). This monomolecular recombination process is also referred to as geminate recombination. Additionally, the electrons which have already been injected into the ZnO CB can recombine to reduce oxidised dye molecules (process 7), or even with the redox couple in the electrolyte solution (process 8). Both these channels are bimolecular and can also be referred to as non-geminate recombination processes.

An additional counter process which is not depicted in the sketch, but must also be accounted for when striving to improve DSSC device efficiencies, is the trap mediated recombination of electrons in the ZnO CB. It is known that electrodeposited ZnO contains shallow band gap trap states due to impurities as well as additional surface trap states. The presence of these states can cause the trapping of electrons before they are extracted to the external circuit and adds a possible recombination path between the trap state and the oxidised dye molecules or the redox couple. As will be expanded on in detail in the chapter to follow, the presence of trap states on the ZnO surface plays an important role in the electron injection from photoexcited dye molecules into the ZnO CB.

The charge transfer pathways presented above and in Figure 4.2 occur with different characteristic time constants, ranging from the femtosecond injection of photoexcited electrons into the ZnO CB (process 2), all the way to the microsecond regeneration

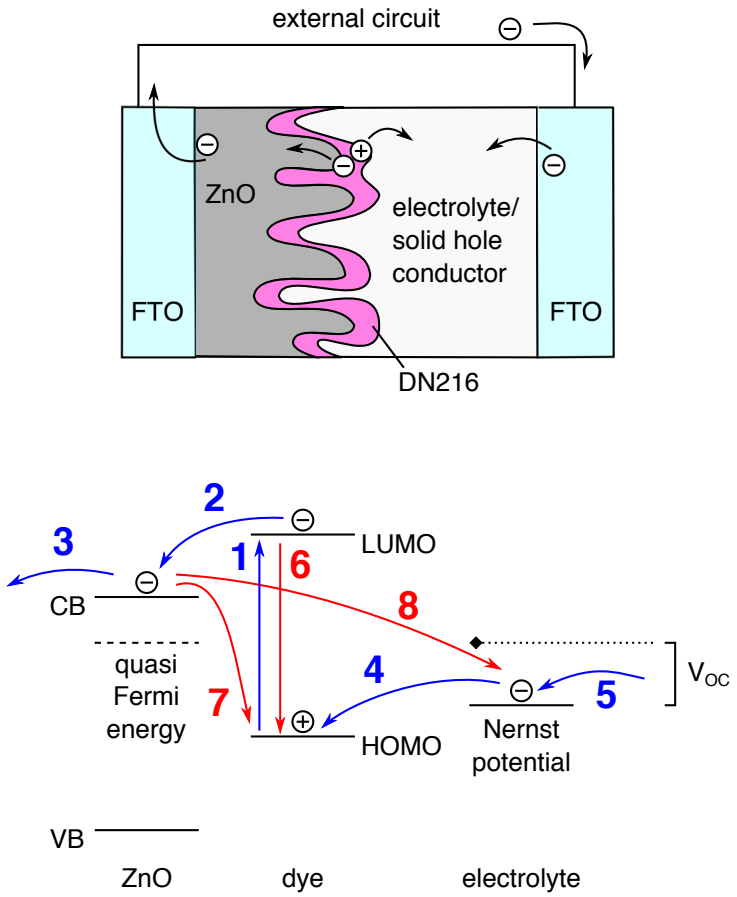

Figure 4.2: Exaggerated sketch of a typical DSSC sample closed with electrolyte solution (above) together with a simplified energy diagram (below), depicting the processes which take place in DSSCs in the conversion of solar energy to electrical energy. In the sketch, the highly porous ZnO is shown together with the monolayer of indoline dye DN216 as well as the volume filled by electrolyte solution, sandwiched between the fluorine-doped tin oxide (FTO) coated class slides. The energy diagram is drawn to depict the conduction (CB) and valence band (VB) energies of the ZnO and the lowest unoccupied molecular orbital (LUMO) and highest occupied molecular orbital (HOMO) of the DN216 dye. The maximum voltage extractable from the cell is shown above as the potential difference between the quasi-Fermi energy of the ZnO under illumination and the Nernst potential of the redox couple. The **desired processes** are shown on the sketch and in blue on the energy diagram and include: **1** photoexcitation of the dye generating an electron hole pair, **2** electron injection from the dye's LUMO into the ZnO CB, **3** the extraction of electrons into the external circuit, **4** reduction of the oxidised dye molecules, **5** reduction of the redox couple at the cathode. The **counter processes** are not shown on the sketch, and depicted in red on the energy diagram and include: **6** relaxation of the photoexcited dye back to its ground state, **7** recombination of electrons in the ZnO CB with oxidised dye molecules, **8** recombination of electrons in the ZnO CB with the redox couple.

of redox couple at the cathode (process 5). Therefore these lifetimes must be investigated with different measurement techniques. As explained in Chapter 3, femtosecond transient absorption spectroscopy (TAS) allows us to follow the processes which occur on the femtosecond and picosecond time scales. These include the electron injection from the dye into ZnO (process 2) and the relaxation of the photoexcited dye back to its ground state (process 6). The reduction of oxidised dye molecules (process 4) takes place on the nanosecond timescale and is therefore only observed as a baseline in our measurement window (600 ps).

The aforementioned cycle, is theoretically infinitely repeatable without a chemical alteration to the dye molecules. In reality however, a limited number of turnovers can

take place due to the dye's chemical and photo stability. For a DSSC lifetime of approximately 20 years in average outdoor conditions, the turnover of the dye employed needs to be in the order of 10^8 cycles – a number easily achieved by the traditional ruthenium based organometallic complexes [2].

4.2 The fabrication of our DSSC samples

As mentioned above the fabrication of the dye sensitised solar cell samples which we investigated in our laboratory as part of this work was carried out by our project collaborators in Giessen, Germany. The following subsections detail the fabrication procedure briefly. The fabrication of DSSCs together with our collaborators formed a substantial part of my MSc research. Therefore a comprehensive, stepwise explanation of the solar cell devices I fabricated is given as part of my MSc thesis [39].

Working electrode

In general, the working electrode of our DSSC samples comprises of a highly porous ZnO nanostructure which was electrodeposited onto an FTO coated glass slide. The glass slide requires the fluorine-doped tin oxide coating for conductivity. The photoanode's absorption is sensitised towards lower photon energies through the adsorption of a monolayer of indoline dye to the surface of the ZnO. As pointed out above, the characteristic absorption of the dye is in the green spectral region, see Figure 4.3 for a steady state absorption spectrum.

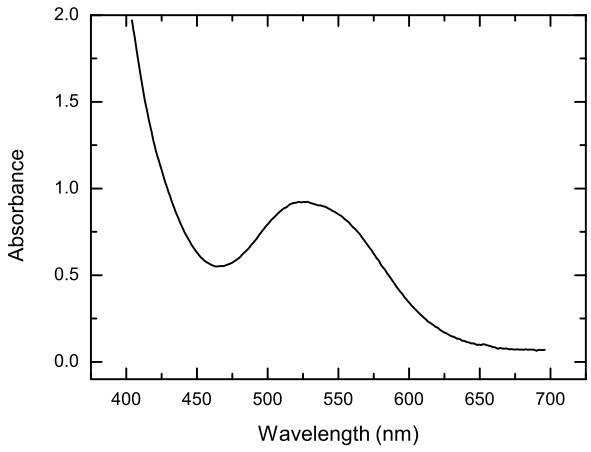

Figure 4.3: The steady state absorption spectrum of a photoanode consisting of an electrodeposited highly porous ZnO nanostructure sensitised with the organic indoline dye DN216. As is evident in the photos of Figure 4.1, the indoline pigment is bright pink in colour and therefore has a strong absorption in the green spectral region at $\lambda = 530$ nm. The high energy absorption edge is caused by the ZnO absorption maximum centred at $\lambda = 387$ nm.

Dye aggregates hamper the transfer of charge, as the excitonic energy transfer within these dye networks is not efficient . Furthermore, it has been shown that for efficient electron injection to take place between the photoexcited dye and ZnO, the LUMO of the dye must overlap with the ZnO CB [125]. Additionally, the oxidised dye molecules

need to be in contact with the electrolyte solution in order to be reduced. Therefore the dye must be adsorbed to the surface of the ZnO as a monolayer. If the semiconductor was to be deposited as a bulk thin film, the surface area which is available to be loaded with dye is extremely small. This is the primary reason why the efficiencies of DSSCs were restricted to approximately 1% before the revolutionary paper of O'Regan and Grätzel [23]. Their introduction of a highly porous semiconductor nanostructure lead to a surface enhancement of 2000 fold and a resulting increase of power conversion efficiency (PCE) to above 7%.

The electrodeposition of ZnO is well established and has been reported in great detail, including as part of my MSc work [38, 39, 41, 126–128]. It is achieved by means of a three electrode setup in 70°C KCl aqueous solution with the help of the structure directing agent EosinY, which is subsequently desorbed. The resulting films are approximately 5 μm thick, with a 10 nm pore size (determined by the agglomerate size of EosinY).

The indoline dye is subsequently adsorbed to the ZnO surface by immersion of the pre-treated electrode in a dye solution. The solution is made up in a 1:1 acetonitrile and tert-butyl alchohol solvent, and consists of 0.5 mM DN216 indoline dye in 1 mM lithocholic acid. The presence of the acid has been shown to aid against the formation of dye aggregates. Optimal dye loading time in terms of producing cells with a maximum short circuit current density (exceeding 12 $mAcm^{-2}$) and thus highest PCEs, is approximately 10 minutes. However, the resulting films are too light absorbing and scattering to be used in TAS measurements in transmission as the change in optical density sensitivity is reduced to above 10^{-1}. So for the purpose of our experiments, we measured samples which were only submerged in the dye solution for 1 minute. Although this results in a noticeable drop in the short circuit current density, and therefore in poor efficiencies compared to state of the art DSSCs, the ultrafast charge dynamics responsible for light to electrical energy conversion are unaffected. Ideally, an absorption of $80 - 90$ % is preferred in order to avoid nonlinear excitation. This is achieved in the sample measured in Figure 4.3.

Please refer to Figure 4.4 for the chemical structure of the organic indoline dye DN216 which was employed in all the DSSC samples studies in this work. The absorbing chromophore contains the indoline moiety as depicted in the image. Furthermore, two carboxyl anchor groups are present, which allow for the dye to adsorb to the ZnO surface. The traditional indoline dye (D149) which was used with ZnO only contains one carboxyl anchor group. It would therefore desorb from the ZnO surface in the presence of the electrolyte solution after a few weeks. The addition of the second anchor was done to increase the dye's adsorption to the ZnO surface and thus the lifetime of the solar cells to approximately 2 years. As will be explained in more detail below, the distance of the carboxyl group anchors with respect to the absorbing chromophore of indoline dyes influences the lifetime of the electron injection from the photoexcited dye into the ZnO CB. On the other hand, the absorbing chromophore of both dyes is the same, thus resulting in an identical absorption maximum and therefore very similar spectroscopic signatures.

To date, thousands of different dyes and dye derivatives have been investigated as possible sensitisers in the context of DSSCs. Perhaps the future success of DSSCs lies with the diversity which can be achieved in terms of working electrodes, electrolyte solutions, and hole transporting materials.

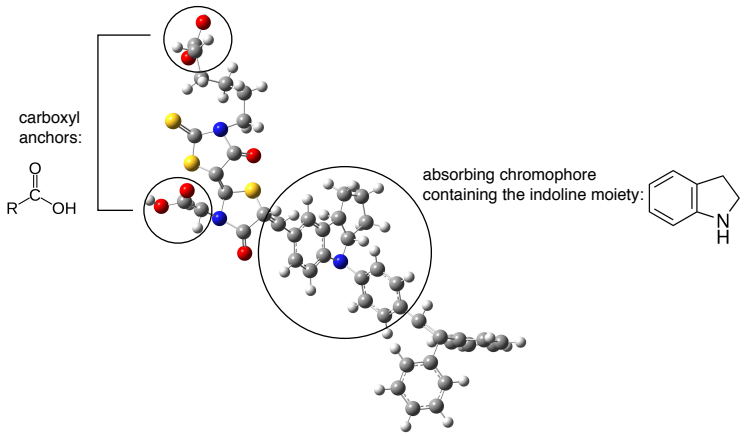

Figure 4.4: The chemical structure of the organic indoline dye DN216. The absorbing chromophore is shown in the diagram together with the chemical structure of the indoline moiety it contains. The two carboxyl anchor groups which bind the dye to the ZnO surface are also pointed out together with the carboxyl functional group chemical structure.

Completing the cell

Traditionally, DSSCs are closed with a liquid electrolyte solution which contains the idodide/triiodide redox couple. A portion of our DSSC samples were closed with this electrolyte solution, in particular 0.5 M 1-methyl-3-propylimidazolium iodide and 50 mM I_2 in acetonitrile. As mentioned above, it has been observed that the liquid electrolyte solution is corrosive thus causing the indoline dye molecules to desorb from the surface of the ZnO. Once in solution, the photoexcited dye can no longer inject electrons into the ZnO and the overall PCE of the solar cell drops drastically. In addition to the inclusion of another carboxyl anchor group in the synthesis of the dye to counteract this problem, the liquid electrolyte solution can also be replaced with a more chemically inert material, such as a solid hole conductor.

The DSSC samples which contain the liquid electrolyte solution, were made as sandwich cells between two FTO coated glass slides. While the fabrication of the photoanode was described above, the cathode was simply made by sputter depositing platinum over the FTO coating of the glass. This platinum layer is approximately 50 nm thick and it functions as a catalyst to speed up the reduction of the redox couple at the cathode. Once the counter electrode is sealed onto the working electrode with the use of a spacer film, the electrolyte solution is added by means of vacuum backfilling through two pre-drilled holes in the cathode.

For the remaining portion of our DSSC samples, the organic solid hole conductor Spiro-OMeTAD was employed in the fabrication procedure. The chemical structure of 2,2′,7,7′-tetrakis-(N,N-di-4-methoxyphenylamino)-9,9′-spirobifluorene, more commonly known as Spiro-OMeTAD is presented in Figure 4.5. To deposit the hole transport layer, 40 μL of a solution containing Spiro-OMeTAD was spin coated onto the working electrode at 3000 rpm for 30 s. The solution consists of 180 mg/mL Spiro-OMeTAD (Borun Chemicals, 99.75%), 6.4 mg/mL lithium bis(trifluoromethanesulfonyl)imide (Li-TFSI, Sigma-Aldrich, 99.5%), 30 mg/mL acetonitrile (Roth, 99.9%) and 16 mg/mL tert-butylpyridine (Sigma-Aldrich, 99%) in chlorobenzene (Roth, 99.5%). For counter electrodes, four silver fingers (100 nm thick) were evaporated over the hole transport layer. The DSSC samples studied in this work, which were fabricated with the double anchor dye (DN216) and closed with Spiro-OMeTAD, continue to be fully operational thus

suggesting that cell lifetimes exceeding 3 years are attainable in this way.

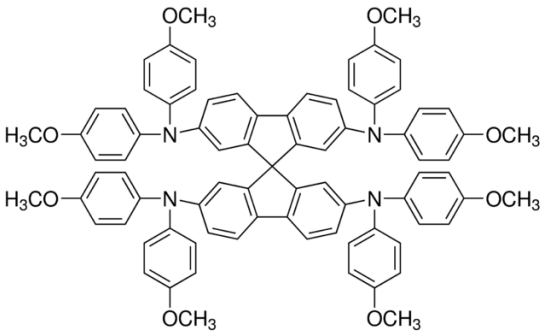

Figure 4.5: The chemical structure of the organic hole transport material Spiro-OMeTAD. When produced as a thin film, the way it is employed in our solar cell samples, this organic solid has an associated hole mobility of 1.69×10^6 cm^{2}V^{-1}s^{-1} [129]. Furthermore, in dichloromethane solution, Spiro-OMeTAD has two absorption maxima centred at $\lambda = 306$ nm and $\lambda = 385$ nm.

In terms of the TAS measurements which we carried out in this work, we observed that the shapes of the spectral signatures of the DSSCs closed with the liquid electrolyte solution were the same as those of the cells made with Spiro-OMeTAD, in the visible spectral region. Furthermore the associated temporal evolutions of these spectroscopic signatures was the same within our temporal measurement window, irrespective of whether the cell was closed with the iodide/triiodide redox couple in solution or Spiro-OMeTAD. This is not surprising as the spectral and temporal changes brought upon by regeneration are much slower than attainable through our ultrafast measurement technique. It is however not always the case. Previous measurements which were carried out in our research group, found that the time constant associated with the injection of photoexcited electrons into ZnO depends on the size of supplementary ions added to the iodide/triiodide electrolyte solution [38].

As will be relied on in Chapter 5, two differences were observed between the two sets of transient absorption spectroscopy measurements. The first is that the iodide/triiodide liquid electrolyte solution absorbed heavily in the near infrared spectral region and spectra could thus not be acquired at wavelengths larger than 1400 nm. The second is that the data collected from the cells closed with Spiro-OMeTAD was not as clean in the visible spectral range due to the overlapping absorption background caused by oxidised Spiro-OMeTAD with associated absorption maxima at $\lambda = 420$ nm, $\lambda = 510$ nm and a very broad absorption peak centred at $\lambda = 700$ nm [130]. For these reasons, the data acquired from all the measurements was combined and the neatest examples are presented in Chapter 5.

4.3 Our previous measurements on indoline DSSCs

In previous work, we carried out spectroelectrochemical and transient absorption spectroscopy measurements on a series of DSSCs sensitised with one of the three novel indoline dyes DN91, DN216 and DN285 and compared the results to our first investigations of D149 in solution and operational sensitised ZnO solar cells. Please refer to Figure 4.6 for the chemical structures of these indoline dyes. DN91, DN216 and DN285 were synthesised with an additional carboxyl anchor group in comparison to D149. As

mentioned above, this was done in order to decrease the desorption of the sensitiser with time, and in turn increase the stability of the cells from a few weeks to a couple of years.

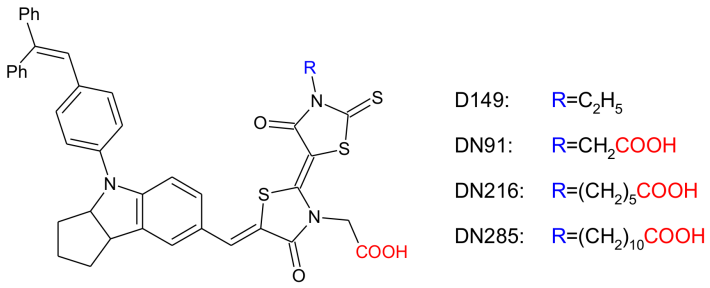

Figure 4.6: The chemical structure of the organic indoline dyes D149, DN91, DN216 and DN285. They all contain the same absorbing chromophore and initial carboxyl anchor group. The R group on the sketch is different for the four molecules: D149 contains an alkyl chain, while DN91, DN216 and DN285 contain a second carboxyl anchoring group attached to an alkyl chain of varying length. This figure was obtained from one of our previous studies [41].

As this second anchor is attached to an alkyl chain of increasing length for DN91, DN216 and DN285, it is assumed that the three respective dyes' spatial orientation on the ZnO surface differs, and thus so does the orbital coupling between the dye molecules and the ZnO. While the open circuit voltage (V_{OC}) of these devices is independent of the sensitiser employed, we observed a noticeable difference in the short circuit current densities (J_{SC}): the shorter the alkyl chain connected to the second carboxyl anchor, the higher the J_{SC} measured for the devices. As a result, this trend was also observed in the measured power conversion efficiencies of the devices. Please refer to Figure 4.7 for example I-V curves obtained from cells sensitised with either DN91, DN216 and DN285.

Transient absorption spectroscopy enabled us to investigate a microscopic reason responsible for the link between the alkyl chain length of the dye and the PCE obtained from the device sensitised with that respective dye. We noted that the ultrafast direct electron (approximately 200 fs) out of the indoline dye's LUMO and presumably into the ZnO CB was fastest for the best performing dye (DN91) and slowest for the dye containing the largest alkyl chain (DN285). Furthermore, we observed that the electron injection measured for the devices sensitised with DN285 was comparable to that of devices sensitised with the traditional D149 indoline dye. This therefore suggested that the addition of a second anchor group greatly increases the cell stability, but only aids with electron injection if the anchor is close enough to the absorbing chromophore.

Furthermore, from the decay of the dye's excited state absorption, we observed that electrons are injected out of the dye's LUMO on two distinct timescales (approximately 200 fs and 2 ps). This lead us to believe that the injection of electrons may occur directly, but also via an intermediate charge transfer state. Prior to the measurements presented in this work, see Chapter 5, we were however unable to probe the ZnO CB population and depopulation dynamics. The spectroscopic signature related to the absorption of CB electrons is in the near infrared spectral region above 200 nm[32, 34, 131], and our experimental setup did not allow for probing beyond 1300 nm. Following the development of a near infrared probe pulse source, we could therefore investigate the ZnO CB filling and learn more about the intermediate charge transfer states previously undetected.

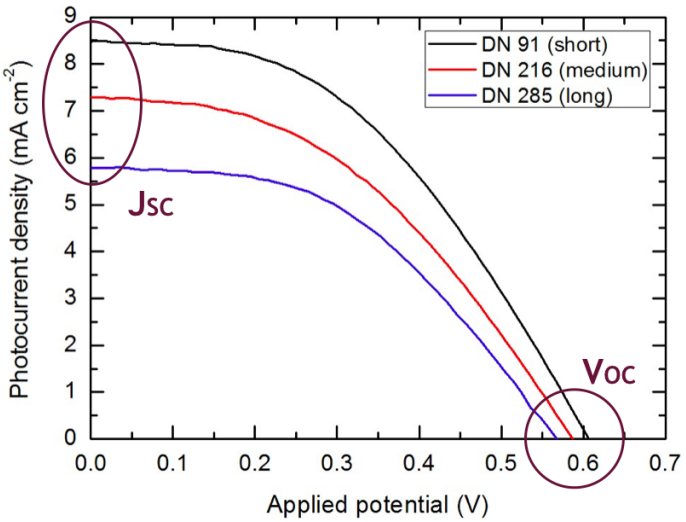

Figure 4.7: Three example I-V curves obtained for DSSCs sensitised with either DN91(short alkyl chain to second anchor), DN216 (medium alkyl chain to second anchor) or DN285 (long alkyl chain to second anchor). The short circuit current density (J_{SC}) for these cells is marked off together with the open circuit voltage (V_{OC}). The J_{SC}s obtained for these devices are lower that the typical expected value of approximately 12 mAcm^{-2} as the dye loading time was reduced to 1 minute versus the usual 10 minutes to optimise the cells for TAS in transmission. Moreover, while the V_{OC}s are very similar for these cells, the trend in J_{SC}s follows the trend in alkyl chain lengths: the lower the J_{SC}, the longer the alkyl chain length connected to the second carboxyl anchor. This figure was obtained from one of our previous studies [39].

4.4 Expected spectroscopic signatures

From our previous work on indoline dyes (D149, DN285, DN216, DN91), both in solution and as sensitisers in fully operational solar cells, we are able to build a sketch of the expected spectroscopic signatures of the DN216 dye sensitised solar cells in the visible regime, refer to Figure 4.8. The assignment of the ground state bleaching (GSB) signal was directly inferred from the absorption maximum of the indoline dyes (530 nm) (Figure 4.3), while the assignment of the excited state absorption (ESA) centred at 675 nm was as a result of transient absorption measurements carried out on the indoline dye D149 in solution [38, 40]. The oxidised dye absorption signal (OX) was observed at 480 nm, and a wing of its broad absorption at 675 nm, as expected from the absorption spectrum of chemically oxidised D149 dye molecules in solution. This measurement was carried out by our project collaborators in Giessen, Germany [132].

The chapter which follows will explain, in detail, the simplest consistent charge transfer model obtained from the transient absorption measurements of the fully operational DSSCs introduced above. From measurements in the visible and near infrared spectral regions, we were able to describe the kinetics which occur upon photoexcitation, specifically in indoline dye sensitised electrodeposited ZnO solar cells.

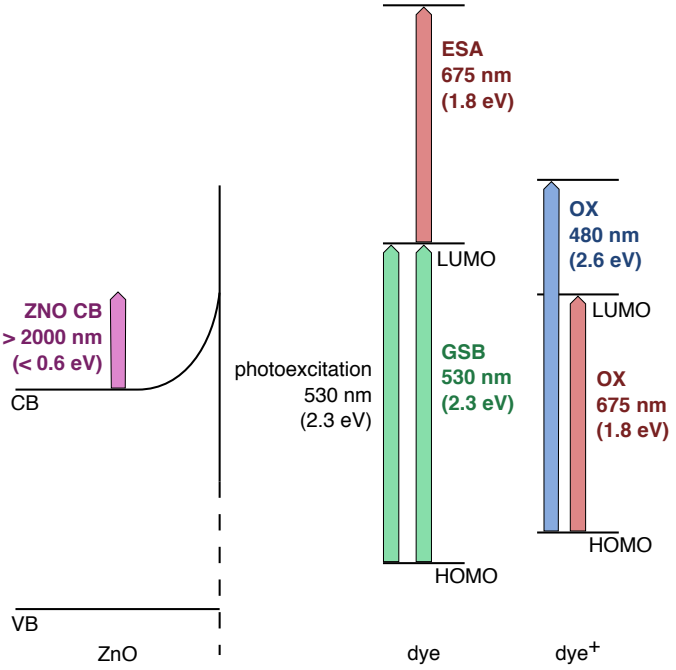

Figure 4.8: A simple energy level diagram indicating the TAS spectroscopic signatures which are expected upon photoexcitation of a DN216 sensitised ZnO solar cell device. The conduction (CB) and valence (VB) bands of the ZnO are plotted together with the lowest unoccupied (LUMO) and highest occupied (HOMO) molecular orbitals of the dye and oxidised dye. The ground state bleaching (**GSB**) of the neutral dye corresponds to its absorption maximum (530 nm), the excited state absorption (**ESA**) of the neutral dye is observed at 675 nm, the absorption of the oxidised dye (**OX**) is observed at 480 nm as well as overlapping with the ESA signal at 675 nm, and the absorption of electrons in the **ZnO CB** is expected above 2000 nm.

5. Transient Absorption Spectroscopy of Dye Sensitised Solar Cells

We followed the charge transfer processes which occur in organic dye sensitised solar cells (DSSCs) immediately following photoexcitation, in real time, with the use of transient absorption spectroscopy (TAS), as described in Chapter 3. In particular, our samples consisted of an indoline dye sensitised electrodeposited ZnO photoanode in contact to either the iodide/triiodide redox couple in liquid electrolyte solution or the solid hole conductor Spiro-OMeTAD. For further details about the working electrode, the electrolyte solution and solid hole conductor as well as the fabrication of these solar cells, please refer to Chapter 4.

In order to build a simplest possible and consistent charge transfer model, we linked the visible and infrared spectral signatures, related to the allowed electronic transitions of the sample, to a kinetic model. This chapter serves to show the charge transfer model together with our TAS results and the detailed analysis procedure that lead us to that particular model. Although unconventional, I will first present the charge transfer model, and save the results, reasoning and detailed analysis to follow for interested parties.

5.1 Charge transfer model

The diagram in Figure 5.1 is a schematic representation of the energy levels of the ZnO, indoline dye DN216 and the iodide/triiodide redox couple or Spiro-OMeTAD taking part in photoinduced charge generation within the DSSC devices investigated in this work. In addition to the conduction (CB) and valence (VB) bands, the surface of electrodeposited ZnO is known to be electronically characterised by surface states, from which the intermediate charge transfer states depicted in the diagram originate. They are differentiated into two categories depending on their electronic nature: ionic charge transfer states (ICT) shown in purple, and neutral charge transfer states (NCT) drawn in orange, and explained in more detail in the subsection bellow.

The maximum voltage extractable from the cell (V_{OC}, typically $0.6 - 0.7$ V) is also shown and is given by the potential difference between the quasi-Fermi energy of the ZnO under illumination and the Nernst potential of the redox couple or highest occupied molecular orbital (HOMO) of the Spiro-OMeTAD. Favourable processes in terms of charge generation and extraction are shown in blue, while counter processes are depicted in red. All processes which do not occur on our timescale are shown in grey.

The charge transfer process explained below are depicted with arrows in Figure 5.1 and occur in indoline dye sensitised electrodeposited ZnO solar cells in the conversion of solar energy to electrical energy.

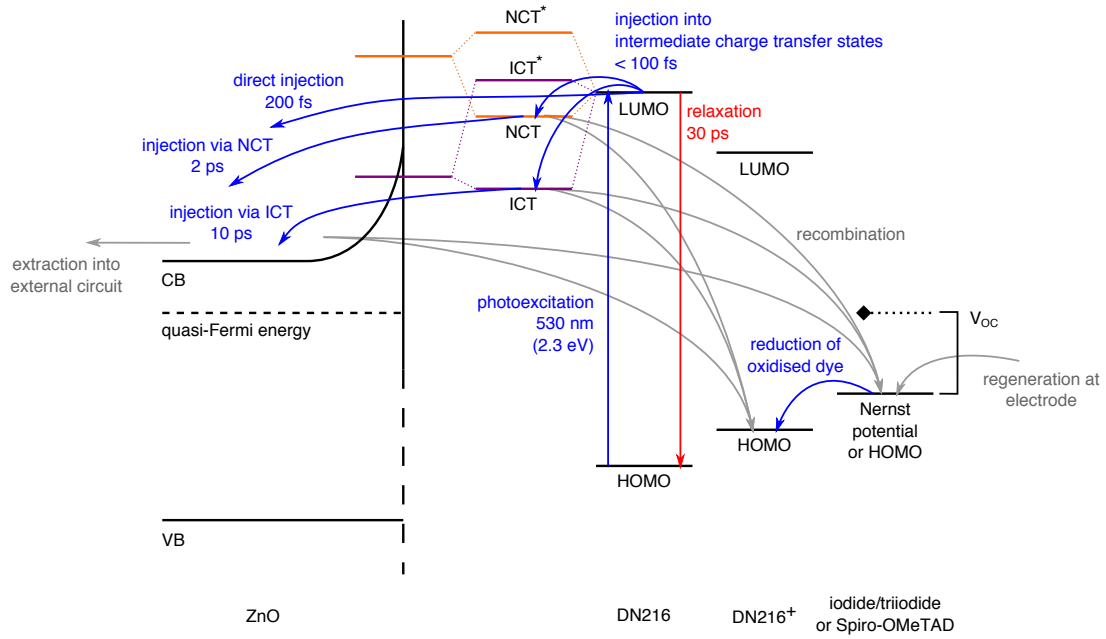

Figure 5.1: A sketch of the conduction (CB) and valence (VB) bands of ZnO and quasi-Fermi level under illumination, together with the highest occupied (HOMO) and lowest unoccupied (LUMO) molecular orbitals of the indoline dye DN216 which take part in the initial photophysics governing DSSCs. The bonding and anti-bonding orbitals of the intermediate neutral (NCT) and ionic (ICT) charge transfer states are also depicted, as well as the Nernst potential of the iodide/triiodide redox couple. In the case of all-solid DSSCs, this level is rather representative of the HOMO energy of Spiro-OMeTAD. The open circuit voltage V_{OC} can also be seen on the diagram, as well as the charge transfer processes which occur upon photoexcitation: aiding towards charge generation (blue), counter processes (red) and kinetics which don't occur on our fs-ps timescale (grey).

Upon illumination with a laser pulse centred around $\lambda = 530$ nm (2.3 eV), thus corresponding to the absorption maximum of the indoline dye DN216, an electron is photoexcited from the neutral dye's highest occupied molecular orbital (HOMO) into its lowest unoccupied molecular orbital (LUMO). The photoexcited electron is either directly injected into the ZnO CB with a time constant of 200 fs, or it is injected into one of the two types of charge transfer states with an associated time constant smaller than 100 fs. While the direct injection into the ZnO CB or into the ICT state immediately generates an oxidised dye molecule, the injection into the NCT state does not. The subsequent injection from one of the two possible charge transfer states into the ZnO CB occurs with two distinct time constants of 2 ps for the higher lying NCT state and 10 ps for the lower energy ICT state. In the case of electron injection from the NCT state into the ZnO CB, an oxidised dye molecule is generated. Once in the ZnO CB, the electrons can be extracted into the external circuit, thus generating an electrical current. The oxidised dye molecules are reduced by the redox couple in the electrolyte solution or the solid hole conductor on a nanosecond timescale, which are themselves reduced at the cathode to close the external circuit on a microsecond timescale.

In addition to the aforementioned processes, some charge transfer pathways counter to cell optimisation occur on ultrafast timescales and cannot be excluded. The most prominent of which, in this temporal regime, is the relaxation of the photoexcited dye back to its ground state with a characteristic time constant of 30 ps. Moreover, the recombination of electrons from within the ZnO CB or from a charge transfer state, with either the redox couple in the electrolyte solution or with oxidised dye molecules is also

found to occur, although on much longer timescales than our measurement window.

Intermediate charge transfer states

As mentioned above, surface trap states are characteristic of electrodeposited ZnO [32, 34]. In the context of the charge kinetics discussed here, these can be differentiated into two categories depending on their energy relative to the LUMO of the neutral indoline dye: high energy surface trap states and low energy surface trap states.

Since the dye is adsorbed to the surface of the electrodeposited ZnO nanostructure as a monolayer, almost all excited DN216 dye molecules are attached to the ZnO surface via two carboxyl group anchors, therefore resulting in distinct orbital molecular configurations and various possible overlap geometries. According to previous charge transfer measurements on coumarin dyes adsorbed to ZnO, hybrid orbitals are generated at the ZnO | dye molecule interface resulting from the overlap of the LUMO and either a higher or a lower lying surface trap orbital. In this way two separate sets of bonding and anti-bonding orbitals are generated, see Figure 5.2.

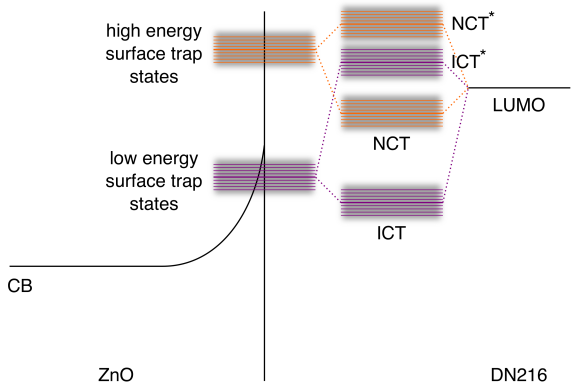

Figure 5.2: The hybrid bonding and anti-bonding orbitals which form due to the overlap of the neutral dye's lowest unoccupied molecular orbital (LUMO) and the trap states present on the surface of electrodeposited ZnO. The resulting intermediate charge transfer states, which take part in electron injection, are either more neutral in nature – resulting bonding orbital is electronically more similar to the LUMO of the dye (NCT, drawn in orange), or ionic – the resulting bonding orbital is electronically more similar to the ZnO surface state (ICT, drawn in purple).

As can be seen in the schematics of Figures 5.1 and 5.2, in the case of overlap between the LUMO and a higher energy surface trap, the resulting bonding hybrid orbital is most alike in energy and thus electronic character to the neutral dye's LUMO. The resulting intermediate charge transfer state (shown in orange) is referred to as a neutral charge transfer state (NCT) as it is electronically very similar to the excited state of the neutral dye. In contrast, the bonding hybrid orbital generated from overlap between the LUMO and a lower energy surface trap, is closer in energy and thus electronic character to the lower energy surface trap. The population of the resulting intermediate charge transfer state (shown in purple) causes the electron density to favour the ZnO surface rather than the neutral dye and is therefore referred to as an ionic charge transfer state (ICT).

5.2 Detailed analysis

As already outlined in Chapter 3, our analysis procedure is as follows: We first acquire transient absorption spectra in the visible and near infrared spectral regions with the various probe pulses available. The observed spectral signatures are then assigned to known allowed electronic transitions in the sample, and a multitude of temporal lineouts covering the entire spectral region are obtained. By comparing our kinetic model with the temporal evolution of the spectroscopic signals, we learn about the photoinduced charge dynamics processes and construct the simplest possible charge transfer model which is fully consistent. Additional spectral signatures, which were not previously known or expected, are then analysed in parallel with the charge transfer model to assign new electronic states in the sample.

The following subsections depict the step for step analysis procedure outlined above together with additional control measurements.

The transient absorption spectrum

The transient absorption spectrum presented in Figure 5.3 comprises of a selection of measurements taken, together with their respective probe pulse spectra. As explained in Chapter 3, the change in optical density of the sample is plotted using a colourmap as a function of both wavelength and temporal delay between the pump and probe laser pulses. Sections a and b were recorded with the use of narrowband infrared NOPA probe pulses centred at $\lambda = 2150 \pm 20$ nm and $\lambda = 1600 \pm 20$ nm, therefore only a limited portion of the entire spectral signature is observed. On the other hand, sections c to f were recorded with broadband white light continua (WLC) probe pulses generated in either a sapphire or a YAG crystal ($900 - 1300$ nm and $450 - 750$ nm), therefore multiple spectral signatures are present in one measurement. The small spectral region between 700 nm and 900 nm was probed with a YAG crystal WLC and a notch dielectric filter (centred around $\lambda = 785$ nm). Some of these spectral signatures have been well studied, while others were not yet assigned prior to this work.

The potion of the absorption signal observed around 2150 nm corresponds to the absorption of electrons in the conduction band of the ZnO as they are known to absorb in the infrared spectral region above 2000 nm (section a) [32, 34, 131]. The excited state absorption (ESA) of the neutral indoline dye DN216 has a characteristic absorption centred about 675 nm, superimposed with a side band of the oxidised dye absorption signal (OX) as seen in section d and measured in our previous TAS experiments. The ground state bleaching signal (GSB) of the neutral dye is observed at 530 nm as expected from its steady state absorption maximum (section e), while the two wings of the oxidised dye absorption signal centred about 440 nm are observed at 480 nm (section f) and overlapping with the ESA signal at 675 nm, as introduced in Chapter 4. In addition, two spectrally broad transient absorption features in the region spanning 800 nm to 1800 nm (sections b and c) were not assigned prior to this work. From their temporal behaviour, we were attributed these absorption signals directly to the population and subsequent depopulation of the neural and ionic charge transfer states.

In order to investigate the temporal behaviour of the spectroscopic signals, we took horizontal lineouts of change in optical density as a function of time across the entire probed spectral region. These traces are integrated over a spectral range of 20 nm, and are discussed in the following section.

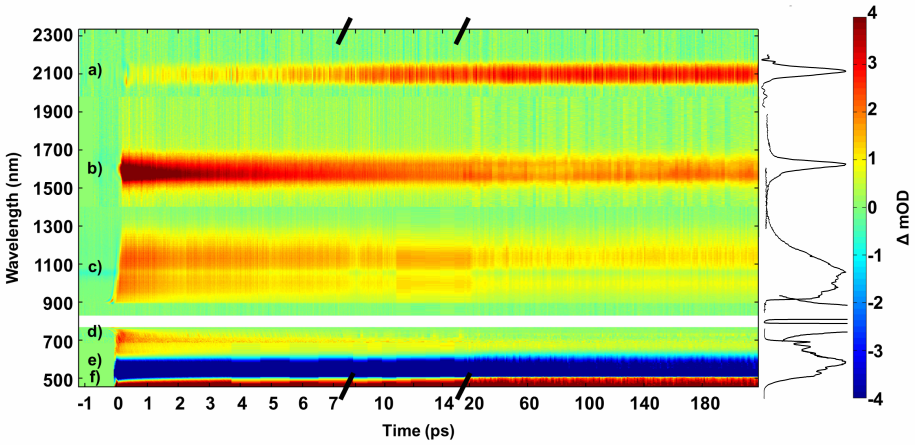

Figure 5.3: A collection of five ultrafast transient absorption spectra of a DN216 sensitised electrodeposited ZnO solar cells contacted to Spiro-OMeTAD (sections a to c) or electrolyte solution (sections d to f), plotted together with the associated probe pulse spectra. Sections a and b were recorded with NOPA probe pulses and thus only display a portion of the spectroscopic signals, and sections c to f were recorded with white light continua probe pulses. We plot the change in optical density (ΔOD) as a function of wavelength and time, on three separate timescales: red indicates an increase in absorption and blue a decrease in absorption upon photoexcitation. The spectral signatures or portions thereof are labeled in the figure and correspond to the: a) absorption of electrons in the ZnO conduction band (ZnO CB), b) neutral charge transfer state (NCT), c) ionic charge transfer state (ICT), d) excited state absorption of the neutral dye overlapping with a wing of the oxidised dye absorption signal (ESA+OX), e) ground state bleaching of the neutral dye (GSB) and f) oxidised dye absorption (OX).

In reality, many measurements were acquired in the spectral region spanning from 400 nm to 2400 nm, especially beyond 1300 nm to compensate for the narrow bandwidth of the NOPA probe pulse in comparison to the WLC. All these transient spectra were analysed manually as one system to compile the complete charge transfer model presented above. The selection of measurements in Figure 5.3 as well as the example temporal lineouts, are representative of the spectral signatures which we observed in the full set of measurements. They were selected at wavelengths with least spectral overlap between different signals, to help explain our reasoning behind the charge transfer model presented above.

Temporal traces

Figure 5.4 is a collection of selected temporal traces corresponding to the transient signals in the absorption spectrum of Figure 5.3. The charge dynamics which occur in DSSCs upon photoexcitation depend on charge carrier density linearly. The temporal evolutions of the transient signals were thus followed mathematically by fitting the traces with a sum of exponential growth and decay functions. From the time constants we obtained lifetimes for the different states which take part in charge generation, separation and extraction in these DSSCs.

Additionally, because many separate measurements were combined, we cannot compare amplitudes throughout the spectral region, but rather just within each WLC probe measurement. And even in that case, the only absolute number of molecules contributing to the signal, is the one obtained in the ground state bleaching (further details are given in Chapter 3). To easier observe the relative amplitude contributions in the various traces, they have all been normalised.

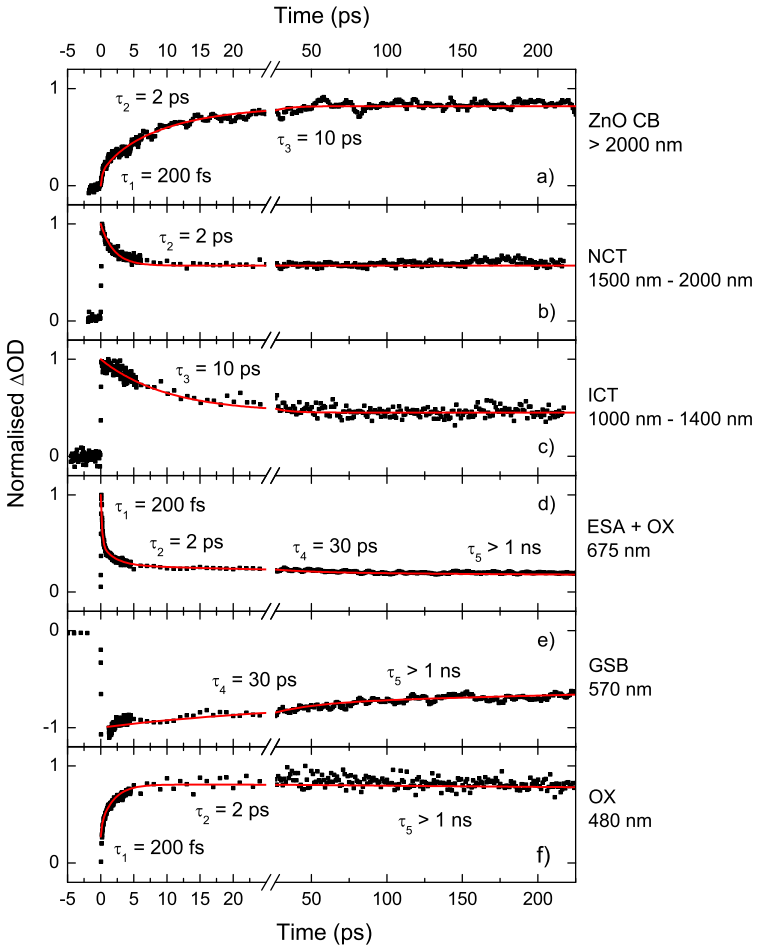

Figure 5.4: A collection of six example normalised lineouts corresponding to the spectral signatures of Figure 5.3: a) absorption of ZnO conduction band electrons, b) neutral charge transfer state, c) ionic charge transfer state, d) excited state absorption of the neutral dye and overlapping wing of the oxidised dye absorption, e) ground state bleaching of the neutral dye and f) absorption of the oxidised dye. The temporal evolution of these lineouts is fitted with a sum of exponential growth and decay functions (red line) and the resulting time constants are presented for each trace.

Link to kinetic model

Electrons in the ZnO conduction band

The line out taken at $\lambda = 2150 \pm 20$nm (section a, Figure 5.4) will be used as the starting point of the analysis and interpretation of all of the spectral components present. It corresponds to the spectroscopic signature assigned to the absorption of free electrons in the ZnO conduction band as measured with an infrared NOPA probe pulse (section a, Figure 5.3). These free electrons were injected into the ZnO CB from the excited neutral dye molecules rather than originating from the direct resonant excitation of ZnO by virtue of the energy of the pump laser pulse (2.3 eV, $\lambda = 530$nm) being smaller than the ZnO optical band gap energy (3.2 eV, $\lambda = 387$nm).

From the multi-exponential growth fit function of this line out (section a, Figure 5.4), three distinct time constants were obtained for the population of the ZnO CB with free electrons thus suggesting three separate charge transfer processes: an ultrafast channel

with a characteristic time of 200 fs, and two slower stepwise channels with characteristic times of 2 ps and 10 ps. These three times are shown with arrows in the kinetic model of Figure 5.5, where the state labelled B is the ZnO conduction band.

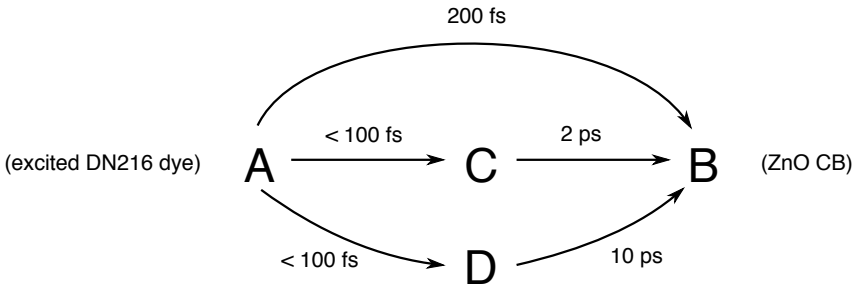

Figure 5.5: The kinetic model of electron injection in indoline dye sensitised electrodeposited ZnO solar cells, which was employed together with the temporal evolution of the spectroscopic signals to generate a simplest fully consistent charge transfer model. **A** represents the photoexcited dye and **B** the ZnO conduction band. With our ultrafast TAS measurements, we assigned **C** and **D** to the neutral and ionic intermediate charge transfer states respectively.

The decay of this signal cannot be observed within our 600 ps measurement window. It corresponds to the extraction of electrons into the external circuit which occurs on a longer timescale.

The ultrafast injection channel

The direct unhindered injection of electrons from the vibrationally cold LUMO of the photoexcited neutral dye into the conduction band of the ZnO, was assigned the time constant of 200 fs. The ultrafast charge transfer process can be likened to the well studied direct injection of electrons from a photoexcited ruthenium based dye into nanoporous TiO_2. Moreover, this interpretation is supported by the ultrafast decay of the neutral dye's ESA signal (section d, Figure 5.4) corresponding to the depopulation of its excited state, together with a mirrored rise in the absorption signal of the oxidised dye molecules (OX), as generated directly through the injection of electrons out of the neural dye's LUMO, see section f of Figure 5.4.

This ultrafast direct electron injection from the photoexcited dye into the ZnO CB is depicted in the kinetic model of Figure 5.5, where the state labelled A is the photoexcited dye.

The stepwise injection channels

The two remaining stepwise processes shown in Figure 5.5, with associated time constants of 2 ps and 10 ps were assigned to the injection of electrons out of the neutral (state C) and ionic (state D) charge transfer states respectively and explained as follows.

The **faster** of these two processes, with a characteristic time of 2 ps, was interpreted as the two step electron injection from the neutral dye's LUMO into the ZnO CB via the NCT state. The fist step comprises of photoexcited electrons being injected into the NCT state with a time constant smaller than 100 fs, at the limit of our temporal resolution. Subsequently, these electrons are injected into the ZnO CB with a characteristic time of 2 ps. Due to the similar electronic character of the bonding orbital of the NCT

state and the LUMO of the neutral dye, as described above, the ultrafast < 100 fs injection into the NCT state does not have an influence on the population of photoexcited molecules, and as a result also not on the population of oxidised dye molecules. Therefore this time constant is not observed in the traces assigned to the excited state absorption of the neutral dye, nor to the absorption of the oxidised dye. However, the 2 ps injection from the NCT into the ZnO CB was observed as a decay in the neutral dye's ESA signal (section d, Figure 5.4), as well as a complimentary rise in the absorption signal (OX) of the oxidised dye molecules (section f, Figure 5.4). Therefore indicating that oxidised dye molecules are only generated through the second 2 ps step of the two stepwise process.

In contrast, the **slower** 10 ps process was assigned to the two step injection of electrons from the neutral dye's LUMO into the ZnO CB via the lower lying ICT state. The fist step was once again assigned to the injection of photoexcited electrons out of the neutral dye's LUMO and into the ICT state with a time constant smaller than 100 fs, at the limit of our temporal resolution. While the succeeding injection of these electrons into the ZnO CB was allocated the slower 10 ps characteristic time. Unlike the injection via the NCT state, the ultrafast < 100 fs time constant is observed as a decay in the neutral dye's ESA signal (section d, Figure 5.4), as well as a mirrored rise in the OX trace (section f, Figure 5.4), while the slower 10 ps second step injection time constant is not present in either of the two ESA or OX signals. The lack of the 10 ps decay in both the ESA and OX traces, confirms the explanation that oxidised dye molecules are already generated through the injection of electrons out of the neutral dye's LUMO and into the bonding orbital of the ICT state, which is most similar in electronic character to the ZnO surface traps.

Moreover, the kinetic model employed (Figure 5.5) can be simplified and used together with sum of exponential rise and decay functions for two reasons. Firstly, the charge transfer processes which we follow in DSSCs using TAS don't depend on the charge carrier density in a nonlinear manner. Secondly, and perhaps more importantly, the time constants associated to the stepwise processes are one to two orders of magnitude different from one another. Therefore the A–B, A–C and A–D processes are mostly complete before, the C–B and D–B processes dominate. This independence between the first and the second set of processes, thus allows for the simplification of the dynamics employed in tis analysis.

In this way, all three time constants causing the rise of the ZnO CB signal (section a) and mirrored as decays in the ESA and OX signals (sections d and f, Figure 5.4) could consequently be assigned.

Relaxation of the photoexcited dye

From the temporal trace corresponding to the excited state absorption of the neutral dye (section d, Figure 5.4) an additional decay time constant of 30 ps was extracted. This time was assigned to the relaxation of photoexcited neutral dye molecules back into their ground state, as it was also observed as a repopulation time of the wing of the ground state bleaching (GSB) signal centred around 530 nm, shown in section e of Figures 5.3 and 5.4. The centre of this transient feature is unfortunately covered due to pump light scattered into the spectrometer off the solid state samples, therefore the wing at 570 nm was used to determine its temporal evolution. By comparing the relative amplitudes of the decay times, we were further able to infer that while 80% of

the photoexcited electrons are injected into the ZnO conduction band, the remaining 20% account for the undesirable relaxation.

Reduction of the oxidised dye

Finally the oxidised dye is in turn reduced via the iodide/triiodide redox couple or Spiro-OMeTAD on a timescale larger than 1 ns. This time constant can be seen in the repopulation of the GSB signal (section e, Figure 5.4) together with the decay of both wings of the oxidised dye absorption signal, at 480 nm (section f, Figure 5.4) and overlapping with the ESA signal at 675 nm (section d, Figure 5.4). It appears as though the reduction of the oxidised dye occurs on similar timescales irrespective of the contact used – iodide/triiodide redox couple in liquid electrolyte solution versus Spiro-OMeTAD, however we were not able to measure any time constants due to the termination of our measurement window at 600 ps.

Spectral signatures of charge transfer states

Furthermore, the existence of the neutral and ionic charge transfer states has so far only been deduced indirectly from the charge dynamics observed in the neutral dye's excited state, the oxidised dye and the ZnO conduction band absorption signals. With the use of our transient absorption measurements, we were able to directly assign the absorption of these suggested charge transfer states to two new spectrally broad positive signatures observed in the spectral region spanning from 1000 nm to 2000 nm, and therefore monitor the population and depopulation thereof, see sections b and c, Figures 5.3 and 5.4. As a reminder, Figure 5.3 only contains a selection of probed regions, although the full range between 900 nm and 2400 nm was probed by gradually tuning the central wavelengths of the infrared NOPA probe pulses and subsequently studied.

By analysing the temporal traces corresponding to the two distinct charge transfer states, we observed an instantaneous rise ($<$ 100 fs) in both signals, corresponding to the ultrafast injection of photoexcited electrons from the neutral dye's LUMO into both types of intermediate charge transfer states. Moreover, the trace shown in section b of Figure 5.4 corresponding to the spectral signature between 1500 nm and 2000 nm (section b, Figure 5.3) was found to decay with a characteristic time of 2 ps and its associated transient signal was therefore attributed to the absorption of electrons in the bonding orbital of the NCT. On the other hand, the line out corresponding to the spectral signature between 1000 nm and 1400 nm (section c, Figures 5.4 and 5.3) was observed to decay with a time constant of 10 ps and its corresponding transient signal was assigned to the absorption of electrons in the bonding orbital of the ICT.

Absorption of oxidised Spiro-OMeTAD

Upon further investigation, it was also noted that the two aforementioned signals do not decay to zero within our measurement timeframe of 600 ps. This apparent baseline was found to be caused by the spectral overlap with the slowly decaying positive absorption signal of the oxidised Spiro-OMeTAD present in the all-solid DSSC samples. In addition to the two absorption peaks of oxidised Spiro-OMeTAD in the visible spectral region, it is also known to have a broad absorption centred at $\lambda = 1400$ nm [133]. To confirm our assignment, we compared the results of the measurements taken on

the DSSC samples in contact with the liquid electrolyte solution, and observed that the NCT absorption signal (section c, Figure 5.4) decayed to zero, while the ICT absorption signal (section b, Figure 5.4) could not be measured due to the high absorbance of the iodide/triiodide redox couple in the near infrared spectral region.

The fully consistent charge transfer model

The final step of our analysis procedure consists of the combination of our kinetic model with the temporal evolution of the spectroscopic signals. A schematic depicting this process is shown in Figure 5.6. The electronic states of ZnO, the indoline dye DN216 and the redox couple or Spiro-OMeTAD, which take part in the initial photophysics are shown together with the spectroscopic signatures observed in the transient absorption spectra. The ZnO CB (pink), ESA (red), OX (blue) and GSB (green) signals corresponding to known electronic transitions are all marked off in the diagram, as well as the newly observed NCT (orange) and ICT (purple) signatures. Furthermore the time constants associated with the filling of a state are labelled as (+) in the sketch and the depopulation time constants observed are marked with a (-). However, the times obtained from the temporal decay of the negative amplitude GSB are rather marked as (+), as they refer to the repopulation of the ground state. Furthermore, only the charge transfer processes which can be observed in our TAS measurements are shown in the diagram, using black arrows.

By linking the (-) time constant from the origin of an arrow, to the (+) time constant at the arrowhead, we assigned times to the various photoinduced charge dynamics processes and constructed the simplest possible charge transfer model which is fully consistent, as presented in Figure 5.1 at the beginning of this chapter.

Aluminium oxide control measurements

We carried out an additional control measurement in order to confirm that the neutral and ionic charge transfer states arise from molecular and surface dominated hybrid orbitals at the dye|ZnO interface, rather than the signals corresponding to triplet states of the DN216 dye. In other words, as a consequence of the orbital overlap between the neutral dye's LUMO and surface traps present on the surface of the electrodeposited nanoporous ZnO film and is not a characteristic of the DN216 dye itself. This was done by preparing thin films of a DN216 monolayer adsorbed onto an aluminium oxide (Al_2O_3) structure. As the energy of the Al_2O_3 conduction band lies above that of the neutral DN216 dye's LUMO, very limited electron injection was expected to occur following photoexcitation of the DN216 dye with a pump laser pulse centred around 530 nm.

No positive absorption signal was detected in the near infrared spectral region spanning from 1000 nm to 2000 nm, thus confirming the presence of the neutral and ionic charge transfer states were generated as a result of the surface traps at the ZnO|dye boundary and are not merely an intrinsic characteristic of the indoline dye DN216.

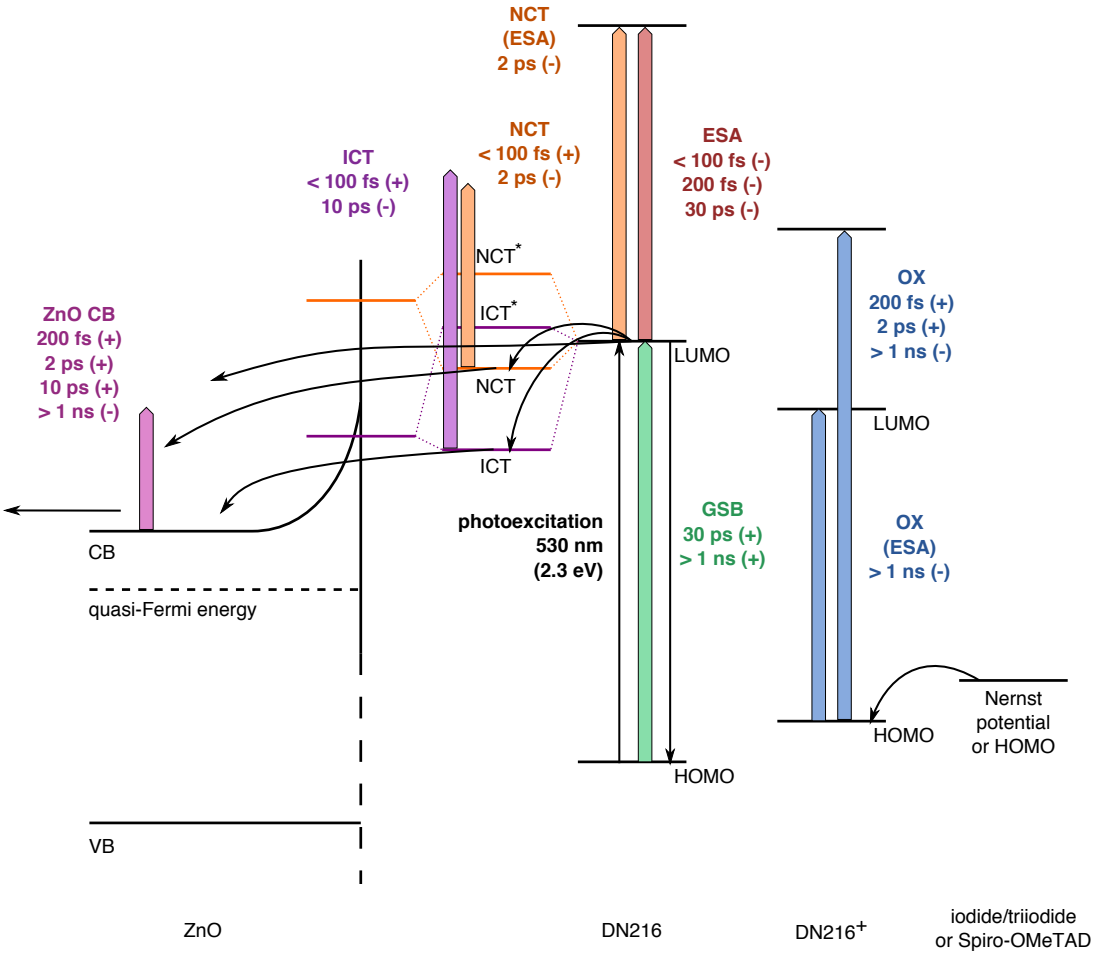

Figure 5.6: A sketch of the conduction (CB) and valence (VB) bands of ZnO and quasi-Fermi level under illumination, together with the highest occupied (HOMO) and lowest unoccupied (LUMO) molecular orbitals of the indoline dye DN216 which take part in the initial photophysics governing DSSCs. The bonding and anti-bonding orbitals of the intermediate neutral (NCT) and ionic (ICT) charge transfer states are also depicted, as well as the Nernst potential of the iodide/triiodide redox couple. In the case of all-solid DSSCs, this level is rather representative of the HOMO energy of Spiro-OMeTAD. The black arrows depict the charge transfer processes which can be observed with our measurement technique. The diagram also depicts the known spectroscopic signatures corresponding to: ZnO CB (pink), ESA (red), OX (blue) and GSB (green), as well as the newly observed NCT (orange) and ICT (purple) signatures. The time constants associated with the filling of a state are labelled as (+) and the depopulation time constants are marked with a (-). The temporal decay of the negative amplitude GSB is rather marked as (+), corresponding to the repopulation of the ground state. To construct our charge transfer model, we link the (-) time constant from the origin of an arrow, to the (+) time constant at the arrowhead, and assign the time constant to the charge transfer channel.

6. Perovskite Thin Films

In the second part of this study, we investigated the photoinduced charge dynamics which take place in mixed perovskite photoabsorbing materials. The samples comprise of a perovskite thin film which was spin coated onto a glass slide and encapsulated to protect it from moisture in the air. A photograph of a typical sample is shown in Figure 6.1. The samples were all made in the material science group of Prof. D. Schlettwein at Justus-Liebig Universität in Giessen, Germany. This chapter aims to present the thin film samples which we employed for our measurements, together with their chemical compositions, deposition methods as well as typical macroscopic characterisation results.

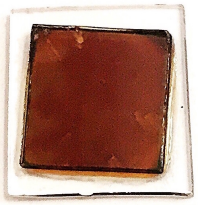

Figure 6.1: A photograph of a typical $FA_{0.85}MA_{0.15}PbI_{2.55}Br_{0.45}$ thin film sample. The brown microcrystalline mixed perovskite was spin coated onto a glass slide and encapsulated with the use of a second glass slide sealed with epoxy. The area of the samples was typically 1 cm^2 and the thickness approximately 200 nm to ensure enough light transmission for transient absorption spectroscopy in transmission.

6.1 The perovskite photoabsorber

As previously introduced, a perovskite photoabsorber is identified by the cubic crystal structure shown in Figure 6.2. The monovalent cation is typically organic as in the case of methylammonium (MA^+) or formamidinium (FA^+), or inorganic as in the case of Cs^+. Please refer to Figure 6.3 for the chemical structure of the organic cations. This cation is surrounded by eight divalent metal cations coordinated to halogen octahedra. The divalent metal ions commonly used are Pb^{2+} and Sn^{2+} and the halogen ions are traditionally I^-, but Cl^- and Br^- are also used.

Although the most commonly employed perovskite photoabsorber is methylammonium lead iodide ($MAPbI_3$), perovskites are also synthesised with a mixture of the aforementioned ions in various ratios. The chemical composition of the mixed perovskite materials which were at the focus of our investigation contain 85% formamidinium and 15% methylammonium as the monovalent cations, lead as the divalent

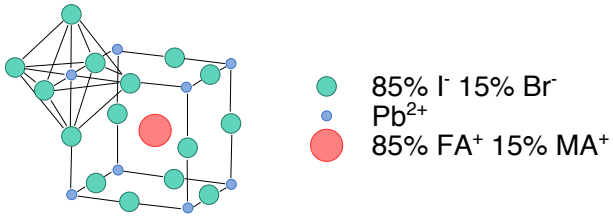

Figure 6.2: The cubic crystal structure of perovskite materials. In our samples, the central monovalent cations (red circles) were a mixture of 85% formamidinium (FA^+) and 15% methylammonium (MA^+). These organic cations are surrounded by eight lead atoms (blue circles) coordinated to halogen octahedra. Our samples contained a mixture of halogen anions (green circles) in the ratio of 85% iodine to 15% bromine anions.

metal cation, and a mixture of 85% iodine and 15% bromine anions, as depicted in Figure 6.2. The formamidinium ions (ionic radius approximately $1.9 - 2.2$ Å) are slightly larger than the methylammonium ions (ionic radius approximately 1.8 Å).

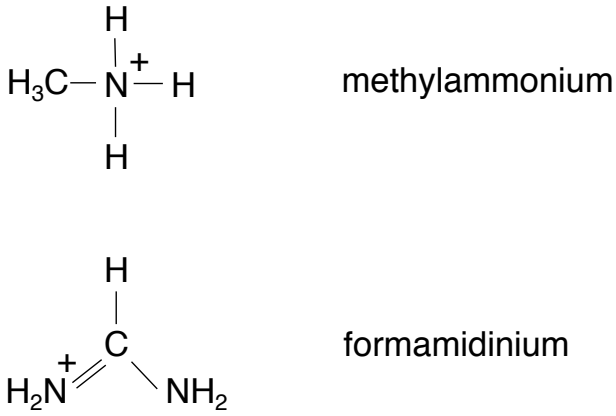

Figure 6.3: The chemical structures of the monovalent organic cations used in our perovskite materials. Formamidinium (ionic radius approximately $1.9 - 2.2$ Å) is slightly larger than methylammonium (ionic radius approximately 1.8 Å).

This particular composition, $(FAPbI_3)_{0.85}(MAPbBr_3)_{0.15}$, was selected due to the fact that solar cell devices made with this perovskite photoabsorber exhibited power conversion efficiencies (PCEs)of 17.9%, the highest certified values at the time our study commenced in 2015 [55]. Since then, PCEs of 21.3% have been achieved with $(FAPbI_3)_{0.85}(MAPbBr_3)_{0.15}$ by the addition of a wider band gap $FAPbBr_{3-x}I_x$ perovskite layer between the primary mixed perovskite and the hole transport material (HTM). The addition of this so called surface passivation layer reduces the electron hole recombination at the perovskite|HTM interface and thus results in a higher open circuit voltage (V_{OC}) [134].

Substituting MA^+ by FA^+ shifts the absorption onset of the perovskite to a lower energy, thereby increasing the short circuit current density (J_{SC}) and the resulting PCE. Furthermore, the electron diffusion lengths of perovskites containing MA^+ versus FA^+ are very similar (130 nm for $MAPbI_3$ versus 177 nm for $FAPbI_3$), but the perovskites containing FA^+ have an increased hole diffusion length (90 nm for $MAPbI_3$ versus 813 nm for $FAPbI_3$) [56, 107].

As previously mentioned, the hydration of $MAPbI_3$ leads to the formation of the PbI_2 and MAI precursors, therefore the chemical stability of the perovskite increases

when MA^+ is replaced by FA^+. This is due to the robust structure of $FAPbI_3$ which is not greatly affected in the presence of water or by the inclusion of additional small molecules. With that said however, the black $FAPbI_3$ perovskite type polymorph undergoes a slow phase transformation to the yellow polymorph which is more thermodynamically stable at room temperature [46, 134]. The perovskite crystal structure is destabilised in this way, in the case of $FAPbI_3$ thus resulting in the need for the mixed MA^+ and FA^+ perovskites.

The performance of these mixed perovskite solar cells, is still dominated by $MAPbI_3$ rather than $FAPbI_3$. To further stabilise the perovskite structure in ambient conditions, the I^- anions are substituted by Br^-. As mentioned previously, this however shifts the absorption onset of the mixed perovskite to a higher energy, therefore only a fraction (15%) of the iodide is replaced by bromide [55, 86]. Furthermore, ion migration was measured for mixed perovskites. Under illumination, separate iodine and bromine rich domains were observed suggesting that perovskite thin films are in fact dynamic systems [135].

With the use of transient absorption spectroscopy (TAS), our aim was therefore to obtain a possible explanation for the high efficiencies achieved with this material from the ultrafast photoinduced charge dynamics. By learning the rate constants associated with the dominant charge transfer and recombination processes, perovskite materials can be further improved.

Steady state absorption spectrum

As is evident in the photograph of Figure 6.1, the mixed perovskite is dark brown and therefore absorbs the majority of the visible spectrum. This is confirmed by the steady state absorption spectrum presented in Figure 6.4. From the absorbance obtained corresponding to $\lambda = 388$ nm, a 0.4% transmission was calculated. This strong absorption suggests that we only photoexcite the front layer of the perovskite thin film. Due to the high electron and hole mobilities of perovskites, this should not affect the charge carrier dynamics, but to further correct for it, we employ very thin perovskite films in our study (approximately 200 nm).

Transient absorption spectroscopic measurements were carried out for various pump pulse photon energies: far from the optical band gap (3.2 eV, $\lambda = 388$ nm), at the optical band gap (1.6 eV, $\lambda = 775$ nm), as well as at 2.6 eV ($\lambda = 480$ nm). While the primary focus of the study was the charge dynamics immediately following 3.2 eV photoexcitation, the supporting results obtained from the lower energy pump measurements will also be presented in the chapter to follow.

Electronic properties

The electronic band structure has to date not yet been calculated for the mixed perovskite $(FAPbI_3)_{0.85}(MAPbBr_3)_{0.15}$, however it has been determined for the more commonly employed perovskite, $MAPbI_3$. An example electronic band structure calculated by Motta *et al.* for fully relaxed $MAPbI_3$, is presented in panel a of Figure 6.5 [136]. As is evident from the figure, there are many valance and conduction bands present in perovskite materials.

Like introduced in Chapter 2, the electronic band structure is qualitatively the same for most lead based perovskites. The lowest energy conduction band (CB) is deter-

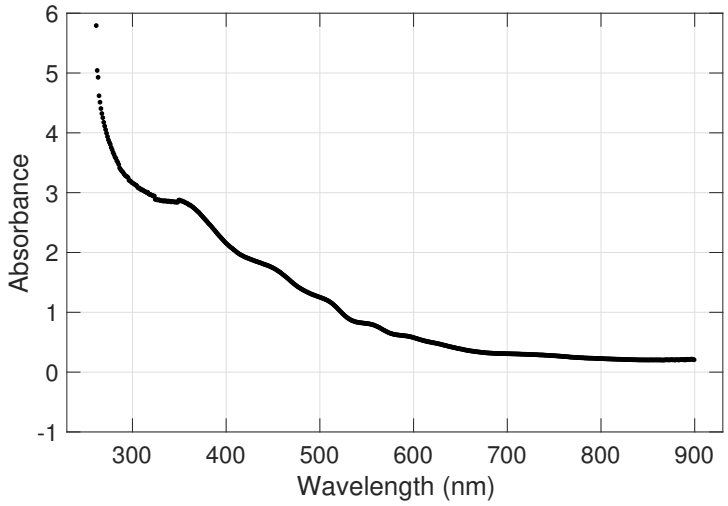

Figure 6.4: The steady state absorption of our 200 nm thick $(FAPbI_3)_{0.85}(MAPbBr_3)_{0.15}$ thin films. The measured UV-Vis absorbance is plotted as a function of wavelength. As expected from the dark brown colour of the sample, together with the absorption spectrum of $MAPbI_3$ presented in Chapter 2, the absorption of the mixed perovskite is spectrally broad.

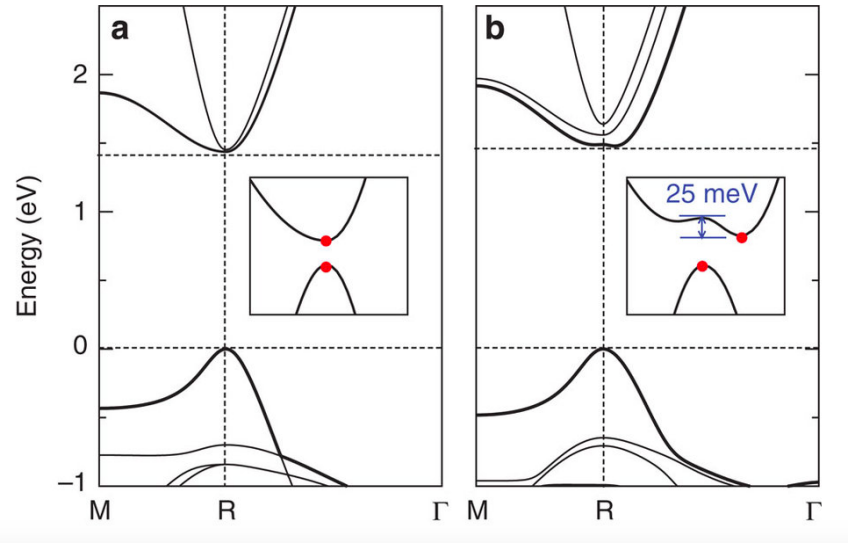

Figure 6.5: The calculated electronic band structure for a fully relaxed $MAPbI_3$ crystal for the MA^+ orientation along the (111) and (011) crystal axes shown in panels a and b respectively. The inserts show a magnification of the conduction band minimum and valence band maximum shifted in energy for ease of observation. The rotation of the organic cation along the (011) crystal axis, results in an indirect bandgap. The energy landscape of the organic cation is very shallow, thus resulting in a small energy difference between the two CB energy minima (approximately 20 meV). This figure was obtained from the work of Motta *et al.* [136].

mined by hybridisation of the 6p lead, 5p iodine and 4p bromine orbitals, but is dominated by the empty 6p lead orbitals. On the other hand, the electronic nature of the highest energy valence band (VB) is mostly determined by the orbital overlap of the 6s lead orbital, with the 5p iodine and 4p bromine orbitals, with a small contribution from the 6p lead orbitals [47, 73, 137].

Even though the organic cation should not influence the CB minimum and VB maximum because its molecular orbitals are energetically far from the band gap, it seems

that its spatial orientation within the inorganic framework does have an effect. In the case of $MAPbI_3$, for the orientation of MA^+ along the (111) crystal axis, the perovskite is a direct band gap semiconductor, while for its orientation along the (011) crystal axis, the band gap becomes indirect. This phenomena can be seen in panels a and b respectively of Figure 6.5, together with inserts of the zoomed in band gaps. The interaction between the organic cation and the lead iodide cage, whereby the MA^+ exerts strain on the PbI_6^{4+} octahedra, is driven by dispersive forces and thus alters the nature of the band gap. At room temperature, the spatial orientation of the organic molecule fluctuates, suggesting that the electronic structure of MAPI constantly varies between the diagrams of panels a and b. For this reason, perovskites can be referred to as dynamical band gap semiconductors [136].

With that said, we therefore expect that with mixed perovskites such as $FA_{0.85}MA_{0.15}PbI_{2.55}Br_{0.45}$ the degeneracy of states will be even further reduced in comparison to $MAPbI_3$ as the degrees of freedom in the electronic band structure calculation are increased by the introduction of the formamidinium cation and halide mixture. This would result in even more conduction and valance bands in the case of $FA_{0.85}MA_{0.15}PbI_{2.55}Br_{0.45}$. However, as the electronic character of the lowest conduction and highest valence band is dominated by the lead and halide constituents, the optical band gap of our mixed perovskite is very similar to that of $MAPbI_3$.

In addition to the dynamic nature of the band gap of perovskite materials, the samples which we investigated with TAS were microcrystalline thin films, therefore the area of our probe pulse focus covered many small crystals containing both MA^+ and FA^+ molecules orientated in many different directions. We therefore cannot differentiate between the two possible energy diagrams shown in Figure 6.5 but may rather probe a mixture of the two – more similar to the sketch shown in panel a, Figure 2.6, Chapter 2.

6.2 Fabricating perovskite thin films

The deposition of perovskite thin films from precursor solutions has been well studied, is simple and mostly reproducible. The three methods usually employed were introduced in Chapter 2 and include the: one step spin coating [51, 74, 75], two step sequential deposition [138], and vapour deposition (in a high vacuum chamber) [139] methods.

Our $FA_{0.85}MA_{0.15}PbI_{2.55}Br_{0.45}$ samples were made by our project collaborators in Giessen, Germany, by spin coating glass slides with a precursor solution in a nitrogen environment according to the anti-solvent assisted crystallisation spin coating approach [86]. Formammidinium iodide (FAI) and methylammonium bromide (MABr) were synthesised as described by Jeon *et al.* and Ruess *et al.* [86, 140].

A precursor solution was prepared in a 7:3 volume to volume ratio of γ-butyrolacetone/DMSO solvent by mixing the synthesised FAI and MABr with purchased PbI_2 and $PbBr_2$ in a ratio of 85:15:85:15, at 60 °C for 10 minutes. The resulting solution was then spin coated onto a clean glass substate which was rotated at 5000 rpm for 30 s, during which, 1 ml of toluene was added drop-wise. To evaporate the solvent, the substate was subsequently annealed at 100 °C for a further 10 minutes.

The resulting perovskite thin films were dark brown in colour and densely packed with crystal domains as can be seen in the scanning electron microscope (SEM) images

of Figure 6.6, measured by our project collaborators in Giessen, Germany. The mixture of γ-butyrolacetone to DMSO as the solvent in the deposition of these thin films is thought to be responsible for the uniform densely packed microcrystalline perovskite layers obtained [86]. The measured film thickness was 200 nm with an alpha-stepper (Alpha-Stepper 10-00020, Tencor Instruments). Although this is less than the optimal thickness for use in high PCE solar cell devices, the films were required to be synthesised less opaque to ensure transient absorption measurements could be performed in transmission with a reasonable sensitivity (approximately 10^{-3}). Due to the highly absorbent nature of the perovskite material, together with the microcrystallinity of the sample, these films are very light scattering, thus unfortunately reducing our measurement technique sensitivity.

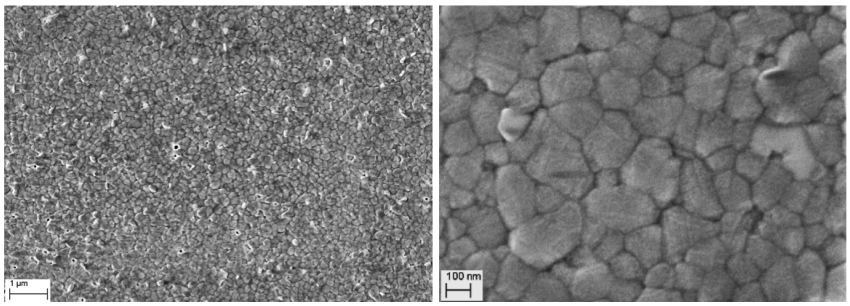

Figure 6.6: Two scanning electron microscope (SEM) images of our microcrystalline perovskite thin films. The image on the left has a 1 μm scale bar, and the zoom in on the right a 100 nm scale bar.

Determining the perovskite layer chemical composition

In addition to the SEM images, an x-ray diffraction (XRD) experiment was also performed on the perovskite thin film samples by our project collaborators in Giessen, Germany, see Figure 6.7. The peaks denoted with the α correspond to the desired so-called 'black perovskite phase' of our mixed perovskite, while the two peaks denoted with the δ correspond to the undesired yellow phase of $FAPbI_3$. By comparing our obtained α lattice parameters with the typical XRD patterns reported in literature [134, 141], we were able to determine that the chemical composition of our thin film samples was indeed $FA_{0.85}MA_{0.15}PbI_{2.55}Br_{0.45}$.

The two δ peaks in the XRD pattern, corresponding to the hexagonal phase of $FAPbI_3$, are indicative that $FAPbI_3$ is present as a separated phase in our thin film. This is expected for annealing times larger than 2 minutes and is indicative of the slight decomposition of the perovskite layer. This partial decomposition occurs mostly on the top surface of the perovskite layer and does not affect the charge dynamics in the bulk [141]. To make sure that we probe the charge dynamics of the black $FA_{0.85}MA_{0.15}PbI_{2.55}Br_{0.45}$ polymorph rather than the yellow $FAPbI_3$ polymorph, we pump and probe our samples from the the glass slide side (bottom surface of the perovskite).

Furthermore, in the current state of the art lead based perovskite solar cells containing a mixture of Rb^+, Cs^+, MA^+ and FA^+ and a mixture of I^- and Br^-, Saliba *et al.* managed to completely eliminate the undesired yellow phase for small Rb^+ and Cs^+ concentrations [59].

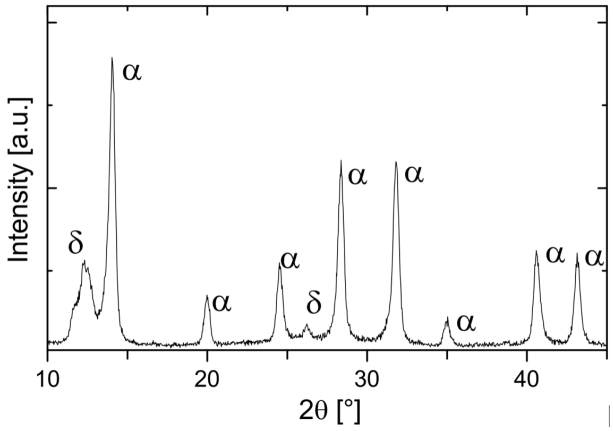

Figure 6.7: X-ray diffraction (XRD) pattern obtained for one of our $FA_{0.85}MA_{0.15}PbI_{2.55}Br_{0.45}$ thin films. The peaks corresponding to the desired black perovskite phase are denoted with a α, and the peaks corresponding to the undesired yellow phase of $FAPbI_3$ are denoted by δ. A negligible contribution from the 12.7° peak of PbI_2 observed as a small shoulder of the 11.5° δ phase peak of $FAPbI_3$.

Overlapping with the 11.5° δ phase peak of $FAPbI_3$, is a negligible contribution from the 12.7° peak of PbI_2 observed as a shoulder. The lack of a substantial PbI_2 peak is an indication that our perovskite thin film has not degraded. Furthermore, it usually is only present in films which were deposited with excess PbI_2 precursor.

Encapsulation

In order to reduce the degradation of the perovskite thin film due to the moisture in ambient air, the samples were sealed. This was done in two ways: either by spin coating of a thin film of poly(methyl methacrylate), more commonly referred to as PMMA, from an anisole based solution, or by sandwiching the perovskite layer between two glass slides and sealing the edges with a UV curable epoxy resin (Ossila E131 Encapsulation Epoxy). Please refer to Figure 6.8 for the chemical structures of PMMA and the epoxide functional group present in all epoxy resins.

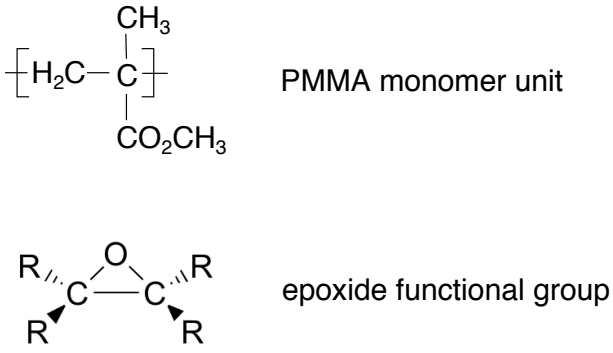

Figure 6.8: The chemical structure of the poly(methyl methacrylate), PMMA, monomer unit used for encapsulation of our perovskite layers is shown above. The chemical structure of the highly reactive epoxide functional group present in the epoxy resin is shown below.

To ensure that the encapsulation method did not have a direct effect on the charge dynamics or spectral features of the $FA_{0.85}MA_{0.15}PbI_{2.55}Br_{0.45}$ perovskite material, transient absorption measurements were carried out on a collection of samples: half of

which were sealed with PMMA, and the other half with glass and epoxy. These results, as well as the steady state absorption spectra of PMMA, epoxy and glass are presented in Chapter 7.

Varying the chemical composition

Furthermore, to identify the spectral characteristics and charge transfer processes unique to $FA_{0.85}MA_{0.15}PbI_{2.55}Br_{0.45}$, we performed a series of measurements on samples with various organic cation and halogen anion ratios. These thin film samples were prepared in an identical procedure to that described above, but simply changing the FAI, MABr, PbI_2 and $PbBr_2$ ratios in the precursor solution. Again, samples encapsulated with PMMA as well as perovskite thin films sandwiched between two glass slides and sealed with epoxy were studied. From the results we observed that the encapsulation method does not affect the spectral transient signatures of the materials, nor the associated temporal dynamics, but the different chemical composition does. Therefore the data presented in the chapter to follow was acquired from samples encapsulated with both PMMA and glass.

Perovskite thin films in contact to electron and hole transport materials

In order to investigate the electron and hole transfer processes which occur in perovskite solar cells, samples were prepared of $FA_{0.85}MA_{0.15}PbI_{2.55}Br_{0.45}$ contacted to [6,6]-phenyl-C61-butyric acid methyl ester (PCBM) as an electron transport material. Alternatively the perovskite thin films were contacted to the hole transport material poly(3,4-ethylenedioxythiophene)-poly(styrenesulfonate), more commonly referred to as PEDOT:PSS. Additionally, samples were also synthesised where $FA_{0.85}MA_{0.15}PbI_{2.55}Br_{0.45}$ was contacted to both PCBM and PEDOT:PSS. Please refer to Figure 6.9 for photographs of four example samples encapsulated between two glass slides and sealed with epoxy. The chemical structures of both PCBM and PEDOT:PSS are depicted in Figure 6.10.

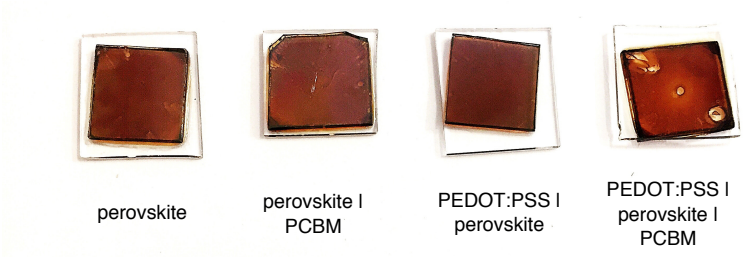

Figure 6.9: Photographs of four example samples encapsulated between two glass slides and sealed with epoxy. The first sample is a pristine $FA_{0.85}MA_{0.15}PbI_{2.55}Br_{0.45}$ perovskite layer, the second sample contains the mixed perovskite contacted to the electron transport material PCBM, the third sample contains the mixed perovskite contacted to the hole transport material PEDOT:PSS, and in the fourth sample the mixed perovskite is contacted to both PCBM and PEDOT:PSS. The chemical structures of PCBM and PEDOT:PSS are shown in Figure 6.10.

As we were only interested in the electron and hole dynamics within the perovskite material itself, these films were not completed with electrodes to fabricate fully operational solar cells which could be characterised spectroelectrochemically. Therefore their

power conversion efficiencies and I-V curves were not determined. Typical values attained by Jeon *et al.* for fully operational devices employing $FA_{0.85}MA_{0.15}PbI_{2.55}Br_{0.45}$ as the photoabsorber were: 22 $mAcm^{-2}$ for the short circuit current, open circuit voltage of 1.08 V and fill factors of approximately 0.73, leading to PCEs above 17% [55]. As a reminder, perovskite solar cells are fabricated in two main types of architectures: planar cells [139] or mesostructured cells [74].

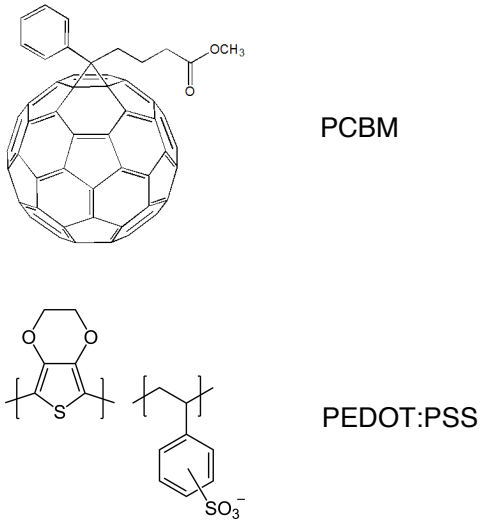

Figure 6.10: The chemical structure of the electron transport material [6,6]-phenyl-C61-butyric acid methyl ester (PCBM) is shown above, and chemical structures of the two monomer units of PEDOT and PSS are shown below, which form the hole transport material poly(3,4-ethylenedioxythiophene)-poly(styrenesulfonate), more commonly referred to as PEDOT:PSS.

6.3 Spectroscopy of perovskites

Perovskite materials have only been employed as photoabsorbers in solar cell devices in recent years. Therefore not many microscopic studies have been carried out, especially on the mixed crystals. Research has rather been driven by improving the PCEs and stabilities of these devices. As it is traditionally the most commonly employed perovskite, $MAPbI_3$ is also the most well studied, and some charge dynamics processes have already been investigated and reported on. These were summarised together with the spectroscopic measurements of mixed perovskites and expected spectroscopic signatures in Chapter 2. The recombination process which dominate in these materials will be explained in detail in the following chapter together with our analysis procedure.

In contrast, the charge dynamics processes and associated rates unique to $FA_{0.85}MA_{0.15}PbI_{2.55}Br_{0.45}$ are not well known and understood. Our aim is therefore to link the electronic band structure to the charge extraction and possible loss mechanisms already determined for perovskite materials. As will be shown in the chapter which follows, with the use of transient absorption spectroscopy we were able to follow the electronic excitation of $FA_{0.85}MA_{0.15}PbI_{2.55}Br_{0.45}$ in time and thus build a simplest possible consistent photoinduced charge dynamics model, as well as determine the dominating recombination mechanisms which occur in this material with associated rate

constants, as a function of pump laser pulse fluence. By comparing the rate constants associated to charge generation, transfer and recombination processes, with those already reported in literature for other perovskite materials, we could learn why this particular composition, is superior to others in terms of photovoltaic performance.

The final goal being that we would like to learn about the fundamental physics and chemistry processes which are responsible for making this mixed perovskite material such a good photoabasorber for use in photovoltaic devices. Hopefully, with our contribution, material scientists will be able to further improve perovskite solar cells.

7. Transient Absorption Spectroscopy of Perovskite Thin Films

We investigated the charge recombination dynamics in $FA_{0.85}MA_{0.15}PbI_{2.55}Br_{0.45}$ thin films which occur upon photoexcitation, in real time, with the use of transient absorption spectroscopy (TAS). The photovoltaic devices made with this mixed perovskite photoabsorbing material boasted record efficiencies at the time our study commenced, and still continue to be among the best. For more details with respect to the material preparation and its electrochemical properties refer to Chapter 6, and for an explanation of our experimental technique to Chapter 3.

In order to build a simplest possible and consistent charge dynamics model, we linked the temporal evolution of the visible and infrared spectral signatures to the allowed electronic transitions of the perovskite. In this way we observed the geminate, non-geminate and Auger recombination of excitons and free charges and determined their associated rate constants within a crystal domain of the $FA_{0.85}MA_{0.15}PbI_{2.55}Br_{0.45}$ thin film.

This chapter aims to show the charge dynamics model together with our TAS results and the detailed analysis procedure that lead us to that particular model. This is presented together with a recombination analysis based on varied pump pulse fluence, and additional supporting measurements. As in the presentation of the charge transfer processes determined for dye sensitised solar cells (Chapter 5), I will first show the charge dynamics model which has resulted from a fully consisted analysis of our broad band transient absorption spectra, and then provide the detailed justification from the individual data sets. We believe that this order of presentation makes it easier to follow the reasoning rather than building up to a big picture from many individual results.

7.1 Charge dynamics model

Figure 7.1 is a rough schematic representation of the lowest conduction band (CB1) and highest valence band (VB2) in $FA_{0.85}MA_{0.15}PbI_{2.55}Br_{0.45}$ which take part in the photogeneration of charges, as a function of the k vector. The bandgap of the perovskite is shown in the figure as the energy separation between the CB and the VB at the R-point. The photoexcited electrons are depicted in red and blue representing hot and cooled electrons respectively, and the photoexcited holes in grey.

As the energy band diagram has not yet been calculated for this particular perovskite chemical composition, the sketch is a combination of the band diagram schematic and the calculated band structures for $MAPbI_3$ presented in Figures 2.6 and 6.5 respectively. The energy separation between the depicted conduction and valence bands is drawn to scale, as determined by the energies of the various spectroscopic signatures.

However, the curvature of the bands with respect to the k vector is exaggerated to allow for a better outlook of the multiple charge dynamics processes in the schematic.

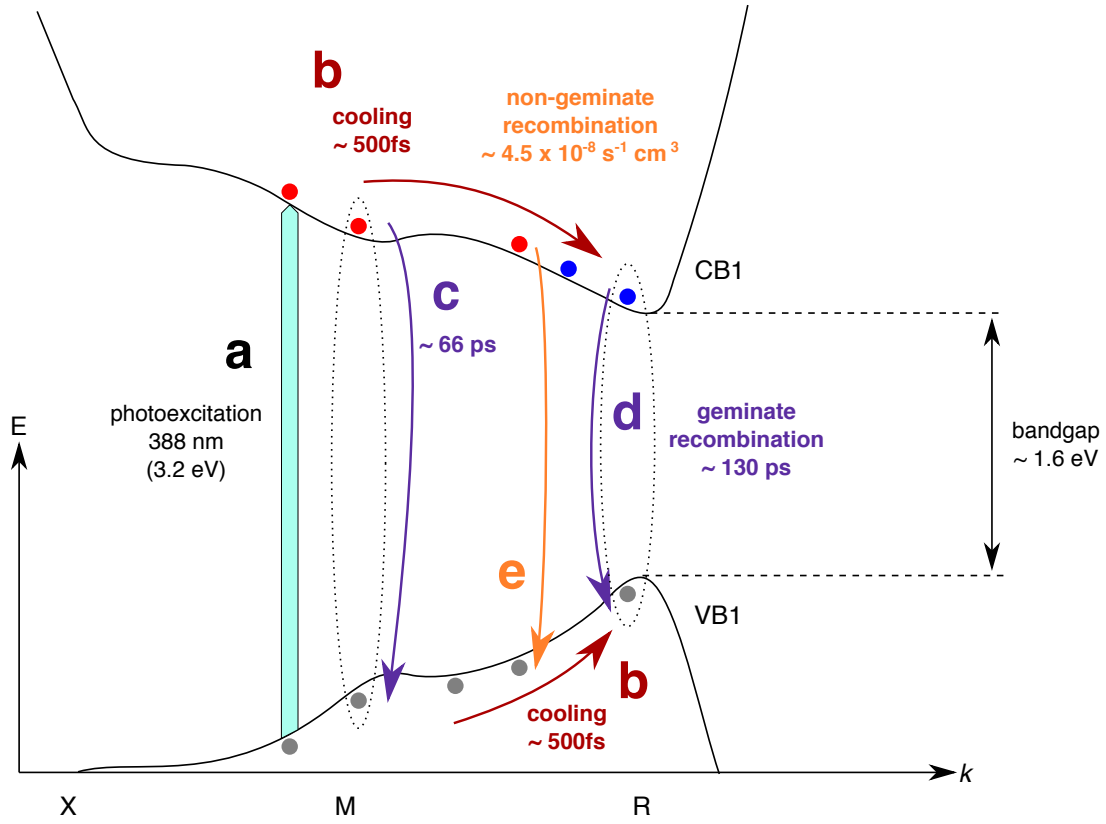

Figure 7.1: A simple energy level diagram of the lowest conduction band (CB1) and highest valence band (VB1) in $FA_{0.85}MA_{0.15}PbI_{2.55}Br_{0.45}$ as a function of the k vector, together with an indication of the bandgap energy. The sketch is a combination of the band diagram schematic and the calculated band structures for $MAPbI_3$ presented in Figures 2.6 and 6.5 respectively. The energy separation between the depicted conduction and valence bands is drawn to scale but the curvature of the bands with respect to the k vector is rough. Hot and cold electrons are drawn as red and blue circles respectively, while holes are drawn in grey. The charge dynamics processes and their associated time and rate constants, which occur upon photoexcitation with a 3.2 eV laser pulse (**process a**) are as follows: charge carrier cooling towards the CB minimum and VB maximum (**process b: 500 fs**), geminate recombination at the M-point (**process c: 66 ps**), geminate recombination at the R-point (**process d: 130 ps**), and non-geminate recombination independent of the k vector (**process e: 4.5** $\times$ $\mathbf{10^{-8}}$ $\mathbf{s^{-1}cm^3}$).

Upon non-resonant photoexcitation with a femtosecond laser pulse of 3.2 eV photon energy ($\lambda = 388$ nm), electrons are excited out of the highest valence band (VB1), into the lowest energy conduction band (CB1), approximately at the M-point, Figure 7.1, process a. Within the temporal resolution of our measurement technique (< 200 fs) the photoexcited hot electron distribution in the CB, initially thermalises through electron-electron scattering. This process is described in more detail in the subsection below. Following the initial ultrafast thermalisation the hot electrons and holes cool towards the CB minimum and VB maximum with an associated time constant of approximately 500 fs, process b.

In addition, geminate and non-geminate recombination channels are present following the non-resonant photoexcitation of $FA_{0.85}MA_{0.15}PbI_{2.55}Br_{0.45}$ assigned to excitons and free charge carriers respectively. Away from the R-point, excitons recombine with an associated time constant of 66 ± 5 ps corresponding to a rate constant

of 1.5×10^{10} s^{-1}. Conversely, at the R-point this process is slowed and can be characterised by a time constant of 130 ± 15 ps (7.7×10^{9} s^{-1}), refer to Figure 7.1, processes c and d.

On the other hand, due to a high peak charge carrier density immediately following photoexcitation of approximately 1.5×10^{19} cm^{-3} in these experiments, nonlinear recombination processes cannot be neglected. The non-geminate recombination requiring two free charge carriers begins to dominate at charge carrier densities in excess of $10^{17} - 10^{18}$ cm^{-3} [70]. It occurs in the $FA_{0.85}MA_{0.15}PbI_{2.55}Br_{0.45}$ thin film with the same rate per charge carrier density (4.5×10^{-8} $s^{-1}cm^{3}$) irrespective of the associated k vector (Figure 7.1, processes e).

Furthermore, the three charge carrier Auger recombination process becomes dominant at higher charge carrier densities. It was already reported for peak charge carrier densities of $10^{18} - 10^{19}$ cm^{-3} in other perovskite materials [64, 98, 142], and is therefore included in our analysis for higher pump fluences.

As previously introduced, there is currently no agreed upon description of the initial photoprocesses occurring within various perovskite absorbers upon high energy non-resonant photoexcitation. Interpretations include the possibility of multiple conduction and valance bands taking part in charge generation, the presence of a charge transfer state, as well as the more widely accepted idea that charge dynamics occur along the k vector.

Moreover, transient absorption spectroscopy is an experimental method which monitors the population and depopulation dynamics of electronic states upon photoexcitation, with associated spectroscopic signatures in the probed spectral region. Therefore, with the use of this method, we are unable to differentiate the electronic nature of the probed states. In other words, to conclude whether a spectroscopic signature is associated with the population of a conduction or valence band, or rather a charge transfer state, or determine its associated k vector.

To further complicate our analysis, all information pertaining to the sign of the charge of the absorbing species is also indefinite, thus causing us the inability to differentiate between an electron or a hole population as the probed species. In order to explain our TAS experimental findings, we were required to fit our data to the simplest fully consistent model possible. In reality however this may not be the entire picture but only a portion thereof. While the concept and processes can be interpreted as a general model for perovskite materials, the determined rate constants are rather characteristic of the $FA_{0.85}MA_{0.15}PbI_{2.55}Br_{0.45}$ thin films which we measured.

Charge carrier cooling

As mentioned above, upon non-resonant 3.2 eV ($\lambda = 388$ nm) photoexcitation, electrons are excited out of the VB into the CB, away from the R-point. The energy and momentum distributions of these hot electrons and holes are determined by product of the spectral content of the pump laser pulse and the density of states [136, 137] in both the conduction and valence bands. No significant population of electrons is believed to be excited out of the valence band at the R-point as a resonant conduction band is not known to be present.

The initial thermalisation of the hot electron distribution in the CB occurs within the temporal resolution of our TAS setup, and is governed by electron-electron scattering. Following this, the associated distribution function of these charge carriers is greater

than the lattice temperature, therefore the thermalised electrons are still referred to as hot. Their subsequent cooling to the CB band edge takes place through coupling with the crystal lattice, and is dominated by the coupling of electrons to longitudinal optical (LO) phonons, as previously observed for classic semiconductors. With the use of our TAS measurements, we observed the aforementioned charge carrier cooling, and in agreement with literature assign a time constant of approximately 500 fs to it [143].

As a result of state filling effects caused by Fermi level filling, a non-equilibrium electron distribution is presumed to be present in the conduction band at early times following photoexcitation (giving rise to the Burstein-Moss shift) [109]. Furthermore, a local minimum may arise in the lowest energy conduction band between the R- and M-points due to the aforementioned rotation of the organic cations (Figure 6.5), and as can be observed in the sketch of Figure 2.6. For these two reasons the initial cooling of hot electrons and holes to the conduction band minimum and valence band maximum respectively, does not occur completely within the first few picoseconds following photoexcitation. Slower recombination processes away from the R-point, such as the geminate and non-geminate recombination channels outlined above, can therefore contribute.

The experimental results presented in the sections to follow, aim to prove the photoinduced charge recombination model presented above as well as add valuable information pertaining specifically to $FA_{0.85}MA_{0.15}PbI_{2.55}Br_{0.45}$ in terms of spectral absorption features as well as recombination rate constants.

Excitons versus free charge carriers

Due to the low exciton binding energy and the high mobility of electrons and holes in perovskite materials, particularly $MAPbI_3$, free charge carriers are believed to be generated shortly following photoexcitation at room temperature. With that said, there is a huge spread in exciton binding energies determined for $MAPbI_3$ alone, ranging from 2 meV to above 60 meV. Therefore we must consider the presence of excitons on our ultrafast TAS measurement timescale.

It has been shown that the excitonic nature of perovskites increases substantially when the I^- content is decreased and the Br^- content is increased in these mixed halide materials. This is directly observed in the increase in exciton binding energies from as low as 25 meV for $MAPbI_3$ to approximately 64 meV for $MAPbBr_3$. Furthermore when charge carrier densities exceeding 10^{18} are present, which is often the case in these laser experiments, the fraction of excitons present in perovskites far outweighs the amount of free charge carriers [49, 144].

Therefore the model outlined above describes the geminate and non-geminate recombination dynamics of excitons and free charges respectively, upon photoexcitation of $FA_{0.85}MA_{0.15}PbI_{2.55}Br_{0.45}$ with a femtosecond laser pulse.

7.2 Detailed analysis

Even though our analysis procedure was described in detail in Chapters 3 and 5, for the sake of completeness, I'll introduce it once more in the case of perovskite thin films.

Transient absorption spectra were first acquired for $FA_{0.85}MA_{0.15}PbI_{2.55}Br_{0.45}$ thin films in the visible and infrared spectral regions, spanning from 450 nm to 1100 nm

with the use of white light continua probe pulses. A multitude of temporal lineouts covering the entire probed spectral region were obtained and analysed as a complete system. The known observed spectral signatures were then assigned to the corresponding electronic transitions in the sample. The unknown spectral signatures were in turn assigned to allowed electronic transitions in the sample by comparing their temporal evolutions with the energy band diagram of the perovskite. Our goal was, as always, to build the simplest and fully consistent model describing the photoinduced charge dynamics in our samples. We achieved this through combining the temporal traces and their associated spectroscopic signatures with the allowed electronic transitions of the perovskite.

The following subsections will give a detailed explanation of the recombination dynamics which take place in perovskite materials together with our applied analysis technique and interpretation thought process.

Recombination dynamics

Following the optical photoexcitation of a pristine perovskite thin film, the material relaxes back into its ground state through the radiative and non-radiative recombination of excitons and free electrons and holes. Perovskites are generally characterised by very intense photoluminescence signals thus indicating strong radiative recombination channels [69]. With respect to the optimisation of these hybrid lead halide photoabsorbers in photovoltaic devices, recombination channels (especially non-radiative mechanisms), are considered counter processes and must therefore be minimised through chemical tuning of the perovskite material and its crystal structure.

The nonlinear differential rate equation

In contrast to the charge transfer and recombination dynamics studied for dye sensitised solar cells which do not depend on charge carrier density ($n(t)$) and therefore on pump laser pulse fluence, presented in Chapter 5, the recombination processes characteristic to perovskite materials are sensitive to fluence. Therefore the recombination dynamics can no longer be described by a simple rate equation linear in n with an associated exponential fit function as a solution to $\frac{dn}{dt} = An$, but must be interpreted with the use of the solution to a differential rate equation.

$$\frac{dn}{dt} = An + Bn^2 + Cn^3 \tag{7.1}$$

The possible recombination channels

The differential rate equation presented in Equation 7.1 has been determined to model the recombination dynamics occurring in perovskite materials as described with the help of Figure 7.2 [70].

A is a rate constant in units of s^{-1} and represents the **monomolecular recombination** in the material as it only requires one charged particle to take place. A more accurate term for it would probably be 'mono-charge' recombination rate constant. This however sounds clumsy and by convention the word molecular is typically used (for the two and three charge carrier processes also). As can be seen in Figure 7.2 this term includes the usually radiative geminate recombination of excitons at very short times

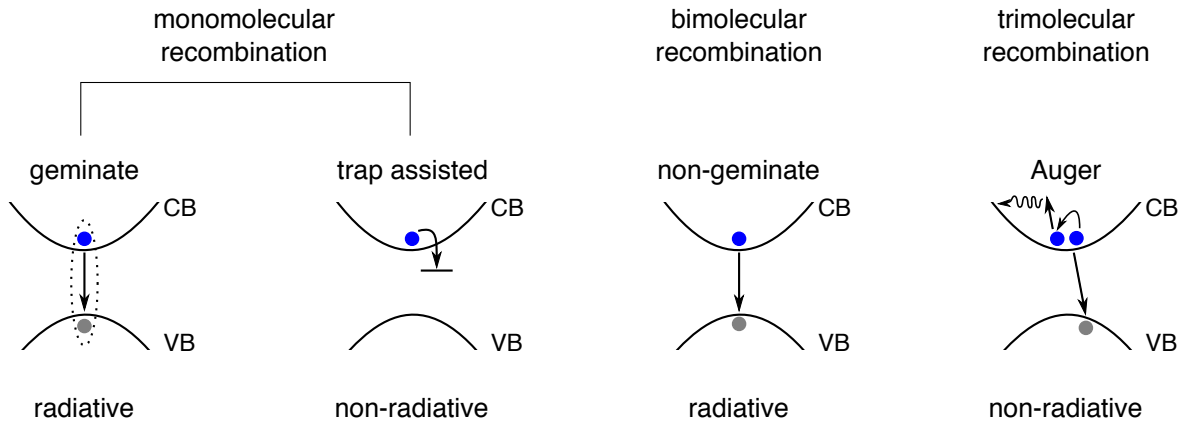

Figure 7.2: The possible recombination channels which occur in perovskite materials are shown with small sketches. Electrons are depicted in blue and holes in grey. The dynamics can be separated into three categories according to how many charged particles they require. Monomolecular recombination requires one charged particle and includes: the radiative geminate recombination of excitons and the non-radiative trap assisted recombination of electrons or holes (only the electron trapping is shown in the sketch). Bimolecular recombination requires two charged particles and refers to the radiative non-geminate recombination of free electrons in the conduction band (CB) and holes in the valence band (VB). Trimolecular recombination requires three charged particles and refers to the phonon-assisted Auger recombination of two photoexcited electrons in the CB and one hole in the VB, or two photoexcited holes in the VB and one electron in the CB (only the two electron - one hole Auger process is shown in the sketch).

following photoexcitation, as well as the non-radiative trap assisted recombination, which takes place on a nanosecond to microsecond timescale [85, 145, 146]. The geminate recombination of excitons was found to take place on the picosecond timescale [147, 148].

In particular, for perovskites containing a mixture of ions, the monomolecular trap assisted recombination channel was found to be strongly correlated to the crystal morphology [56]. Furthermore, this recombination pathway dominates at low charge carrier densities below 10^{17} cm^{-3}. As the typical charge carrier densities for perovskite solar cells under AM1.5 illumination are in the order of $10^{15} - 10^{16}$ cm^{-3} the goal of many studies has been to decrease the trap states available [146, 149–153]. Typical values for the trap assisted recombination rate are in the order of $10^{6} - 10^{9}$ s^{-1} [146].

B is a second order rate constant describing ultrafast dynamics, measured per density of charge carriers in units of $s^{-1}cm^3$ and it is characteristic of the radiative **bimolecular recombination** (non-geminate) in the perovskite. From photoluminescence measurements of perovskite thin films it was determined that the radiation which occurs at room temperature is governed by the non-geminate recombination of free charge carriers [154]. Typical values for the non-geminate recombination rate per charge carrier density are in the range of $6 \times 10^{-11} - 20 \times 10^{-10}$ $s^{-1}cm^3$ [70, 109, 113, 144–146, 154–158]. Lower bimolecular recombination rates are not uncommon, and they are thought to be caused by the localisation of the free electron and hole at different points in the unit cell [47].

Finally **C** is the **trimolecular recombination** rate constant, requiring three charged particles, measured per density of charge carriers squared, and is presented in units of $s^{-1}cm^6$. It describes the hot electron assisted non-radiative Auger recombination which can take place in the perovskite in the femtosecond regime. Typical values for the Auger recombination rate per charge carrier density squared are in the range of

$2 \times 10^{-29} - 10 \times 10^{-28}$ $s^{-1}cm^6$ for mixed halide perovskites, however they are expected to increase as the bromide content is increased [56, 70, 113, 145, 146, 155, 158].

These C values are highly dependent on the perovskite crystal structure so they are linked to the electronic and vibronic structure of the material and change with temperature as the structural phase of the perovskite also changes [155]. Therefore we can already expect that the organic cation ratio in our material will influence the obtained C values. Furthermore, Auger recombination was found to contribute to more than half of the total recombination in mixed halide perovskites. These materials must therefore be further developed to minimise the non-radiative recombination, especially in the high charge carrier regime [47].

As will be shown later in the work, the geminate and non-geminate recombination rates are characteristic of the material in question and therefore constants for a fixed crystal domain of $FA_{0.85}MA_{0.15}PbI_{2.55}Br_{0.45}$. Auger recombination, on the other hand, is much more sensitive to the crystal structure and thus the temperature and may not remain constant due to the dynamic nature of perovskite materials explained in the previous chapter.

The solution to the nonlinear differential rate equation

The aforementioned differential equation (Equation 7.1) does not have an analytic solution, however assuming that the third order contribution is small (especially true at low charge carrier densities) it can be solved to second order, see Equation 7.2.

$$n(t) = \frac{An_0}{(A + Bn_0)e^{(At)} - Bn_0} \tag{7.2}$$

We then added the Auger contribution as a perturbation to complete the solution as shown in Equation 7.3.

$$\begin{aligned} n(t) = & \frac{An_0}{(A + Bn_0)e^{(At)} - Bn_0} \\ & - \frac{A^2 n_0^3 C(Bn_0 - Bn_0 e^{(At)} + (A + Bn_0)e^{(At)} \log(\frac{A+Bn_0-Bn_0e^{(-At)}}{A}))}{B^2 n_0^2 (Ae^{(At)} + Bn_0(e^{(At)}))^2} \end{aligned} \tag{7.3}$$

n_0 is the initial charge carrier density. Although the generation of charge carriers is also governed by a generation rate equation, n_0 is taken as constant on our timescale as the pump laser pulse duration is considerably smaller than the timescale on which the recombination dynamics occur.

In contrast to the linear recombination rate equation employed for DSSCs where a time constant can be extracted from an exponential fit function without the knowledge of the charge carrier density $n(t)$, the nonlinear recombination rates B and C can only be converted to time constants if we know the charge carrier density in absolute numbers.

Obtaining a fit function

Even though our experimental technique monitors the photoinduced change in charge population of electronic states, we obtain a measure of change in optical density (absorbance) as a function of time, $\Delta OD(t)$, and not an absolute number with respect to

charge carrier density. As the pump laser pulse fluence is varied, a direct response is seen in the amplitude of the change in optical density for a given spectroscopic signature. We thus relate the two linearly as $\alpha n = \Delta OD$ where α is a proportionality constant correlating the charge carrier density (n) to the amplitude of the absorbance signal measured.

Additionally, not each incident photon is absorbed by the perovskite to generate an electron-hole pair, therefore the charge carrier density can also be related to the incident photon flux (ϕ) as $\phi = \beta n$ where β is a proportionality constant describing the photon to charge carrier conversion efficiency and is smaller than 1. As shown in the previous chapter, the $FA_{0.85}MA_{0.15}PbI_{2.55}Br_{0.45}$ thin films absorb 99.6% of the incident photons centred about $\lambda = 388$ nm. Therefore, in order to simply the fitting procedure and interpretation thereof, β will be set to 1 in the sections to follow.

Furthermore, the initial charge carrier concentration (n_0) was calculated as per Equation 7.4 below for a 388 nm laser pulse with associated pulse energy of 50 nJ. $E_{\text{laser pulse}}$ is the laser pulse energy in Joules, E_{photon} is the incident photon energy in Joules, d is the perovskite film thickness in cm, and A is the laser pump pulse focus area in cm^2.

$$\begin{aligned} n_0 &= \frac{E_{\text{laser pulse}}}{E_{\text{photon}} \times d \times A} \\ &= \frac{50 \times 10^{-9}\text{J}}{5.127 \times 10^{-19}\text{J} \times 200 \times 10^{-7}\text{cm} \times \pi \times 10^{-4}\text{cm}^2} \\ &= 1.55 \times 10^{19}\text{cm}^{-3} \end{aligned} \tag{7.4}$$

As we always aim to create the simplest fully consistent charge dynamics model, and as mentioned above, Auger recombination only begins to dominate at our initial charge carrier density, we first exclude it from our analysis procedure and only add it once we investigate higher charge carrier densities and our fitting procedure begins to require additional parameters. The validity of this assumption is directly tested by the success of the fitting procedure. If Equation 7.2 can be used to fit our data well, this is an indication that the Auger recombination channel doesn't dominate in the $FA_{0.85}MA_{0.15}PbI_{2.55}Br_{0.45}$ thin films at this charge carrier density.

Furthermore, as the trap assisted recombination occurs on a larger timescale than our measurement window, we incorporate it as a constant baseline y_0. In this way, the obtained A value is solely a measure of the geminate recombination rate.

With that said, before Equation 7.2 can be directly employed as a fit function for the temporal evolution of the spectroscopic signatures, the proportionality constant relating the maximum amplitude of the spectroscopic signal to the initial charge carrier density must be inserted (α), as well as the above calculated n_0 value to yield Equation 7.5.

$$\Delta OD(t) = \frac{\alpha A n_0}{A e^{(At)} - B n_0 + B n_0 e^{(At)}} + y_0 \tag{7.5}$$

This equation was used as the fit function in the analysis procedure, depicted in the subsections to follow, to obtain the geminate (A) and non-geminate (B) recombination rate constants from various spectroscopic signatures, in units of s^{-1} and $s^{-1}cm^3$ respectively.

The transient absorption spectrum

The transient absorption spectrum presented in Figure 7.3 was obtained from measurements on a $FA_{0.85}MA_{0.15}PbI_{2.55}Br_{0.45}$ thin film, as outlined in detail in Chapter 3. It comprises of three separate transient absorption spectra, acquired in different spectral regions with the use of two visible and one near infrared white light continua probe pulses. In general, some of the spectral signatures present in the figure have been observed and investigated for other perovskite compositions previously, however they are not yet well understood. Additionally, as far as we are aware, prior to this work, the fine spectral structure of the visible absorption signal, characteristic of $FA_{0.85}MA_{0.15}PbI_{2.55}Br_{0.45}$, has not yet been identified and studied.

As in the preceding chapters, the change in optical density is plotted using a colourmap as a function of time on two separate scales and probed wavelength. The energies associated to the respective wavelengths are also plotted on the right hand side of the transient absorption spectrum.

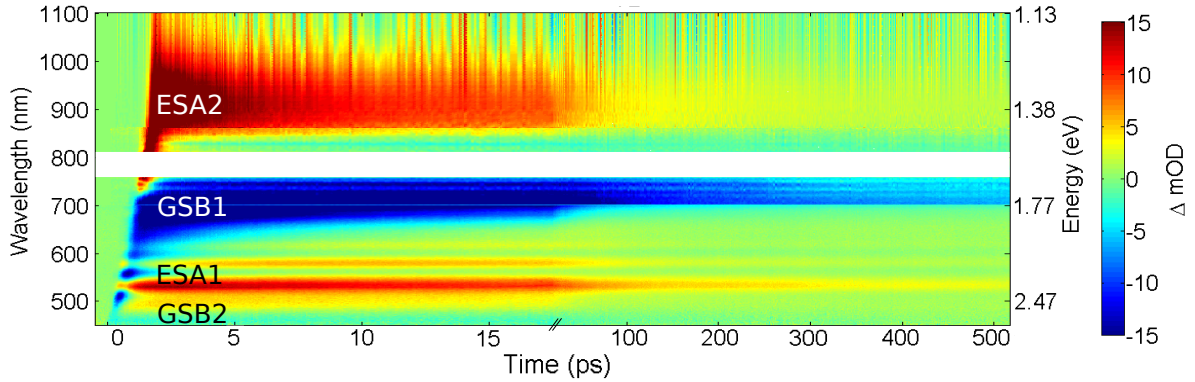

Figure 7.3: Transient absorption spectrum of a $FA_{0.85}MA_{0.15}PbI_{2.55}Br_{0.45}$ thin film comprising of three separate measurements, acquired in different spectral regions with the use of two visible and one near infrared white light continua probe pulses. The change in optical density (ΔOD) is plotted using a colourmap as a function of time (on two separate scales) and probed wavelength (left axis) and energy (right axis): red indicates an increase in absorption and blue a decrease in absorption upon photoexcitation. The spectral signatures are labeled in the figure and correspond to the: infrared excited state absorption at the M-point (ESA2), optical bandgap ground state bleaching at the R-point (GSB1), three-band visible excited state absorption at the R-point (ESA1), higher energy ground state bleaching at the M-point (GSB2).

As with previously reported transient spectra, two bleached electronic transitions are present – one corresponding to the optical bandgap (1.6 eV, $\lambda = 775$ nm), and the second at the higher resonant energy of approximately 2.6 eV, $\lambda = 480$ nm. The two signals appear as negative change in optical density signatures in the transient spectrum and are generated by the photoinduced depletion of the ground state, therefore they are commonly referred to as ground state bleaching signals (GSB). The origin of the ground state bleaching signal at the optical bandgap of the perovskite (GSB1) is usually assigned to the R-point change in population and thus depends on the population of both the conduction and valence bad edges. The origin of the higher energy bleaching signal (GSB2) continues to be a discussion point in the context of perovskite solar cells but is widely accepted to correspond to the electronic transition at the M-point.

In addition to the two bleaching signals, two positive change in optical density signatures are also present in the TAS spectrum of Figure 7.3. As they are an indication

of newly populated states upon photoexcitation, they are referred to as excited state absorption signals and denoted by ESA1 and ESA2 in the visible and near infrared spectral regions respectively.

Furthermore the spectral shape of ESA1, containing the three distinct bands, is unique to the $FA_{0.85}MA_{0.15}PbI_{2.55}Br_{0.45}$ perovskite, and was not observed for other perovskite compositions, where a very broad ESA1 absorption has been reported and also observed by us. The three absorption bands forming the ESA1 signal are centred about 2.1 eV ($\lambda = 580$ nm), 2.3 eV ($\lambda = 535$ nm) and 2.5 eV ($\lambda = 500$ nm) and are characterised by an identical temporal evolution, thus indicating that they probe the photoinduced population and depopulation of a single electronic state – as will become evident in the following analysis, this is the conduction band minimum.

As an additional check the aforementioned strong ground state bleaching signal of PbI_2 is not observed in the visible spectral region of Figure 7.3, therefore indicating that the sample has not degraded back into its precursors.

Temporal traces

In order to interpret the correlations between the population an depopulation dynamics of different electronic states from their spectroscopic signatures, we extract horizontal lineouts of change in optical density as a function of time ($\Delta OD(t)$) across the entire probed spectral region. These traces are typically averaged over a spectral range of 20 nm, and we analyse their temporal evolutions mathematically. A selection of four representative temporal traces corresponding to the four spectroscopic signatures seen above, and their mathematical fits according to Equation 7.5 are presented in Figure 7.4 for two separate time scales: a short time window on the left (early times following photoexcitation) and a long time window on the right.

Short time following photoexcitation

Let's first examine the early time measurements. The photoinduced generation of hot electrons and holes (within the pump pulse duration of 50 fs) in the conduction and valence bands around the M-point results in the instantaneous appearance of the **GSB2** bleaching signal centred about 2.6 eV, $\lambda = 480$ nm, during the duration of the pump laser pulse. This can be observed as a sharp rise in the negative change in optical density at time zero as seen in the example temporal trace presented in Figure 7.4, section d. At early times, dominating the first 5 ps, an ultrafast monoexponential decay describes the data with an associated time constant < 500 fs.

Conversely, the generation of the ground state bleaching signal **GSB1** (centred at 1.6 eV, $\lambda = 775$ nm) corresponding to the optical bandgap does not occur instantaneously upon photoexcitation, but rather grows in with a characteristic time of < 500 fs (section b). Furthermore, by studying the transient absorption spectrum shown in Figure 7.3 we note that although the signal is initially spectrally broad reaching out to 500 nm, it narrows temporally.

In addition to the two bleaching signals presented above, two excited state absorption signals are also present in the transient spectrum of Figure 7.3. As previously introduced, the visible signal (**ESA1**) is made up of three narrow absorption bands centred about 2.1 eV ($\lambda = 580$ nm), 2.3 eV ($\lambda = 535$ nm) and 2.5 eV ($\lambda = 500$ nm) with identical temporal evolutions. For this reason, a temporal lineout extracted from one of three

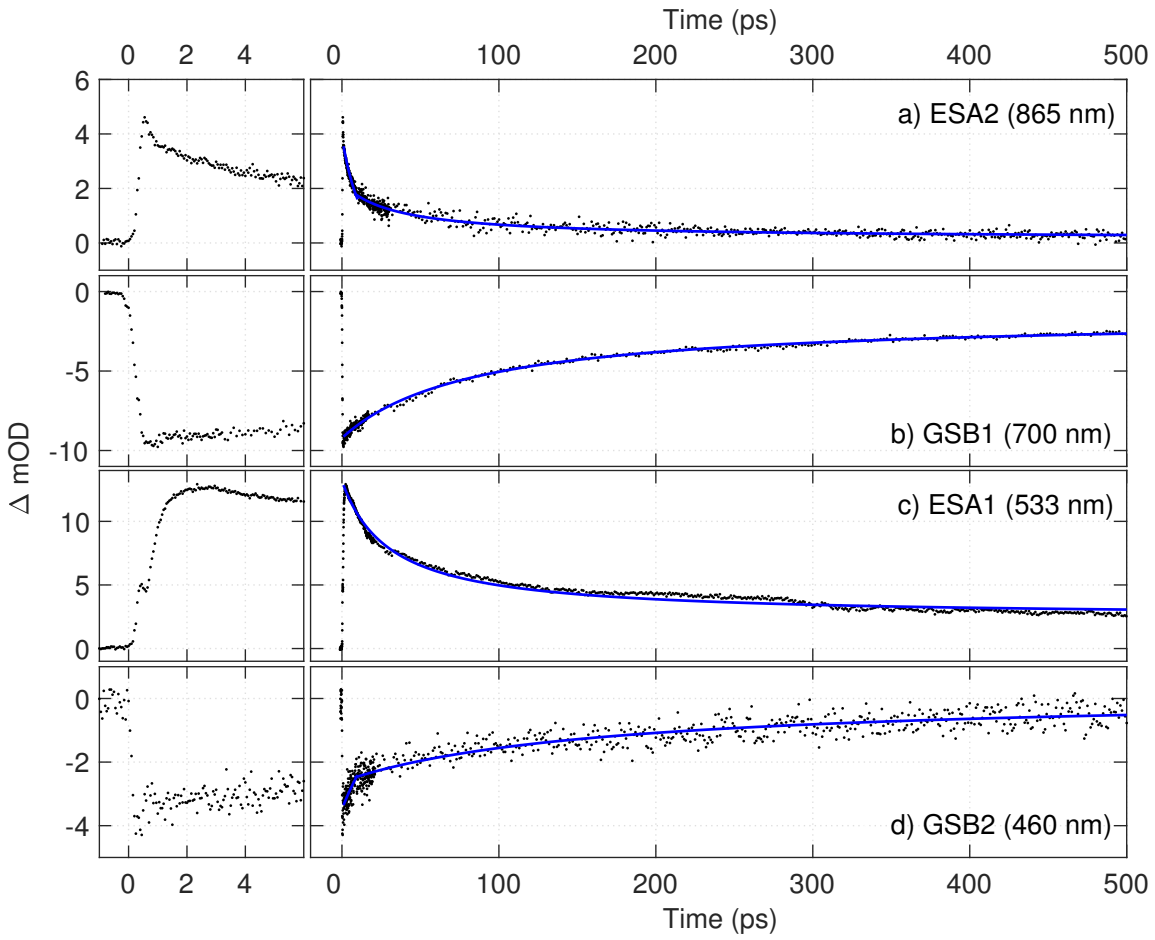

Figure 7.4: Four example temporal traces of change in optical density as a function of time ($\Delta OD(t)$) corresponding to the spectroscopic signals of Figure 7.3 are shown for short (left) and long times (right) following photoexcitation. Trace a) corresponds to the infrared excited state absorption (ESA2) signal and was obtained at a central wavelength of 865 nm. Trace b) corresponds to the bandgap ground state bleaching (GSB1) signal and was obtained at a central wavelength of 700 nm. Trace c) corresponds to one of the three bands making up the conduction band minimum excited state absorption (ESA1) signal and was obtained at a central wavelength of 533 nm. Trace d) corresponds to the high energy ground state bleaching signal (GSB2) and was obtained at a central wavelength of 460 nm. The data is shown with black markers, and the fitting functions are shown in blue for the long time traces.

bands was selected to serve as an example in Figure 7.4, section c. Furthermore, the three bands are not generated within the duration of the pump laser pulse, but rather grow in with a time constant < 500 fs, similar to that of GSB1.

In contrast to the unique spectral shape of ESA1, the **ESA2** signal is characterised by a broad absorption in the near infrared spectral region. It is generated immediately upon excitation as can be seen in the instantaneous rise of the example temporal trace shown in Figure 7.4, section a. Similar to the behaviour of GSB2 at early times, an ultrafast monoexponential decay with a characteristic time constant < 500 fs dominates.

By combining these dynamics, we are therefore able to pair ESA1 and GSB1 and assign the visible excited state absorption signal to the conduction band minimum, see Figure 7.5. Furthermore, as ESA2 and GSB2 behave the same way, we can conclude that they probe the same population and thus assign the infrared excited state absorption signal away from the conduction band minimum, at the M-point. Interestingly, the energy separation between the heavy electron (HE) CB2 and CB1 close to the M-point,

matches the energy at which the ESA2 signal is observed. We therefore assign ESA2 to the CB1 – CB2 (HE) electronic transition. On the other hand, not enough is known with respect to the higher energy conduction bands terminating the three electronic transitions which give rise to ESA1. They are thus drawn in as horizontal dashed lines.

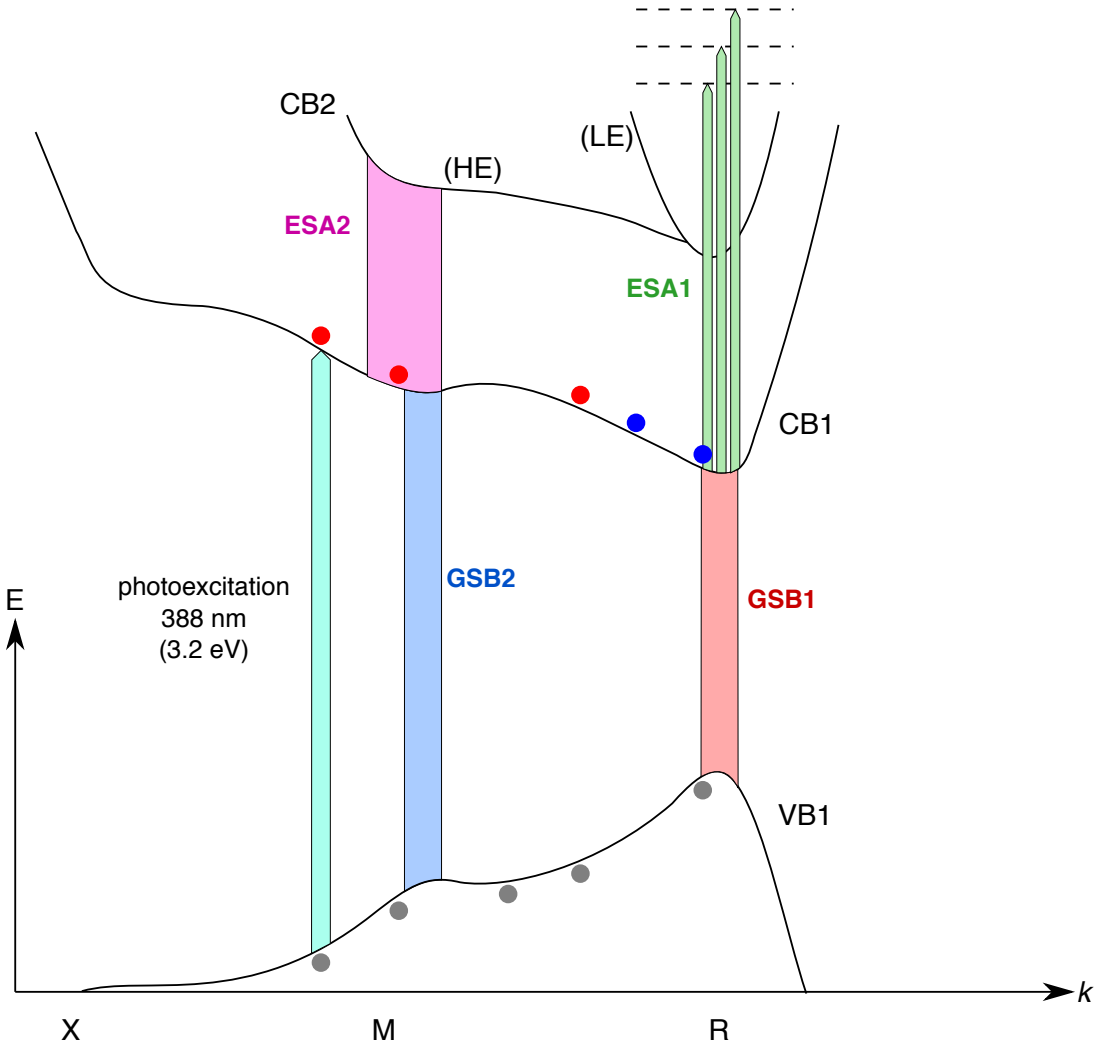

Figure 7.5: A simple energy level diagram of the two lowest conduction bands (CB1 and CB2) and highest valence band (VB2) in $FA_{0.85}MA_{0.15}PbI_{2.55}Br_{0.45}$ drawn as a function of the k vector. Both the heavy (HE) and light (LE) electron portions of CB2 are depicted. Hot and cold electrons are shown in red and blue respectively, while holes are grey. The transient absorption spectroscopic signatures in the visible and infrared spectral regions generated upon photoexcitation with a 3.2 eV laser pulse are shown with respect to allowed electronic transitions in the mixed perovskite thin film. The optical bandgap bleaching signal **GSB1** (red) corresponds to the VB1 - CB1 transition at the R-point, while the higher energy bleaching **GSB2** (blue) corresponds to the VB1 - CB1 transition near to the M-point. The three-band **ESA1** (green) corresponds to the R-point transition between CB1 and higher energy conduction bands. As these are not known, they are indicated with dashed horizontal lines. **ESA2** (pink) corresponds to the CB1 - CB2 (HE) transition at the M-point.

Furthermore, the non-instantaneous 500 fs rise in the GSB1 and ESA1 temporal traces coupled with the mirrored ultrafast decay of the GSB2 and ESA2 signals, together with the disappearance of the high energy wing of GSB1, is a direct result of the cooling of hot electrons and holes. We believe this cooling occurs along the k vector axis towards the conduction band minimum and valence band maximum respectively

for hot electrons and holes. The resulting charge carrier concentration exceeds the density of states at the CB minimum and VB maximum therefore the GSB1 signal remains spectrally broad for the duration of our measurement window. This apparent broadening of the optical bandgap due to the filling of states is common to semiconductors and as introduced previously, it is referred to as the Burstein-Moss effect.

Longer time following photoexcitation

The temporal evolution of the spectroscopic signals beyond 1 ps was fitted with the use of Equation 7.5, as shown in blue for the examples of Figure 7.4. The initial charge carrier density (n_0) was fixed to the calculated value above. On the other hand, the scaling parameter (α) was left free. This was done to correct for the aforementioned fact that the amplitudes of the spectroscopic signals are arbitrary in terms of the absolute population of photoexcited molecules, or in this case unit cells. The only exception is the bleaching signal corresponding to the pump pulse central wavelength ($\lambda = 388$ nm). Although this would give us a measure of the absolute percentage of photoexcited unit cells, we don't have access to the signal as it occurs at a lower wavelength than the span of our white light continuum probe pulse which terminates at approximately 450 nm. Furthermore, as we do not know the density of trap states present in our thin films, more particularly in the probed crystal domain, we also allowed y_0 to remain free in the fits.

From the fit function, we obtained values for the rate describing the geminate recombination of excitons (A) as well as for the rate per charge carrier density (B) describing the non-geminate recombination of free charge carriers.

The temporal decay of the higher energy ground state bleaching signal, **GSB2** (section d), is described by the associated rate constants of $A_{hot} = 1.5 \times 10^{10}$ s^{-1} (67 ps) and $B = 4.8 \times 10^{-8}$ $s^{-1}cm^3$. The extracted A_{hot} and B rate constants therefore correspond to the geminate and non-geminate recombination of *hot* excitons and free charge carriers respectively, at the M-point.

In addition, the temporal evolution of the optical bandgap bleaching signal, **GSB1** (section b), can also be well fitted with Equation 7.5. The resulting rate constants are $A_{cold} = 8.8 \times 10^9$ s^{-1} (114 ps) and $B = 4.5 \times 10^{-8}$ $s^{-1}cm^3$. As in the case of GSB2, the A_{cold} and B rate constants correspond to the geminate and non-geminate recombination of *cooled* excitons and free charge carriers respectively. In this instance however, the recombination occurs at the R-point.

The decay of the excited state absorption signal (**ESA1**, section c) corresponding to the conduction band minimum, is described by the associated rate constants of $A_{cold} = 7.0 \times 10^9$ s^{-1} (143 ps) and $B = 4.5 \times 10^{-8}$ $s^{-1}cm^3$. As ESA1 probes the population of electrons at the conduction band minimum, these A_{cold} and B rate constants are characteristic of the geminate and non-geminate recombination of *cold* excitons and free charge carriers respectively, at the R-point.

Finally, the rate constants obtained from the longer time temporal evolution of the near infrared **ESA2** signal (section a), are $A_{hot} = 1.5 \times 10^{10}$ s^{-1} (65 ps) and $B = 4.5 \times 10^{-8}$ $s^{-1}cm^3$. These rate constants are characteristic of the geminate (A_{hot}) and non-geminate (B) recombination of *hot* excitons and free charge carriers, near to the M-point.

From the rate constants obtained, we can once again pair the GSB1 and ESA1 signals as they have an almost identical temporal evolution on the longer time scale too, and

assign them to the R-point. The GSB2 and ESA2 signals can also be paired from their extremely similar longer time temporal evolutions and thus assigned near to the M-point. This serves as a second confirmation to the initial assignment of ESA1 and ESA2 shown in Figure 7.5.

An additional observation with respect to the temporal evolution of the spectroscopic signatures present in Figure 7.3 and their associated temporal traces presented in Figure 7.4, is that the lineouts, especially those corresponding to GSB1 and ESA1, do not decay to zero within our 500 ps measurement window. This baseline (y_0) is therefore a direct measure of the non-radiative trap mediated recombination specific to each perovskite thin film sample, which occurs on a > 1 ns timescale, as introduced above.

The fully consistent charge dynamics model

By combining the temporal traces (Figure 7.4) with the associated spectroscopic signatures and electronic band structure (Figures 7.3 and 7.5), we can build a consistent model depicting the charge dynamics which occur in $FA_{0.85}MA_{0.15}PbI_{2.55}Br_{0.45}$ following non-resonant photoexcitation with a laser pulse of 3.2 eV photon energy ($\lambda = 388$ nm).

As in the case of DSSCs, a schematic depicting this last step in our analysis procedure is shown in Figure 7.6. The conduction and valence bands of $FA_{0.85}MA_{0.15}PbI_{2.55}Br_{0.45}$, which take part in the initial photophysics are drawn together with the spectroscopic signatures observed in the transient absorption spectra: ESA1 (green), ESA2 (pink), GSB1 (red) and GSB2 (blue). The time constants associated with the short time dynamics are depicted by (gen) to indicate the *generation* of a spectroscopic signal and thus the increased population of a state. Conversely, (dep) is used to indicate the *depletion* of a spectroscopic signal and thus the depopulation of a state. On the longer time scale, the time and rate per charge carrier density constants associated with the filling of a state are labelled as (+), and the depopulation of a state as (-) in the sketch. The times and rates obtained from the temporal decays of the negative amplitude GSB1 and GSB2 are rather marked as (+), as they refer to the repopulation of the ground state. Moreover, the charge dynamics processes which can be observed in our TAS measurements are shown in the diagram, using arrows.

By linking the (dep) and (-) time and rate constants from the origin of an arrow, to the (gen) and (+) time and rate constants at the arrowhead, we assigned times and rates per charge carrier density to the various photoinduced charge dynamics processes. We constructed the simplest possible charge dynamics model which is fully consistent in this way, as presented in Figure 7.1 at the beginning of this chapter. Our reasoning was as outlined below.

The instantaneous generation of the GSB2 and ESA2 signals is an indication that they are both signatures of the hot charge carrier concentration away from the R-point. The subsequent < 500 fs decay of these two signals and mirrored rise of the GSB1 and ESA1 signals is an indication of the cooling dynamics taking place in the perovskite, and serves as a confirmation that GSB1 is characteristic to the optical bandgap transition and ESA1 to the electronic transition between the conduction band minimum and a higher resonant conduction band. As the population of hot charge carriers decreases, the population of cold charge carriers at the conduction band minimum and valence band maximum increases.

Furthermore, the two matching pairs of geminate recombination rate constants in-

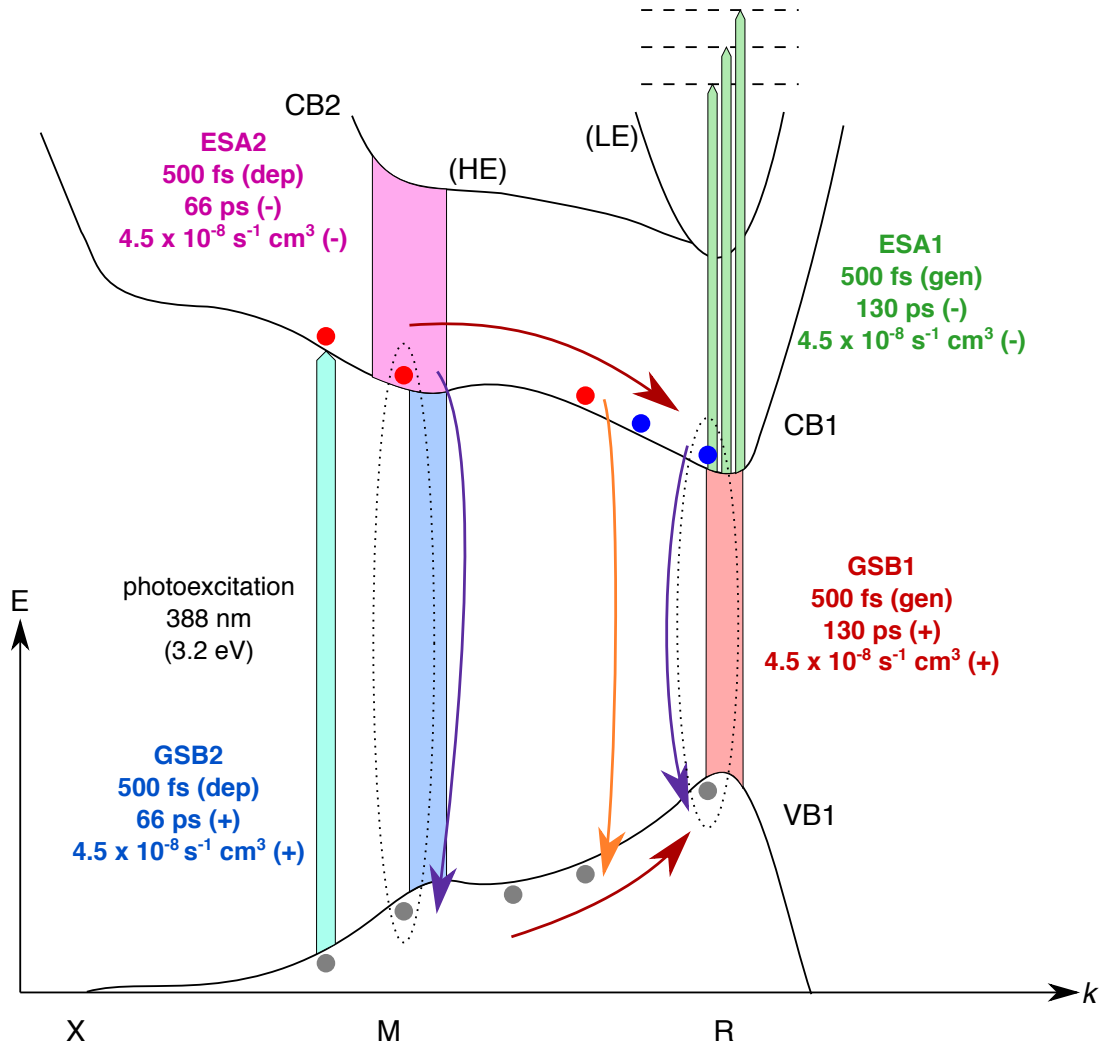

Figure 7.6: A simplified energy level diagram of the two lowest conduction bands (CB1 and CB2) and highest valence band (VB1) in $FA_{0.85}MA_{0.15}PbI_{2.55}Br_{0.45}$ drawn as a function of the k vector. Both the heavy (HE) and light (LE) electron portions of CB2 are depicted. Hot and cold electrons are shown in red and blue respectively, while holes are grey. The arrows depict the charge transfer processes which can be observed with our measurement technique. The diagram also depicts the spectroscopic signatures corresponding to: GSB1 (red), GSB2 (blue), ESA1 (green), ESA2 (pink). The short timescale time constants associated with the filling of a state are labelled as (gen) and the depopulation time constants are marked with a (dep). On the longer time scale, the time and rate per charge carrier density constants associated with the filling of a state are labelled as (+), and the depopulation of a state as (-)The times and rates obtained from the temporal decays of the negative amplitude GSB1 and GSB2 are rather marked as (+), as they refer to the repopulation of the ground state.To construct our charge transfer model, we link the (-) time or rate constant from the origin of an arrow, to the (+) time constant at the arrowhead, and assign the time or rate constant to the charge dynamics processes.

dicate that hot excitons recombine with an associated constant of $A_{hot} = 1.5 \times 10^{10}$ s^{-1} (66 ps) as obtained from the temporal evolutions of GSB2 and ESA2. On the other hand, cold excitons recombine with an associated rate of approximately $A_{cold} = 7.7 \times 10^{9}$ s^{-1} (130 ps) as obtained from the temporal evolutions of GSB1 and ESA1 at the R-point.

Finally, the non-geminate recombination rate per charge carrier density constant obtained from the fits of all four spectroscopic signatures was the same and determined to be $B = 4.5 \times 10^{-8}$ $s^{-1}cm^3$. This is an indication that non-geminate recombination doesn't depend on the energetic separation between the electron in CB1 and the hole in VB1, nor does it depend on the associated k vector.

As mentioned previously, although this investigation yielded the simplest possible consistent charge dynamics model, it is of course not the entire picture. Due to the high charge carrier densities generated in these types of laser experiments, we cannot exclude trimolecular processes such as the Auger recombination. This is also a possible reason for the overestimation of our non-geminate recombination rate per charge carrier density (B) in comparison to the B values reported for other mixed perovskite thin films (4.5×10^{-8} versus 10^{-10} $s^{-1}cm^3$). Therefore in order to more thoroughly and accurately investigate the recombination dynamics occurring in $FA_{0.85}MA_{0.15}PbI_{2.55}Br_{0.45}$, we carried out a detailed study of the effect of pump laser pulse fluence. A number of additional measurements were also carried out in order to better understand our material, which are presented in the sections that follow.

7.3 Recombination dependence on pump pulse fluence

To better understand the recombination dynamics occurring in perovskite materials, in particular $FA_{0.85}MA_{0.15}PbI_{2.55}Br_{0.45}$, we completed a series of measurements within a controlled experimental environment, with varying pump laser pulse energies (25 nJ, 50 nJ, 100 nJ, 200 nJ, 300 nJ, 500 nJ) and a pump beam focus diameter of 200 μm. These energies correspond to peak charge carrier densities of approximately 0.75, 1.5, 3, 6, 9, 15 $\times 10^{19}$ cm^{-3} respectively. The lowest value was unfortunately determined by the highly absorbing and light scattering nature of these multicrystalline thin films which compromised the sensitivity of our measurement technique. On the other hand, the largest pump pulse energy was selected as it was still below the damage threshold of our sample, and yielded a peak charge carrier density roughly an order of magnitude larger than the lowest pump pulse energy.

As previously mentioned the recombination rate constants are very highly dependent on the chemical composition and structure of the perovskite crystal. Furthermore, perovskite materials are dynamic. Therefore upon heating, ion migration can occur to yield iodine and bromine rich domains as well as a localised phase change in the crystal structure. To be able to compare our measurements directly, the same sample was used for all the TAS measurements and the experiments were performed successively over the course of 24 hours. Furthermore the pump and probe laser beams were overlapped on the same crystal domain for the complete set of measurements. In order to make the following analysis procedure easier to follow, I'll employ the charge carrier densities to differentiate between the measurements.

Temporal traces of ESA1

Temporal traces were extracted from the ESA1 absorption signal centred about 2.1 eV ($\lambda = 580 \pm 20$ nm) and compared for the various charge carrier densities, as per Figure 7.7. The data points are shown with an array of colours which correspond to the peak charge carrier densities in the legend, and the associated fit functions are presented with black lines. As expected, an increase in charge carrier density is mirrored by an increase in signal amplitude.

The temporal traces were fitted with the solution of the rate equation: either just including the first order, or the first and second orders, or all three. Once again, we always begin our fitting with the fewest possible free parameters and only add the

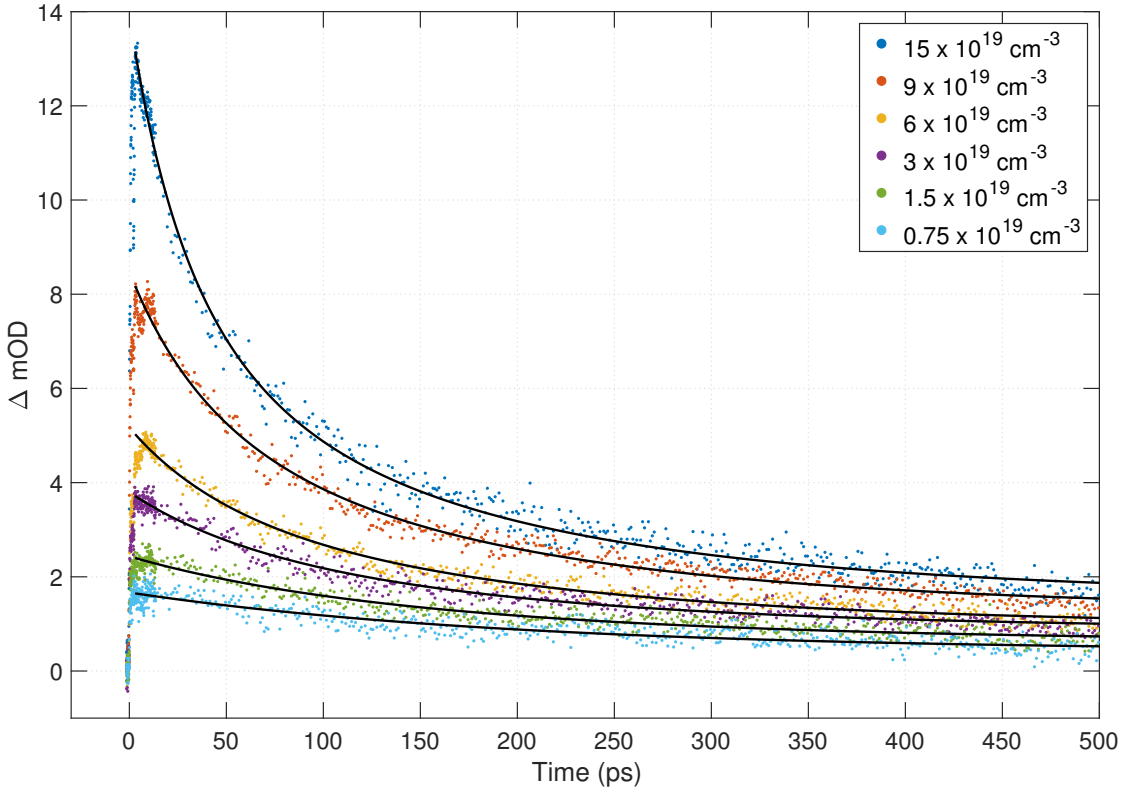

Figure 7.7: Temporal traces of change in optical density as a function of time (ΔOD(t)) were extracted from the R-point ESA1 absorption signal centred about 2.1 eV ($\lambda = 580 \pm 20$ nm) of a $FA_{0.85}MA_{0.15}PbI_{2.55}Br_{0.45}$ thin film photoexcited with a photon energy of 3.2 eV for various charge carrier densities of 0.75, 1.5, 3, 6, 9, 15 $\times 10^{19}$ cm^{-3} corresponding to pump laser pulse energies of 25, 50, 100, 200, 300 and 500 nJ. The data points are shown with an array of colours which correspond to the peak charge carrier densities in the legend, and the associated fit functions are presented with black lines (Equations 7.6, 7.7 and 7.8).

nonlinear contributions one by one if the mathematical fit fails. The analysis procedure and reasoning are presented in the subsections to follow.

0.75 $\times 10^{19}$ cm^{-3} trace

At low pump fluences, geminate recombination dominates and both non-geminate and Auger recombination processes are negligible. Our approach was therefore to make the assumption that when pumping with a laser pulse energy of 25 nJ, we were accessing mostly the geminate recombination regime, and the non-geminate and Auger recombination channels were not dominant. As seen from our previous measurements this is assumption might be elementary, but rather than fit with too many free parameters, we allowed the goodness of our fits to dictate at which pump pulse energy to begin including the nonlinear components. The temporal trace corresponding to a peak charge carrier density of 0.75 $\times 10^{19}$ cm^{-3}, was thus fitted with the first order solution to the recombination rate equation (Equation 7.1) given by:

$$\Delta OD(t)^{(1)} = \alpha e^{(At)} + y_0 \tag{7.6}$$

As previously mentioned, the amplitude of the change in optical density is proportional to the population density of a particular state. Therefore in addition to the

rate constant obtained for A $= 5 \pm 0.7 \times 10^9$ s^{-1} (200 ps), the proportionality constant was also determined ($\alpha = 1.25 \pm 0.06$), for an initial charge carrier density of 0.75 $\times 10^{19}$ cm^{-3}. As these two values are characteristic of the probed crystal domain of the material in question ($FA_{0.85}MA_{0.15}PbI_{2.55}Br_{0.45}$) and independent of the charge carrier density, they were kept constant throughout the remainder of the fits. The trap assisted monomolecular recombination was included with the help of a baseline $y_0 = 0.42 \pm 0.07$.

The A value which was obtained at this lower pump fluence from the ESA1 signal, matches very well with the previously obtained A_{cold} value for the geminate recombination at the R-point (200 ps vs 140 ps), even though the measurements were performed on two separate batches of samples, more than a year apart. Furthermore, from the goodness of this monoexponential fit in conjunction with the aforementioned observation, we can conclude that the assumption we made regarding non-geminate and Auger recombination not being dominant at this charge carrier density, was reasonable.

1.5 and 3 $\times 10^{19}$ cm^{-3} traces

Keeping in line with our approach of fitting data with the fewest free parameters possible, we included the non-geminate recombination contribution to the fit function and applied it to the remainder of the data as:

$$\Delta OD(t)^{(2)} = \frac{\alpha A n_0 f}{A e^{(At)} - B n_0 f + B n_0 f e^{(At)}} + y_0 \tag{7.7}$$

Equation 7.7 is the same as Equation 7.5, but contains an additional scaling factor (f). Rather than fixing the initial charge carrier density to the calculated value of 1.5 $\times 10^{19}$ cm^{-3} for a 50 nJ pulse, we allowed this parameter to be free by introducing the product $n_0 f$ instead, where $n_0 = 0.75 \times 10^{19}$ cm^{-3} is the charge carrier density for the 25 nJ pulse temporal trace. Furthermore we observed that the data acquired for charge carrier densities greater than 3 $\times 10^{19}$ cm^{-3}, could not be reasonably fitted with only the geminate and non-geminate recombination terms, as the function fails to fit the data at short times following photoexcitation, but required the Auger recombination contribution, see Figure 7.8. The coefficient of determination (R^2 value) of the fit decreases from 0.99 (typical for all the fits in Figure 7.7) to 0.96 when the third order term is excluded.

By keeping the α and A values fixed, and allowing the n_0 value to be adjusted for (with the factor f) in Equation 7.7, we obtained almost identical B values from the fits corresponding to the 1.5 and 3 $\times 10^{19}$ cm^{-3} traces in Figure 7.7. The average of the two B rate constants was calculated to be 1.1 $\times$ 10^{-10} $s^{-1}cm^3$. As it is unique to the probed crystal domain of the $FA_{0.85}MA_{0.15}PbI_{2.55}Br_{0.45}$ thin film sample, it was fixed as a constant for the remainder of the fits. The B value has been previously measured to be time dependent in perovskites, however on a nanosecond timescale – longer than our 600 ps measurement window [159].

6, 9 and 15 $\times 10^{19}$ cm^{-3} traces

Finally, the last three data sets were fitted with the fit function corresponding to Equation 7.8, where α, A, B and n_0 were kept constant, and the charge carrier density was

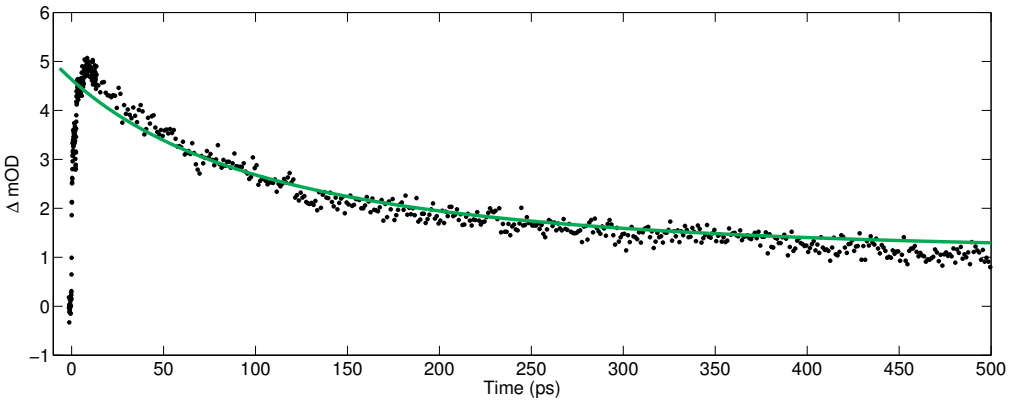

Figure 7.8: The temporal trace of change in optical density as a function of time corresponding to the ESA1 signal of the 6 $\times 10^{19}$ cm^{-3} charge carrier density (200 nJ pump pulse energy) measurement shown in Figure 7.7. The data points are depicted in black and a second order fit according to Equation 7.7 is shown in green. At short times the second order fit appears to fail. This is an indication that the Auger recombination contribution can no longer be excluded, and a third order fit is required for peak charge carrier densities exceeding 3 $\times 10^{19}$ cm^{-3}.

adjusted for with the factor f during the fitting process. As a reminder, the higher orders are only employed in deriving the fitting function, if they are needed for fitting the traces properly. By following this procedure, we ensure that we have a systematic result.

$$\Delta OD(t)^{(3)} = \frac{\alpha A n_0 f}{(A + B n_0 f)e^{(At)} - B n_0 f} - \frac{\alpha A^2 n_0^3 f^3 C(B n_0 f - B n_0 f e^{(At)} + (A + B n_0 f)e^{(At)} \log(\frac{A+B n_0 f - B n_0 f e^{(-At)}}{A}))}{B^2 n_0^2 f^2 (Ae^{(At)} + B n_0 f(e^{(At)}))^2} + y_0 \tag{7.8}$$

The C values which were obtained, are presented in Table 7.1 below, together with all the fit parameters and rate constants obtained for the above data.

Values obtained from the fits

Table 7.1 presented below contains all the values obtained from the mathematical fits of the ESA1 temporal traces shown in Figure 7.7. The values which were fixed for a given fit function, are displayed in grey to avoid confusion.

From the extracted C values presented in Table 7.1, we see that rather than remaining constant for the three individual measurements, these Auger recombination rate constants decrease with increasing charge carrier densities. As mentioned above, due to the dynamic nature of perovskite materials, especially mixed perovskites, this is not completely surprising. The heating of the sample at high pump fluences can cause a phase change in the perovskite crystal structure, which combined with ion migration, can lead to a variance in C values. We however don't observe arbitrarily different C values, but rather a decreasing trend with increasing charge carrier density. In order to formulate an explanation for this trend, we look to studies of Auger recombination for other semiconductors employed in photovoltaics, such as germanium and silicon [160].

n_0 $\times 10^{19}$ cm^{-3}	A $\times 10^{9}$ s^{-1}	B $\times 10^{-10}$ $s^{-1}cm^{3}$	C $\times 10^{-32}$ $s^{-1}cm^{6}$	y_0	α	f	f ratio w.r.t. max	n_0 ratio w.r.t. max
0.75	5.0 ± 0.7			0.42 ± 0.07	1.25 ± 0.06	1	0.1	0.05
1.5	5.0	1.0 ± 0.4		0.62 ± 0.04	1.25	1.5	0.1	0.1
3	5.0	1.1 ± 0.2		0.87 ± 0.03	1.25	2.3	0.2	0.2
6	5.0	1.1	51 ± 6	0.94 ± 0.02	1.25	3.4	0.3	0.4
9	5.0	1.1	8 ± 1	1.28 ± 0.04	1.25	5.8	0.6	0.6
15	5.0	1.1	1.7 ± 0.1	1.56 ± 0.04	1.25	9.9	1	1

Table 7.1: A table summarising all the values obtained from the mathematical fits of the fluence dependence measurements of Figure 7.7. The values which were fixed for a given fit function, are displayed in grey. The calculated initial charge carrier densities (n_0) of 0.75, 1.5, 3, 6, 9, 15 $\times 10^{19}$ cm^{-3} corresponding to the pump laser pulse energies of 25, 50, 100, 200, 300 and 500 nJ are presented in the first column. The first order rate constant **A** is associated to the geminate recombination of excitons. The second order rate constant **B** describes the non-geminate recombination of free charge carriers. The third order rate constant **C** is associated with the Auger recombination channel. The trap mediated recombination was included with the use of a baseline y_0 in the fit functions. α is a proportionality constant relating the charge carrier density to the change in optical density as $\alpha n(t) = \Delta OD(t)$. The factor f was a free parameter in the fitting function, and used to scale the charge carrier density of the lowest pump fluence measurement (0.75×10^{19} cm^{-3}) to the n_0 required by the fit. In the last two columns, the **ratio of the f value with respect to the maximum f value** was calculated to be compared to the **ratio of the calculated n_0 value with respect to the maximum n_0 value** (from the first column).

The Auger recombination rate per charge carrier density squared (C) has previously been determined to depend strongly on the bandgap energy of the semiconductor, as well as on temperature. At low charge carrier densities it is indeed a constant and independent of carrier concentrations. However, upon optical pumping with an associated photon energy much larger than the bandgap, as well as at high pump fluences, excess electron hole pairs are generated. This results in a non-equilibrium condition where the charge generation and recombination rates are no longer equal. As a result, the semiconductor becomes a conductor and the C value decreases as a function of the charge carrier density. This phenomenon is referred to as phase-space filling. From our measurements, we have directly observed this trend at charge carrier densities in the range of $6 - 15 \times 10^{19}$ cm^{-3} [161–163]. Another third order recombination channel which outcompetes the Auger recombination at high charge carrier densities, is amplified spontaneous emission [24].

Furthermore, we notice that our monomolecular recombination rates are similar to other reported values presented earlier in this chapter: geminate recombination of excitons occurs on the picosecond time scale ($\tau = 200$ ps, governed by the rate constant A) [147], and trap assisted recombination occurs with a time constant > 1 ns (reflected in the presence of baselines in our temporal traces) [47]. Additionally, the bimolecular non-geminate recombination of free electrons and holes also occurs with an associated rate per charge density (B) very similar to other perovskite materials, in the order of 10^{-10} $s^{-1}cm^{3}$ [144]. Conversely, the values which we obtained for the third order Auger recombination rate constant were in the order of 10^{-32} $s^{-1}cm^{6}$ – much smaller than previously reported values for other perovskites, in the order of 10^{-29} $s^{-1}cm^{6}$ [145], but rather in the same range as the C values determined for germanium ($\sim 10^{-32}$ $s^{-1}cm^{6}$) [162].

From Table 7.1, we can also observe that the baselines of the temporal traces describing the trap assisted monomolecular recombination, increase in amplitude (y_0) for increasing pump pulse fluences. This is expected as more trap states are populated as the charge carrier density increases.

As a reminder, when calculating the charge carrier density, we assumed that each incident photon is absorbed by the perovskite to generate an exciton or electron hole pair. This assumption means that in the calculation of the B and C rates, an overestimation of n_0 was employed (even though this value was scaled by f). Therefore the presented B and C values above, are rather lower limits to the actual rate constants per charge carrier density and per charge carrier density squared. As a final check of the initial charge carrier densities calculated n_0 versus those obtained from the fit functions with the scaling factor f, we calculated the ratios of the various n_0 and f values with respect to their maximum as shown in the last two columns of Table 7.1. By comparing the ratios, we see that they are almost identical therefore further confirming our analysis procedure.

The values in the table are also presented together with their error boundaries corresponding to 95% fit confidence. As a check, we reversed our fitting procedure and started with the highest charge carrier density lineout where we allowed all parameters to be free. The error boundaries corresponding to 95% confidence for the resulting rate constants obtained from the fit, increased by up to 3 orders of magnitude. This serves as an additional confirmation to our systematic fitting and analysis procedure outlined above.

Recombination rates

If we go back to the recombination rate equation describing the relaxation of a photoexcited perovskite crystal back to it's ground state (Equation 7.1), we can now fill in the obtained A, B and C values which can be measured in our temporal window, for a given crystal domain in the $FA_{0.85}MA_{0.15}PbI_{2.55}Br_{0.45}$ thin film. To complete the equation for a more general case, both the trap mediated and geminate monomolecular recombination rates would have to be included into the constant A.

$$\frac{dn}{dt} = (5 \times 10^{9} s^{-1})n + (10^{-10} s^{-1} cm^{3})n^{2} + (50 \times 10^{-32} s^{-1} cm^{6})n^{3} \tag{7.9}$$

Interestingly, even at high charge carrier densities where non-radiative Auger recombination dominates, the associated C values obtained for $FA_{0.85}MA_{0.15}PbI_{2.55}Br_{0.45}$ are much lower than other perovskite materials. In addition to the macroscopic reasons explaining why this particular material is such an excellent photoabsorber in highly efficient solar cell devices, we believe that the small non-radiative Auger recombination rate constants measured could be a fundamental physics contribution to its success.

7.4 Additional measurements

We carried out supporting TAS measurements to further investigate the unique spectral structure of the ESA1 signal of $FA_{0.85}MA_{0.15}PbI_{2.55}Br_{0.45}$ observed, and whether it is characteristic to the chemical composition of the perovskite, or rather an artefact caused by the encapsulation technique. In addition, we investigated the influence of the pump laser pulse photon energy on the transient absorption of the mixed

perovskite by photoexciting the samples with a 1.6 eV ($\lambda = 775$ nm) and a 2.6 eV ($\lambda = 480$ nm) pump pulse. Finally we measured the transient absorption spectra of perovskite layers contacted to electron and hole transport materials. These additional results are presented in the sections that follow.

Systematically varied perovskite compositions

To better investigate the three-band spectral structure of the ESA1 absorption signal of $FA_{0.85}MA_{0.15}PbI_{2.55}Br_{0.45}$ observed in TAS measurements, we studied a collection of perovskite thin films, with systematically varied chemical compositions and two different encapsulation methods. The two encapsulation techniques employed were introduced in the previous chapter and include either an additional PMMA layer covering the perovskite thin film sample, or a second glass slide sealed with epoxy, sandwiching the perovskite.

Comparing the transient absorption spectra

The collection of thin films which were measured to compare the different chemical compositions included four samples for each material, two of which were encapsulated with PMMA and two with glass and epoxy. These include: the primary material under investigation $FA_{0.85}MA_{0.15}PbI_{2.55}Br_{0.45}$, $FA_{0.85}MA_{0.15}PbI_3$, $FA_{0.5}MA_{0.5}PbI_3$, $FAPbI_3$ and $FA_{0.5}MA_{0.5}PbI_{1.5}Br_{1.5}$. Five representative transient absorption spectra, acquired in the visible spectral region, are presented in Figure 7.9, together with the associated perovskite material chemical compositions and vertical lineouts of the change in optical density as a function of wavelength ($\Delta OD(\lambda)$).

All of the transient absorption spectra presented in Figure 7.9, except that of $FA_{0.85}MA_{0.15}PbI_{2.55}Br_{0.45}$, contain a broad positive absorption signal corresponding to ESA1 without any distinct multi-band feature. We therefore assign the three-band spectral structure of the ESA1 signal as unique to $FA_{0.85}MA_{0.15}PbI_{2.55}Br_{0.45}$. Additionally, the optical bandgap ground state bleaching signals are not dominant due to the low fluence pump pulses employed for these measurements.

A possible explanation for this was already introduced in the previous chapters. The mixture of methylammonium cations with larger formamidinium molecules introduces a distortion of the perovskite crystal structure. Furthermore, it increases the possible spatial orientation permutations of the organic ions within the lead halide framework. This leads to an increased loss of degeneracy in the multiple conduction and valence bands of mixed methylammonium - formamidinium perovskite materials with respect to their single organic cation counterparts.

Furthermore, as expected, the substitution of I^- with Br^-, causes a shift in the bandgap (and therefore the GSB1 signal) towards higher energies. This can directly be observed in the TAS measurements of $FA_{0.85}MA_{0.15}PbI_{2.55}Br_{0.45}$ (leftmost spectrum) and $FA_{0.5}MA_{0.5}PbI_{1.5}Br_{1.5}$ (bottom right spectrum). Interestingly, the higher energy bleaching signal (GSB2) also appears to have shifted to higher energies for the bromine containing perovskites and is centred about $\lambda = 460$ nm instead of $\lambda = 480$ nm. This shift indicates that the energies of the states which govern the electronic transition associated with GSB2, are determined by the orbitals of the halogen anion. Therefore the source of the GSB2, is strongly dependent on the halogen content of the perovskite material.

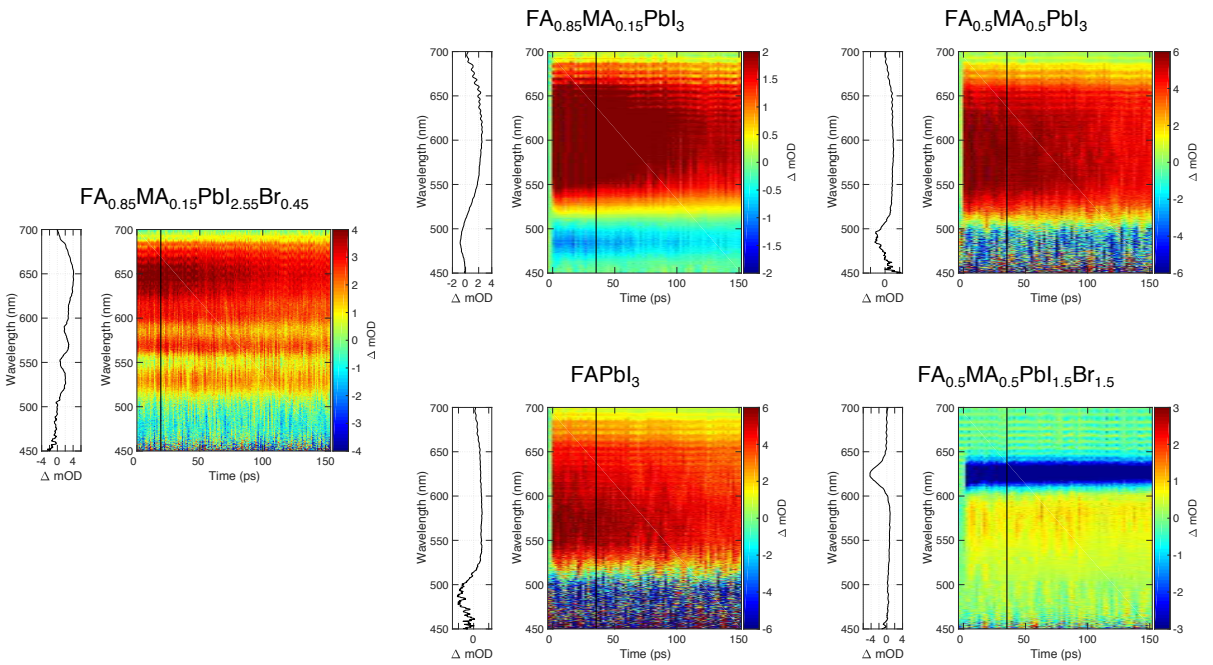

Figure 7.9: Five representative transient absorption spectra, acquired in the visible spectral region, are presented together with the associated perovskite material chemical compositions and vertical lineouts of the change in optical density as a function of wavelength. The leftmost transient corresponds to the primary material under investigation $FA_{0.85}MA_{0.15}PbI_{2.55}Br_{0.45}$, where a clear three-band ESA1 signal can be observed. A broadband ESA1 signal with no spectral structure is observed for the remaining transients: $FA_{0.85}MA_{0.15}PbI_3$ (top left), $FA_{0.5}MA_{0.5}PbI_3$ (top right), $FAPbI_3$ (bottom left) and $FA_{0.5}MA_{0.5}PbI_{1.5}Br_{1.5}$ (bottom right).

Effect of encapsulation

As previously mentioned, the crystal structure of perovskite photoabsorbers degrades fairly rapidly in the presence of water at room temperature, and is accelerated in the presence of heat. The thin film samples which we investigated, were therefore fabricated in a nitrogen environment and encapsulated to protect them from moisture.

In order to rule out any effect that the encapsulation method may have had on the three-band spectral structure of the ESA1 signal of $FA_{0.85}MA_{0.15}PbI_{2.55}Br_{0.45}$, we carried out a further series of measurements comparing TAS spectra. Four $FA_{0.85}MA_{0.15}PbI_{2.55}Br_{0.45}$ thin film samples which were prepared in a controlled environment in an identical manner to the ones employed for the charge dynamics models in this chapter, were investigated. All four samples were spin coated onto glass sides, two of which were encapsulated with PMMA and the other two were sealed with an additional glass slide and edges affixed with epoxy. Steady state absorption spectra were acquired for PMMA and epoxy, and are presented in Figure 7.10.

From the absorption spectra of Figure 7.10, it is evident that the PMMA does not exhibit a significant absorbance in the visible spectral region, however epoxy does. Furthermore, the glass substrate is transparent in visible and near infrared spectral regions. As the epoxy is merely used as a sealant, the amount present in the beam path of our TAS experiments is negligible. At most, the presence of epoxy will lead to a slightly lowered measurement sensitivity in the visible spectral region. Therefore for the purpose of our measurements, acquired in transmission, these encapsulation methods should not have a significant effect on the transient absorption spectra of the thin films. To check for this, we compared the transient absorption spectra of the $FA_{0.85}$-

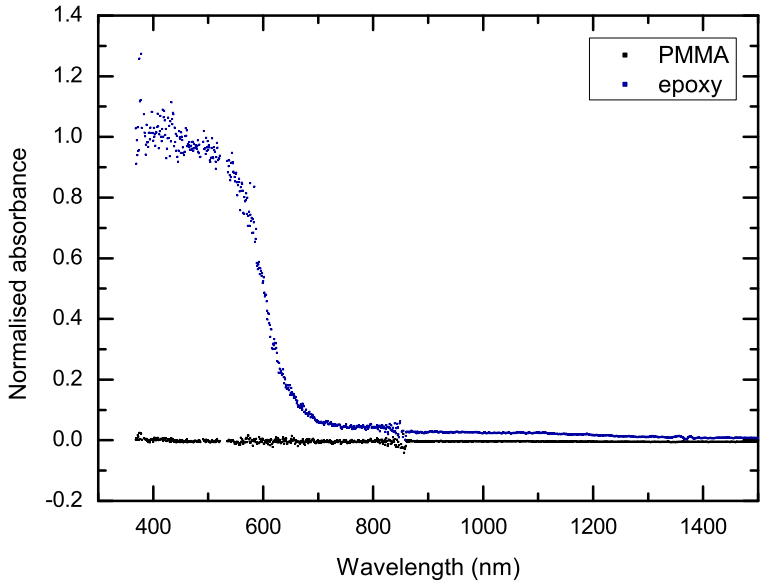

Figure 7.10: Steady state absorption spectra in the visible and near infrared spectral regions acquired for PMMA (black) and epoxy (blue). PMMA does not exhibit a significant absorbance, however epoxy does.

$MA_{0.15}PbI_{2.55}Br_{0.45}$ thin film samples encapsulated with the two different techniques, see Figure 7.11.

Four transient absorption spectra, acquired in the visible spectral region, are presented in Figure 7.11, together with the the associated encapsulation methods and vertical lineouts of the change in optical density as a function of wavelength ($\Delta OD(\lambda)$). Spectra a and b were obtained from samples encapsulated with PMMA, and spectra c and d from samples which were encapsulated with glass and sealed with epoxy.

From the spectral line outs accompanying the transient absorption spectra, it can easily be observed that the three-band spectral feature of the ESA1 signal characteristic to $FA_{0.85}MA_{0.15}PbI_{2.55}Br_{0.45}$, is indeed unaffected by the encapsulation method.

Photoexcitation with lower photon energies

In the preceding sections, the transient absorption data interpreted corresponded to the non-resonant photoexcitation of the perovskite thin films with a femtosecond laser pulse of 3.2 eV photon energy ($\lambda = 388$ nm), way above the bandgap. In addition, we also carried out measurements employing 2.6 eV and 1.6 eV photon energies ($\lambda = 480$ nm and $\lambda = 775$ nm). These resonant photoexcitation energies correspond directly to the two photoinduced ground state bleaching signals observed: GSB1 (bandgap electronic transition at the R-point), and GSB2 (electronic transition near to the M-point).

Although a series of TAS measurements were obtained and analysed, rather than presenting a collection of transient absorption spectra, the results are summarised in a sketch to aid with the explanation. Figure 7.12 is a drawing of the conduction and valence bands in $FA_{0.85}MA_{0.15}PbI_{2.55}Br_{0.45}$ which take part in the initial photophysics occurring upon optical pumping with an ultrashort laser pulse. In addition to the energy levels which are drawn as a function of the k vector, the observed spectroscopic

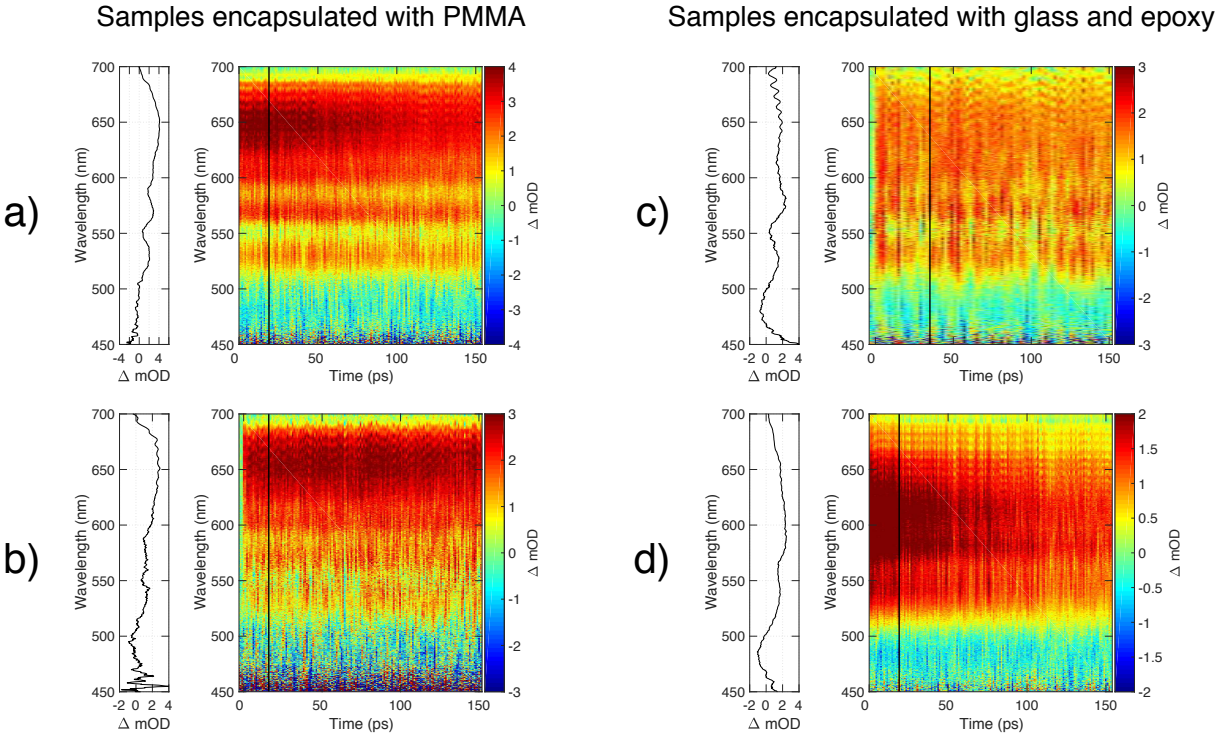

Figure 7.11: Four transient absorption spectra, acquired in the visible spectral region, are presented together with the the associated encapsulation methods and vertical lineouts of the change in optical density as a function of wavelength. Spectra a and b were obtained from samples encapsulated with PMMA, and spectra c and d from samples which were encapsulated with glass and sealed with epoxy. As these measurements were performed on an array of samples, a deviation in perovskite thin film quality can also be observed. From the TAS measurements, we can see that the encapsulation technique has no influence on the spectral shape of the $FA_{0.85}MA_{0.15}PbI_{2.55}Br_{0.45}$ spectroscopic signals.

signals are also shown. This diagram was used in the reasoning and building of the charge dynamics model, and different versions of it have been presented throughout this chapter. In addition, the three different photoexcitation energies are indicated with their associated central wavelengths. Observations pertaining to the four visible and near infrared spectroscopic signatures: GSB1, GSB2, ESA1 and ESA2, are also shown in the figure. The following discussion aims to support our assignment of spectral signatures and thus the charge dynamics model presented at the start of this chapter, by explaining these observations in more detail.

The spectral behaviour of the transient absorption spectra acquired with lower photon energy excitation (1.6 eV and 2.6 eV) was found to be very similar to that of photoexcitation with 3.2 eV photon energy. The spectral features assigned to **GSB1 and ESA1**, probing the electron population at the CB minimum, are present in the same spectral regions for all three sets of measurements. Moreover the three-band spectral shape of ESA1 is observed irrespective of the pump energy with matching central wavelengths. The spectral broadness of the GSB1 signal is narrowed upon pumping with lower pump energies. This is due to a decrease in the hot charge carrier density and thus confirms our assignment of the charge carrier cooling dynamic.

As reported in literature, and previously introduced in the preceding chapters, the **GSB2** signal is also present with lower photon energy excitation. Its relative amplitude with respect to the GSB1 signal is considerably smaller than in the case with 3.2 eV excitation (where it was already very weak) and diminishes with decreasing pump

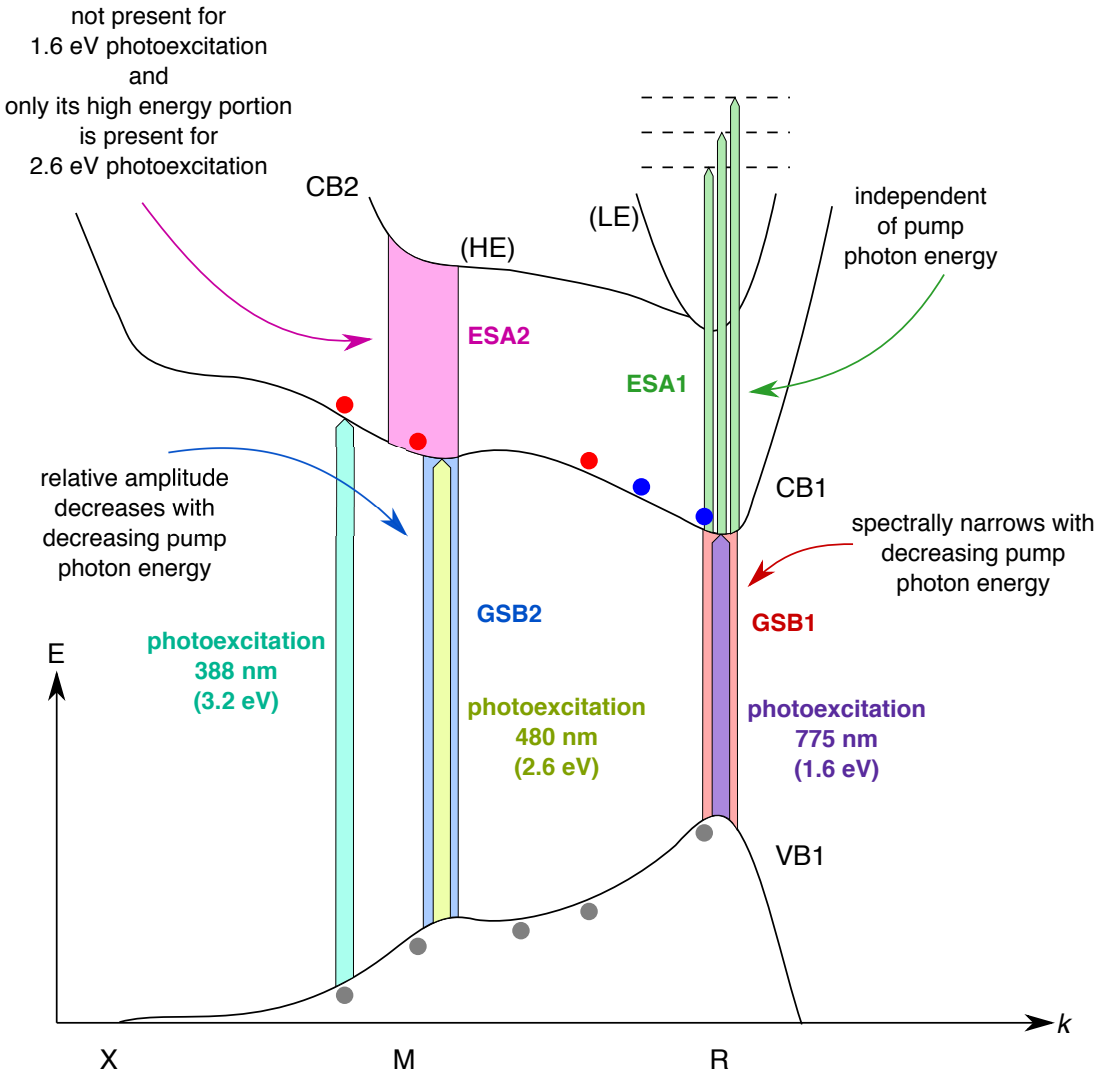

Figure 7.12: A simplified energy level diagram of the two lowest conduction bands (CB1 and CB2) and highest valence band (VB2) in $FA_{0.85}MA_{0.15}PbI_{2.55}Br_{0.45}$ drawn as a function of the k vector. Both the heavy (HE) and light (LE) electron portions of CB2 are depicted. The three photoexcitation energies employed in the TAS measurements are shown: 3.2 eV (turquoise), 2.6 eV (mustard) and 1.6 eV (purple). The effects of pumping with lower photon energies are summarised in the sketch for the spectroscopic signatures corresponding to: GSB1 (red), GSB2 (blue), ESA1 (green), ESA2 (pink).

energy. This indicates a strongly reduced electron and hole population away from the R-point, upon lower energy photoexcitation.

We did not detect hot electrons in the conduction band away from the R-point upon pumping with 1.6 eV photon energy (corresponding to the optical bandgap of the perovskite material) as indicated by the lack of **ESA2** signal in the near infrared spectral region. Additionally, only the high energy portion of the signal is detected with 2.6 eV excitation, thereby directly confirming that the ESA2 signal corresponds to the absorption of the hot electron population in the conduction band near to the M-point, which is only generated with sufficient pump laser pulse photon energies.

Finally, as an additional note, we observed that the temporal behaviour of the GSB1 and GSB2 signals is different upon bandgap photoexcitation (1.6 eV). This indicates that GSB1 and GSB2 correspond to the absorption of two different electron and hole populations, and fits with their assignment to the R- and M-points respectively.

Perovskite contacted to electron and hole transport materials

In order to complete the charge recombination dynamics model presented at the start of this chapter, we investigated the effect of contacting the $FA_{0.85}MA_{0.15}PbI_{2.55}Br_{0.45}$ perovskite thin film to either an electron transport material (ETM), a hole transport material (HTM), or both. The two transport materials selected for the purpose of this study were PCBM and PEDOT:PSS due to the correct electronic band alignment between these materials and the mixed perovskite under investigation, combined with their ease of acquisition and ability to be deposited via the spin coating method. For further information regarding the chemical composition of these thin films samples, please refer to Chapter 6.

Figure 7.13 is an energy diagram depicting the conduction band (CB) minimum and valence band (VB) maximum of $FA_{0.85}MA_{0.15}PbI_{2.55}Br_{0.45}$ together with the highest occupied (HOMO) and lowest unoccupied (LUMO) molecular orbital energies of PCBM and PEDOT:PSS [134]. From the diagram, it can be observed that the energy separation between the charge donor and acceptor states of the perovskite and the ETM and HTM, should be sufficient to facilitate efficient charge transfer. Furthermore, from previous studies, we expect electrons to be injected into the ETM and holes into the HTM on similar timescales [164].

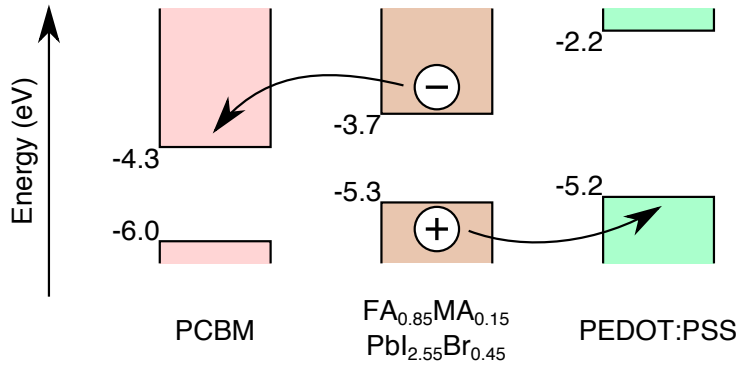

Figure 7.13: An energy diagram depicting the conduction band minimum and valence band maximum of $FA_{0.85}MA_{0.15}PbI_{2.55}Br_{0.45}$ [134] together with the highest occupied and lowest unoccupied molecular orbital energies of PCBM and PEDOT:PSS with respect to the vacuum level energies. The potential difference between the charge donor and acceptor states of the perovskite and the electron and hole transport materials should be sufficient to facilitate efficient charge transfer.

The change in optical density as a function of time and wavelength was once again measured with femtosecond TAS in the visible and near infrared spectral regions. The photon energy of the pump laser pulse employed for photoexcitation was set to 1.6 eV ($\lambda = 775$ nm), to match the bandgap of the $FA_{0.85}MA_{0.15}PbI_{2.55}Br_{0.45}$ photoabsorber. The data presented bellow serves to explain the contributions of the PCBM and PEDOT:PSS qualitatively. Therefore rate constants corresponding to the newly available charge transfer channels were not determined.

ESA1

Figure 7.14 is a collection of normalised temporal traces corresponding to the three-band ESA1 signal of four thin film samples: pure $FA_{0.85}MA_{0.15}PbI_{2.55}Br_{0.45}$ perovskite (labeled as FAI), perovskite contacted to PCBM (FAI | PCBM), perovskite contacted to

PEDOT:PSS (PEDOT | FAI) and perovskite contacted to both PEDOT:PSS and PCBM (PEDOT | FAI | PCBM). As a reminder from the previous chapter, these samples were not completed with electrodes and are therefore not fully operational solar cells.

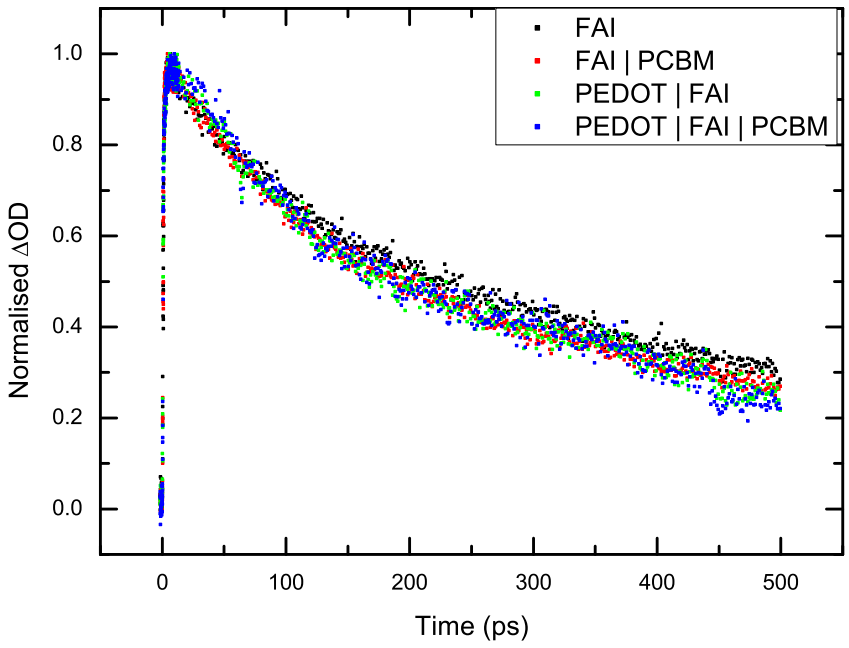

Figure 7.14: A collection of normalised temporal traces of change in optical density as a function of time, corresponding to the visible excited state absorption (ESA1) signal of four thin film samples: pure $FA_{0.85}MA_{0.15}PbI_{2.55}Br_{0.45}$ perovskite (FAI, black), perovskite contacted to PCBM (FAI | PCBM, red), perovskite contacted to PEDOT:PSS (PEDOT | FAI, green) and perovskite contacted to both PEDOT:PSS and PCBM (PEDOT | FAI | PCBM, blue). The samples were photoexcited with 1.6 eV photon energy, corresponding to the bandgap of the perovskite.

From Figure 7.14, we can see that the temporal dynamics of ESA1 are the same for the four samples. This suggests that the ESA1 signal, a measure of the electron population at the conduction band minimum, does not depend on the presence of contact layers. This result indicates poor charge transfer from the electron donating $FA_{0.85}MA_{0.15}PbI_{2.55}Br_{0.45}$ into the electron accepting PCBM. Therefore only the hot electrons (very few due to optical bandgap photoexcitation) in the CB electron distribution are injected into the PCBM layer.

GSB1 and GSB2

The normalised temporal lineouts of the GSB1 signal measured for the four samples, are presented in Figure 7.15. The fastest decay corresponds to the pristine $FA_{0.85}MA_{0.15}PbI_{2.55}Br_{0.45}$ thin film (labeled as FAI). Upon addition of either the electron transport material (labeled FAI | PCBM) or the hole transport material (labeled PEDOT | FAI) the signal is longer lived. This indicates that photoexcited electrons and holes are extracted into PCBM and PEDOT:PSS respectively, reducing the charge recombination at the R-point. In the instance that the perovskite layer is contacted to both PCBM and PEDOT:PSS (labelled PEDOT | FAI | PCBM), we observe that the GSB1 signal decay is

even further suppressed. This reduces the charge carrier recombination at the R-point even further.

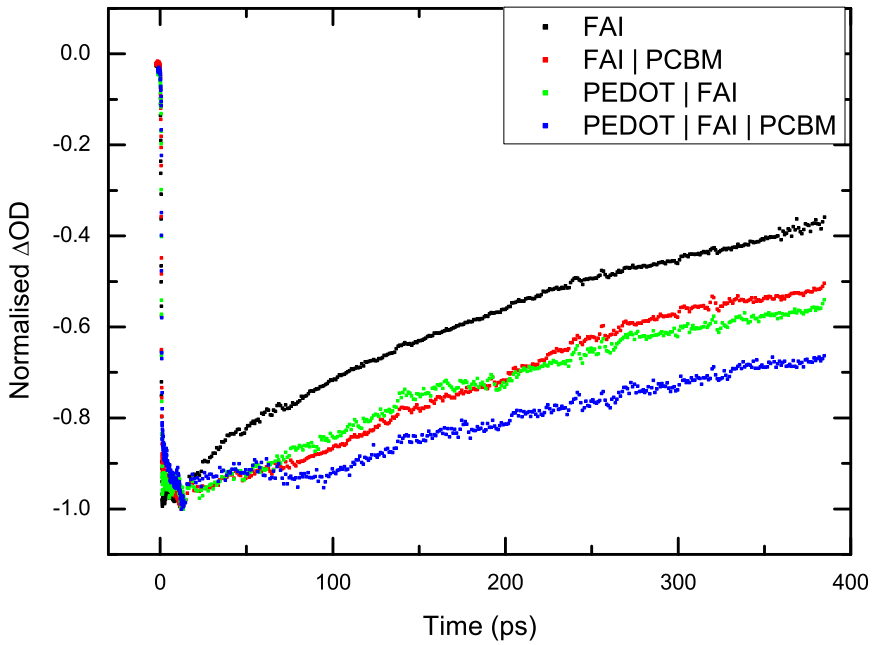

Figure 7.15: The normalised temporal traces of change in optical density as a function of time, corresponding to the optical bandgap bleaching (GSB1) signal of four thin film samples: pure $FA_{0.85}MA_{0.15}PbI_{2.55}Br_{0.45}$ perovskite (FAI, black), perovskite contacted to PCBM (FAI | PCBM, red), perovskite contacted to PEDOT:PSS (PEDOT | FAI, green) and perovskite contacted to both PEDOT:PSS and PCBM (PEDOT | FAI | PCBM, blue). The samples were photoexcited with 1.6 eV photon energy, corresponding to the bandgap of the perovskite.

The trend observed in Figure 7.15 is expected from the ground state bleaching signal of a photoabsorber when it is contacted to either an electron or a hole transport layer, or both. The injection of free charges into these contact layers results in a reduction of the charge carrier recombination at the $FA_{0.85}MA_{0.15}PbI_{2.55}Br_{0.45}$ bandgap.

As mentioned above, although a GSB2 signal is generated upon pumping with 1.6 eV ($\lambda = 775$ nm) photon energy, its amplitude is extremely weak. The signal quality was too poor in all four measurements for any kind of interpretation.

ESA2

Figure 7.16 consists of four transient absorption spectra acquired in the near infrared spectral region, corresponding to the thin film samples: pure $FA_{0.85}MA_{0.15}PbI_{2.55}Br_{0.45}$ perovskite (labeled as FAI), perovskite contacted to PCBM (FAI | PCBM), perovskite contacted to PEDOT:PSS (PEDOT | FAI) and perovskite contacted to both PEDOT:PSS and PCBM (labeled as PEDOT | FAI | PCBM).

From the figures, it is obvious that the ESA2 signal which we attributed to the absorption of hot electrons in the conduction band, is not present upon 1.6 eV photoexcitation (at the bandgap). Furthermore, it is interesting to note that the PCBM radical anion absorption signal (which is centred at 1020 nm [165]) is also not present. This is

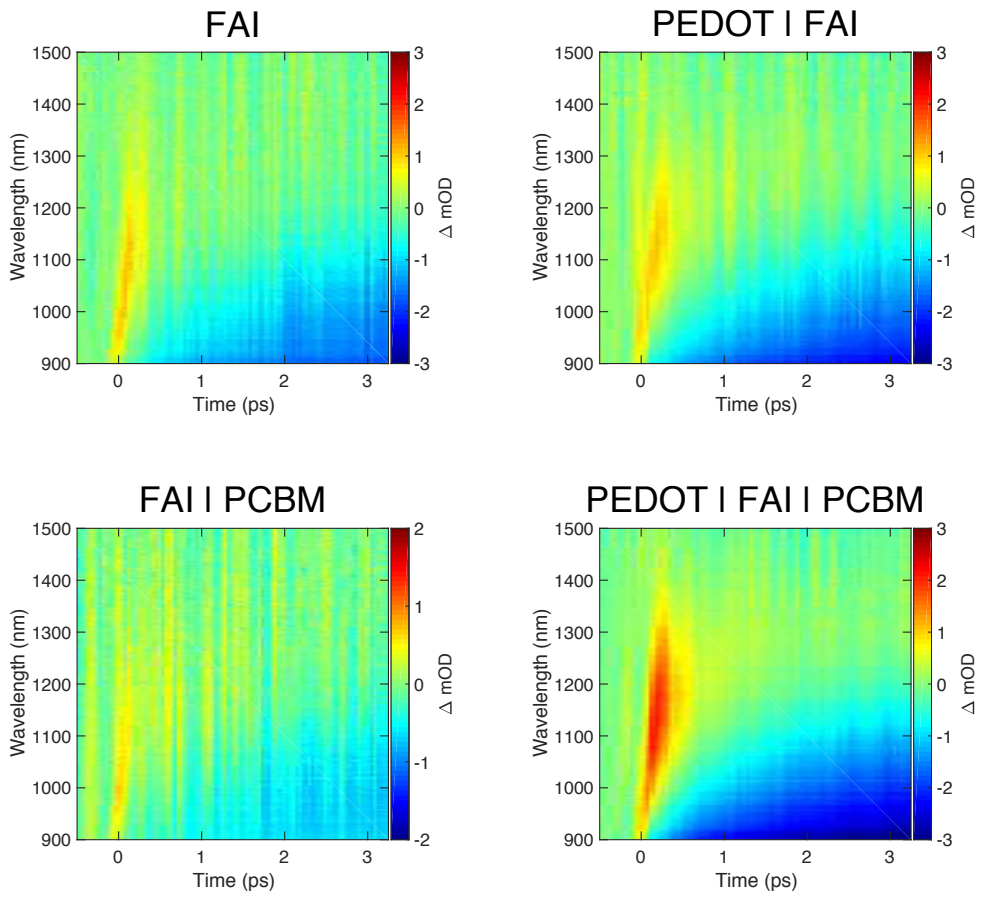

Figure 7.16: Four transient absorption spectra of change in optical density as a function of wavelength and time, acquired in the near infrared spectral region (where the ESA2 signal is expected). The samples were photoexcited with 1.6 eV photon energy, corresponding to the bandgap of the perovskite: pure $FA_{0.85}MA_{0.15}PbI_{2.55}Br_{0.45}$ perovskite (FAI), perovskite contacted to PCBM (FAI | PCBM), perovskite contacted to PEDOT:PSS (PEDOT | FAI) and perovskite contacted to both PEDOT:PSS and PCBM (PEDOT | FAI | PCBM).

an indication that the majority of photoexcited electrons in the conduction band, near to its minimum, are not injected into the LUMO of the PCBM. This is perhaps due to the insufficient coupling between the two energy levels.

8. Summary and Outlook

We employed femtosecond transient absorption spectroscopy (TAS) in the visible and near infrared spectral regions to follow the photoinduced charge dynamics in real time in fully operational dye sensitised solar cells (DSSCs) and perovskite thin films. By combining the spectroscopic signatures of the investigated samples with the allowed electronic transitions which occur in the materials, and following their temporal evolutions, we constructed the simplest possible fully consistent charge dynamics models for the kinetics which occur on these ultrafast timescales. Our main goal was to learn about the fundamental physics processes which dominate the generation and extraction of charges in DSSCs and perovskite solar cells in the conversion of solar energy to electrical energy.

In particular we were interested in the photophysics governing the electron transfer from a photoexcited indoline dye (DN216) into electrodeposited ZnO as well as the possible microscopic reasons why ZnO based DSSCs have not yet reached the same efficiencies as their TiO_2 counterparts. On the other hand, the solar cells which contain the mixed perovskite photoabsorber $FA_{0.85}MA_{0.15}PbI_{2.55}Br_{0.45}$ boasted record power conversion efficiencies (PCEs) at the time our study commenced, and still continue to be among the best. We were therefore interested in the fundamental reasons contributing to the success of this specific perovskite chemical composition. Especially, learning how charge is generated and extracted, the possible recombination channels which can occur and their dependence on the charge carrier density.

Dye sensitised solar cells

By probing the population dynamics of the injected electrons in the ZnO conduction band (CB), we observed that the charge injection from the photoexcited indoline dye into ZnO occurs directly (with an associated time constant < 200 fs), but also in a stepwise manner via intermediate charge transfer states. These charge transfer states are generated as a result of the orbital overlap between trap states on the surface of electrodeposited ZnO and the lowest unoccupied molecular orbital (LUMO) of the dye molecules. They are distinguished based on their electronic character as: neutral (NCT) or ionic (ICT) charge transfer states, where the resulting bonding hybrid orbital is either closest in energy to the LUMO of the dye (neutral), or the ZnO surface trap (ionic). We observed the electron injection into the charge transfer states to be ultrafast (< 100 fs), while the subsequent injection from the charge transfer states into the ZnO CB to occur slower: 2 ps out of the higher energy NCT state and 10 ps out of the lower energy ICT state. The larger time constants associated to the stepwise electron injection increase the opportunity for recombination to take place.

From a TAS point of view, this study was a first direct measure of the absorption of the electrons in the ZnO CB injected from the photoexcited indoline dye DN216

($>$ 2000 nm), and required the development of a near infrared probe laser source. Furthermore, with the use of our extended probing window, we observed the broadband absorption signals of the NCT and ICT states. Prior to this work, these were not known.

This stepwise injection is unique to electrodeposited ZnO and a fundamental physics reason behind the lower PCEs of ZnO based DSSCs.

With this knowledge, a possible way forward in the development of ZnO DSSCs toward higher PCEs would be to engineer the surface of electrodeposited ZnO in order to minimise the trap states available and thus favour the ultrafast direct electron injection channel.

Perovskite thin films

Upon non-resonant photoexcitation of a $FA_{0.85}MA_{0.15}PbI_{2.55}Br_{0.45}$ thin film, with 3.2 eV photon energy (way above the bandgap), we observed the initial ultrafast cooling ($<$ 500 fs) of hot electrons and holes from our TAS measurements. This cooling along the k vector axis is rivalled by the geminate recombination of excitons, which occurs with an associated time constant of 66 ps at the M-point, and is slowed towards the R-point (to 130 ps). We also observed the competing non-geminate recombination of free charge carriers and measured an associated rate per charge density constant of 4.5×10^{-8} $s^{-1}cm^3$ which is independent of the associated k vector.

To determine why our analysis procedure was fully consisted even though we excluded the third order Auger recombination process, we performed a series of measurements with varying initial charge carrier densities. From the results, we were able to once again extract the geminate and non-geminate recombination time and rate constants (A $\sim$ 200 ps, B $\sim$ 10^{-10} $s^{-1}cm^3$) which are independent of charge carrier density and fixed for a crystal domain of the measured $FA_{0.85}MA_{0.15}PbI_{2.55}Br_{0.45}$ thin film. Additionally, we measured the Auger recombination rate constant (C $\sim$ $2 - 50 \times 10^{-32}$ $s^{-1}cm^6$) and observed that it is dependent on the charge carrier density as the perovskite semiconductor behaves more like a metal at high pump fluences. The non-radiative Auger recombination rate (C) thus decreases for increasing charge carrier density.

From a TAS perspective, this work was a first observation of the three-band spectral feature of the excited state absorption signal in the visible spectral region characteristic to $FA_{0.85}MA_{0.15}PbI_{2.55}Br_{0.45}$, which is unaffected by the encapsulation technique.

Moreover, the calculated C range is specific to $FA_{0.85}MA_{0.15}PbI_{2.55}Br_{0.45}$ and even at high charge carrier densities it is smaller than the C values determined for other perovskite materials, but rather more similar to that of silicon and germanium. As non-radiative recombination is detrimental towards achieving high efficiency solar cells, the low Auger recombination rate constant range which we measured contributes to the success of $FA_{0.85}MA_{0.15}PbI_{2.55}Br_{0.45}$ as a photoabsorber in state of the art perovskite solar cells, from a fundamental physics perspective.

As the field of perovskite solar cells is still young and fast developing, a potential outlook would be to determine how the recombination rate constants (A, B and C) depend on the various crystal domains of $FA_{0.85}MA_{0.15}PbI_{2.55}Br_{0.45}$ as well as how they change in fully operational solar cells. Furthermore, with the knowledge that the Auger recombination is much less dominant than expected in $FA_{0.85}MA_{0.15}PbI_{2.55}Br_{0.45}$, the material can be engineered further to produce cells which are more stable in ambient conditions and provide higher PCEs.

Bibliography

[1] Shirley, J.H.: *Encyclopedia of World Climatology*. Springer Netherlands, 2005.

[2] Hagfeldt, A., Boschloo, G., Sun, L., Kloo, L. and Pettersson, H.: Dye-Sensitized Solar Cells. *Chemical Reviews*, vol. 110, no. 11, pp. 6595–6663, 2010.

[3] Schiermeier, Q., Tollefson, J., Scully, T., Witze, A. and Morton, O.: Energy alternatives: Electricity without carbon. *Nature*, vol. 454, no. 7206, pp. 816–823, August 2008.

[4] NREL: Solar Spectrum. Online, . Acessed 30-03-2017.
Available at: http://rredc.nrel.gov/solar/spectra

[5] Nelson, C.A., Monahan, N.R. and Zhu, X.Y.: Exceeding the Shockley-Queisser limit in solar energy conversion. *Energy & Environmental Science*, vol. 6, no. 12, pp. 3508–3519, 2013.

[6] Sessolo, M. and Bolink, H.J.: Perovskite solar cells join the major league. *Science*, vol. 350, no. 6263, p. 917, November 2015.

[7] Shockley, W. and Queisser, H.J.: Detailed Balance Limit of Efficiency of p-n Junction Solar Cells. *Journal of Applied Physics*, vol. 32, no. 3, pp. 510–519, March 1961.

[8] Green, M.A.: *Third Generation Photovoltaics: Advanced Solar Energy Conversion*, vol. 12 of *Springer series in photonics*. Springer, Berlin, Heidelberg, 2006.

[9] Green, M.A., Emery, K., Hishikawa, Y., Warta, W., Dunlop, E.D., Levi, D.H. and Ho-Baillie, A.W.Y.: Solar cell efficiency tables (version 49). *Progress in Photovoltaics: Research and Applications*, vol. 25, no. 1, pp. 3–13, 2017.

[10] NREL: Best Research-Cell Efficiencies. Online, . Acessed 15-02-2017.
Available at: https://www.nrel.gov/pv/assets/images/efficiency-chart.png

[11] Lee, T.D. and Ebong, A.U.: A review of thin film solar cell technologies and challenges. *Renewable and Sustainable Energy Reviews*, vol. 70, pp. 1286–1297, April 2017.

[12] Mazzio, K.A. and Luscombe, C.K.: The future of organic photovoltaics. *Chemical Society Reviews*, vol. 44, no. 1, pp. 78–90, December 2014.

[13] Marinova, N., Valero, S. and Delgado, J.L.: Organic and perovskite solar cells: Working principles, materials and interfaces. *Journal of Colloid and Interface Science*, vol. 488, pp. 373–389, February 2017.

[14] Etxebarria, I., Ajuria, J. and Pacios, R.: Solution-processable polymeric solar cells: A review on materials, strategies and cell architectures to overcome 10%. *Organic Electronics*, vol. 19, pp. 34–60, 2015.

[15] Sauvé, G. and Fernando, R.: Beyond Fullerenes: Designing Alternative Molecular Electron Acceptors for Solution-Processable Bulk Heterojunction Organic Photovoltaics. *The Journal of Physical Chemistry Letters*, vol. 6, no. 18, pp. 3770–3780, 2015.

[16] Menke, S.M. and Holmes, R.J.: Exciton diffusion in organic photovoltaic cells. *Energy & Environmental Science*, vol. 7, no. 2, pp. 499–512, January 2014.

[17] Krebs, F.C., Hösel, M., Corazza, M., Roth, B., Madsen, M.V., Gevorgyan, S.A., Søndergaard, R.R., Karg, D. and Jørgensen, M.: Freely available OPV – The fast way to progress. *Energy Technology*, vol. 1, no. 7, pp. 378–381, 2013.

[18] Chandiran, A.K., Abdi-Jalebi, M., Nazeeruddin, M.K. and Grätzel, M.: Analysis of Electron Transfer Properties of ZnO and TiO_2 Photoanodes for Dye-Sensitized Solar Cells.

ACS Nano, vol. 8, no. 3, pp. 2261–2268, February 2014.

[19] Kumavat, P.P., Sonar, P. and Dalal, D.S.: An overview on basics of organic and dye sensitized solar cells, their mechanism and recent improvements. *Renewable and Sustainable Energy Reviews*, vol. 78, pp. 1262–1287, October 2017.

[20] Hagfeldt, A. and Grätzel, M.: Molecular Photovoltaics. *Accounts of Chemical Research*, vol. 33, no. 5, pp. 269–277, May 2000.

[21] Grätzel, M.: Dye-sensitized solar cells. *Journal of Photochemistry and Photobiology C: Photochemistry Reviews*, vol. 4, no. 2, pp. 145–153, October 2003.

[22] Gorlov, M. and Kloo, L.: Ionic liquid electrolytes for dye-sensitized solar cells. *Dalton Transactions*, vol. 353, no. 20, pp. 2655–2666, 2008.

[23] O'Regan, B. and Grätzel, M.: Low cost and highly efficient solar cells based on the sensitization of colloidal titanium dioxide. *Nature*, 1991.

[24] Mathew, S., Yella, A., Gao, P. and Humphry-Baker, R.: Dye-sensitized solar cells with 13% efficiency achieved through the molecular engineering of porphyrin sensitizers. *Nature*, 2014.

[25] Lange, I., Reiter, S., Ptzel, M., Zykov, A., Nefedov, A., Hildebrandt, J., Hecht, S., Kowarik, S., Wll, C., Heimel, G. and Neher, D.: Tuning the Work Function of Polar Zinc Oxide Surfaces using Modified Phosphonic Acid Self-Assembled Monolayers. *Advanced Functional Materials*, vol. 24, no. 44, pp. 7014–7024, 2014.

[26] Ito, S., Miura, H., Uchida, S., Takata, M., Sumioka, K., Liska, P., Comte, P., Péchy, P. and Grätzel, M.: High-conversion-efficiency organic dye-sensitized solar cells with a novel indoline dye. *Chemical Communications*, vol. 353, no. 41, pp. 5194–5196, October 2008.

[27] Strothkämper, C., Bartelt, A., Sippel, P., Hannappel, T., Schütz, R. and Eichberger, R.: Delayed Electron Transfer through Interface States in Hybrid ZnO/Organic-Dye Nanostructures. *The Journal of Physical Chemistry C*, vol. 117, no. 35, pp. 17901–17908, August 2013.

[28] El-Zohry, A.M. and Zietz, B.: Concentration and Solvent Effects on the Excited State Dynamics of the Solar Cell Dye D149: The Special Role of Protons. *The Journal of Physical Chemistry C*, vol. 117, no. 13, pp. 6544–6553, March 2013.

[29] El-Zohry, A., Orthaber, A. and Zietz, B.: Isomerization and Aggregation of the Solar Cell Dye D149. *The Journal of Physical Chemistry C*, vol. 116, no. 50, pp. 26144–26153, December 2012.

[30] Burdziński, G., Karolczak, J. and Ziółek, M.: Dynamics of local Stark effect observed for a complete D149 dye-sensitized solar cell. *Physical Chemistry Chemical Physics*, vol. 15, no. 11, pp. 3889–3896, February 2013.

[31] Katoh, R., Furube, A., Hara, K., Murata, S., Sugihara, H., Arakawa, H. and Tachiya, M.: Efficiencies of Electron Injection from Excited Sensitizer Dyes to Nanocrystalline ZnO Films as Studied by Near-IR Optical Absorption of Injected Electrons. *American Chemical Society*, vol. 106, November 2002.

[32] Furube, A., Katoh, R., Yoshihara, T., Hara, K., Murata, S., Arakawa, H. and Tachiya, M.: Ultrafast Direct and Indirect Electron-Injection Processes in a Photoexcited Dye-Sensitized Nanocrystalline Zinc Oxide Film: The Importance of Exciplex Intermediates at the Surface. *American Chemical Society*, vol. 108, July 2004.

[33] Katoh, R., Furube, A., Yoshihara, T., Hara, K., Fujihashi, G., Takano, S., Murata, S., Arakawa, H. and Tachiya, M.: Efficiencies of Electron Injection from Excited N3 Dye into Nanocrystalline Semiconductor (ZrO_2, TiO_2, ZnO, Nb_2O_5, SnO_2, In_2O_3) Films. *American Chemical Society*, vol. 108, March 2004.

[34] Furube, A., Katoh, R., Hara, K., Murata, S., Arakawa, H. and Tachiya, M.: Ultrafast Stepwise Electron Injection from Photoexcited Ru-Complex into Nanocrystalline ZnO Film via Intermediates at the Surface. *American Chemical Society*, vol. 107, April 2003.

[35] Sobuś, J., Burdziński, G., Karolczak, J., Idígoras, J., Anta, J.A. and Ziółek, M.: Compari-

son of TiO_2 and ZnO Solar Cells Sensitized with an Indoline Dye: Time-Resolved Laser Spectroscopy Studies of Partial Charge Separation Processes. *Langmuir*, vol. 30, no. 9, pp. 2505–2512, February 2014.

[36] Sobuś, J., Karolczak, J., Komar, D., Anta, J.A. and Ziółek, M.: Transient states and the role of excited state self-quenching of indoline dyes in complete dye-sensitized solar cells. *Dyes and Pigments*, vol. 113, pp. 692–701, February 2015.

[37] Oum, K., Lohse, P.W., Flender, O., Klein, J.R., Scholz, M., Lenzer, T., Du, J. and Oekermann, T.: Ultrafast dynamics of the indoline dye D149 on electrodeposited ZnO and sintered ZrO_2 and TiO_2 thin films. *Physical Chemistry Chemical Physics*, vol. 14, no. 44, pp. 15429–15437, October 2012.

[38] Rohwer, E.: *Ultrafast photodynamics of ZnO solar cells sensitized with the organic indoline derivative D149*. Ph.D. thesis, Stellenbosch University, April 2014.

[39] Minda, I.: *Photoinduced charge dynamics in indoline-dye sensitised solar cells*. Master's thesis, Stellenbosch University, December 2014.

[40] Rohwer, E., Richter, C., Heming, N., Strauch, K., Litwinski, C., Nyokong, T., Schlettwein, D. and Schwoerer, H.: Ultrafast Photodynamics of the Indoline Dye D149 Adsorbed to Porous ZnO in Dye-Sensitized Solar Cells. *ChemPhysChem*, vol. 14, no. 1, pp. 132–139, January 2013.

[41] Rohwer, E., Minda, I., Tauscher, G., Richter, C., Miura, H., Schlettwein, D. and Schwoerer, H.: Ultrafast Charge-Transfer Reactions of Indoline Dyes with Anchoring Alkyl Chains of Varying Length in Mesoporous ZnO Solar Cells. *ChemPhysChem*, vol. 16, no. 5, pp. 943–948, April 2015.

[42] Minda, I., Ahmed, E., Sleziona, V., Richter, C., Beu, M., Falgenhauer, J., Miura, H., Schlettwein, D. and Schwoerer, H.: Identification of different pathways of electron injection in dye-sensitised solar cells of electrodeposited ZnO using an indoline sensitiser. *Physical Chemistry Chemical Physics*, vol. 18, no. 13, pp. 8938–8944, 2016.

[43] Smeigh, A.L., Le Pleux, L., Fortage, J., Pellegrin, Y., Blart, E., Odobel, F. and Hammarström, L.: Ultrafast recombination for NiO sensitized with a series of perylene imide sensitizers exhibiting Marcus normal behaviour. *Chemical Communications*, vol. 48, no. 5, pp. 678–680, December 2011.

[44] Kojima, A., Teshima, K., Shirai, Y. and Miyasaka, T.: Organometal Halide Perovskites as Visible-Light Sensitizers for Photovoltaic Cells. *Journal of the American Chemical Society*, vol. 131, no. 17, pp. 6050–6051, April 2009.

[45] Elumalai, N., Mahmud, M., Wang, D. and Uddin, A.: Perovskite Solar Cells: Progress and Advancements. *Energies*, vol. 9, no. 11, p. 861, October 2016.

[46] Stoumpos, C.C. and Kanatzidis, M.G.: Halide Perovskites: Poor Man's High-Performance Semiconductors. *Advanced Materials*, vol. 28, no. 28, pp. 5778–5793, July 2016.

[47] Herz, L.M.: Charge-Carrier Dynamics in Organic-Inorganic Metal Halide Perovskites. *Annual Review of Physical Chemistry*, vol. 67, pp. 65–89, May 2016.

[48] De Wolf, S., Holovsky, J., Moon, S.-J., Löper, P., Niesen, B., Ledinsky, M., Haug, F.-J., Yum, J.-H. and Ballif, C.: Organometallic Halide Perovskites: Sharp Optical Absorption Edge and Its Relation to Photovoltaic Performance. *The Journal of Physical Chemistry Letters*, vol. 5, no. 6, pp. 1035–1039, 2014.

[49] Leguy, A.M.A., Hu, Y., Campoy-Quiles, M., Alonso, M.I., Weber, O.J., Azarhoosh, P., van Schilfgaarde, M., Weller, M.T., Bein, T., Nelson, J., Docampo, P. and Barnes, P.R.F.: Reversible Hydration of $CH_3NH_3PbI_3$ in Films, Single Crystals, and Solar Cells. *Chemistry of Materials*, vol. 27, no. 9, pp. 3397–3407, May 2015.

[50] Sheng, R., Ho-Baillie, A., Huang, S., Chen, S., Wen, X., Hao, X. and Green, M.A.: Methylammonium Lead Bromide Perovskite-Based Solar Cells by Vapor-Assisted Deposition. *The Journal of Physical Chemistry C*, vol. 119, no. 7, pp. 3545–3549, 2015.

[51] Noh, J.H., Im, S.H., Heo, J.H., Mandal, T.N. and Seok, S.I.: Chemical Management for Col-

orful, Efficient, and Stable Inorganic-Organic Hybrid Nanostructured Solar Cells. *Nano Letters*, vol. 13, no. 4, pp. 1764–1769, April 2013.

[52] Dar, M.I., Arora, N., Gao, P., Ahmad, S., Grätzel, M. and Nazeeruddin, M.K.: Investigation Regarding the Role of Chloride in Organic-Inorganic Halide Perovskites Obtained from Chloride Containing Precursors. *Nano Letters*, vol. 14, no. 12, pp. 6991–6996, December 2014.

[53] Liu, J., Shirai, Y., Yang, X., Yue, Y., Chen, W., Wu, Y., Islam, A. and Han, L.: High-Quality Mixed-Organic-Cation Perovskites from a Phase-Pure Non-stoichiometric Intermediate $(FAI)_{1-x}$-PbI_2 for Solar Cells. *Advanced Materials*, vol. 27, no. 33, pp. 4918–4923, September 2015.

[54] Yang, W.S., Noh, J.H., Jeon, N.J., Kim, Y.C., Ryu, S., Seo, J. and Il Seok, S.: High-performance photovoltaic perovskite layers fabricated through intramolecular exchange. *Science*, vol. 348, no. 6240, pp. 1234–1237, June 2015.

[55] Jeon, N.J., Noh, J.H., Yang, W.S., Kim, Y.C., Ryu, S., Seo, J. and Il Seok, S.: Compositional engineering of perovskite materials for high-performance solar cells. *Nature*, vol. 517, no. 7535, pp. 476–480, January 2015.

[56] Eperon, G.E., Stranks, S.D., Menelaou, C., Johnston, M.B., Herz, L.M. and Snaith, H.J.: Formamidinium lead trihalide: a broadly tunable perovskite for efficient planar heterojunction solar cells. *Energy & Environmental Science*, vol. 7, no. 3, pp. 982–988, 2014.

[57] Bi, D., Tress, W., Dar, M.I., Gao, P., Luo, J., Renevier, C., Schenk, K., Abate, A., Giordano, F., Correa Baena, J.-P., Decoppet, J.-D., Zakeeruddin, S.M., Nazeeruddin, M.K., Grätzel, M. and Hagfeldt, A.: Efficient luminescent solar cells based on tailored mixed-cation perovskites. *Sci Adv*, vol. 2, no. 1, pp. 982–988, January 2016.

[58] Yi, C., Li, X., Luo, J., Zakeeruddin, S.M. and Grätzel, M.: Perovskite Photovoltaics with Outstanding Performance Produced by Chemical Conversion of Bilayer Mesostructured Lead Halide/TiO_2 Films. *Advanced Materials*, vol. 28, no. 15, pp. 2964–2970, 2016.

[59] Saliba, M., Matsui, T., Domanski, K., Seo, J.-Y., Ummadisingu, A., Zakeeruddin, S.M., Correa Baena, J.-P., Tress, W.R., Abate, A., Hagfeldt, A. and Grätzel, M.: Incorporation of rubidium cations into perovskite solar cells improves photovoltaic performance. *Science*, vol. 354, no. 6309, pp. 206–209, October 2016.

[60] Saliba, M., Matsui, T., Seo, J.-Y., Domanski, K., Correa Baena, J.-P., Nazeeruddin, M.K., Zakeeruddin, S.M., Tress, W., Abate, A., Hagfeldt, A. and Grätzel, M.: Cesium-containing triple cation perovskite solar cells: improved stability, reproducibility and high efficiency. *Energy & Environmental Science*, vol. 9, no. 6, pp. 1989–1997, 2016.

[61] Jaramillo-Quintero, O.A., Sanchez, R.S., Rincon, M. and Mora-Sero, I.: Bright Visible-Infrared Light Emitting Diodes Based on Hybrid Halide Perovskite with Spiro-OMeTAD as a Hole-Injecting Layer. *The Journal of Physical Chemistry Letters*, vol. 6, no. 10, pp. 1883–1890, May 2015.

[62] Wong, A.B., Lai, M., Eaton, S.W., Yu, Y., Lin, E., Dou, L., Fu, A. and Yang, P.: Growth and Anion Exchange Conversion of $CH_3NH_3PbX_3$ Nanorod Arrays for Light-Emitting Diodes. *Nano Letters*, vol. 15, no. 8, pp. 5519–5524, August 2015.

[63] Deschler, F., Price, M., Pathak, S., Klintberg, L.E., Jarausch, D.-D., Higler, R., Hüttner, S., Leijtens, T., Stranks, S.D., Snaith, H.J., Atatüre, M., Phillips, R.T. and Friend, R.H.: High Photoluminescence Efficiency and Optically Pumped Lasing in Solution-Processed Mixed Halide Perovskite Semiconductors. *The Journal of Physical Chemistry Letters*, vol. 5, no. 8, pp. 1421–1426, April 2014.

[64] Xing, G., Mathews, N., Lim, S.S., Yantara, N., Liu, X., Sabba, D., Grätzel, M., Mhaisalkar, S. and Sum, T.C.: Low-temperature solution-processed wavelength-tunable perovskites for lasing. *Nature materials*, vol. 13, no. 5, pp. 476–480, May 2014.

[65] Kagan, C.R., Mitzi, D.B. and Dimitrakopoulos, C.D.: Organic-Inorganic Hybrid Materials as Semiconducting Channels in Thin-Film Field-Effect Transistors. *Science*, vol. 286, no.

5441, pp. 945–947, October 1999.

[66] Mitzi, D.B., Dimitrakopoulos, C.D. and Kosbar, L.L.: Structurally Tailored Organic-Inorganic Perovskites: Optical Properties and Solution-Processed Channel Materials for Thin-Film Transistors. *Chemistry of Materials*, vol. 13, no. 10, pp. 3728–3740, June 2001.

[67] Mei, Y., Zhang, C., Vardeny, Z. and Jurchescu, O.: Electrostatic gating of hybrid halide perovskite field-effect transistors: balanced ambipolar transport at room-temperature. *MRS Communications*, vol. 5, no. 2, p. 297301, 2015.

[68] Dong, Q., Fang, Y., Shao, Y., Mulligan, P., Qiu, J., Cao, L. and Huang, J.: Electron-hole diffusion lengths $>175\mu$m in solution-grown $CH_3NH_3PbI_3$ single crystals. *Science*, vol. 347, no. 6225, pp. 967–970, February 2015.

[69] Chen, Y.-S., Manser, J.S. and Kamat, P.V.: All Solution-Processed Lead Halide Perovskite-$BiVO_4$Tandem Assembly for Photolytic Solar Fuels Production. *Journal of the American Chemical Society*, vol. 137, no. 2, pp. 974–981, January 2015.

[70] Wehrenfennig, C., Eperon, G.E., Johnston, M.B., Snaith, H.J. and Herz, L.M.: High Charge Carrier Mobilities and Lifetimes in Organolead Trihalide Perovskites. *Advanced Materials*, vol. 26, no. 10, pp. 1584–1589, March 2014.

[71] Motta, C., El-Mellouhi, F. and Sanvito, S.: Charge carrier mobility in hybrid halide perovskites. *Scientific reports*, vol. 5, no. 1, p. 506, 2015.

[72] Gonzalez-Pedro, V., Juarez-Perez, E.J., Arsyad, W.-S., Barea, E.M., Fabregat-Santiago, F., Mora-Sero, I. and Bisquert, J.: General Working Principles of $CH_3NH_3PbX_3$ Perovskite Solar Cells. *Nano Letters*, vol. 14, no. 2, pp. 888–893, January 2014.

[73] Stoumpos, C.C., Malliakas, C.D. and Kanatzidis, M.G.: Semiconducting Tin and Lead Iodide Perovskites with Organic Cations: Phase Transitions, High Mobilities, and Near-Infrared Photoluminescent Properties. *Inorganic Chemistry*, vol. 52, no. 15, pp. 9019–9038, July 2013.

[74] Lee, M.M., Teuscher, J., Miyasaka, T., Murakami, T.N. and Snaith, H.J.: Efficient Hybrid Solar Cells Based on Meso-Superstructured Organometal Halide Perovskites. *Science*, vol. 338, no. 6107, pp. 643–647, November 2012.

[75] Kim, H.-S., Lee, C.-R., Im, J.-H., Lee, K.-B., Moehl, T., Marchioro, A., Moon, S.-J., Humphry-Baker, R., Yum, J.-H., Moser, J.E., Grätzel, M. and Park, N.-G.: Lead Iodide Perovskite Sensitized All-Solid-State Submicron Thin Film Mesoscopic Solar Cell with Efficiency Exceeding 9%. *Scientific reports*, vol. 2, p. 591, August 2012.

[76] Liu, T., Chen, K., Hu, Q., Zhu, R. and Gong, Q.: Inverted Perovskite Solar Cells: Progresses and Perspectives. *Advanced Energy Materials*, vol. 6, no. 17, p. 1600457, September 2016.

[77] Yin, W., Pan, L., Yang, T. and Liang, Y.: Recent Advances in Interface Engineering for Planar Heterojunction Perovskite Solar Cells. *Molecules*, vol. 21, no. 7, p. 837, June 2016.

[78] Kim, H., Lim, K.-G. and Lee, T.-W.: Planar heterojunction organometal halide perovskite solar cells: roles of interfacial layers. *Energy & Environmental Science*, vol. 9, no. 1, pp. 12–30, January 2016.

[79] Chueh, C.-C., Li, C.-Z. and Jen, A.K.Y.: Recent progress and perspective in solution-processed Interfacial materials for efficient and stable polymer and organometal perovskite solar cells. *Energy & Environmental Science*, vol. 8, no. 4, pp. 1160–1189, April 2015.

[80] Miyata, A., Mitioglu, A., Plochocka, P., Portugall, O., Wang, J.T.-W., Stranks, S.D., Snaith, H.J. and Nicholas, R.J.: Direct Measurement of the Exciton Binding Energy and Effective Masses for Charge carriers in an Organic-Inorganic Tri-halide Perovskite. *Nature Physics*, vol. 7, pp. 582–587, April 2015.

[81] Edri, E., Kirmayer, S., Mukhopadhyay, S., Gartsman, K., Hodes, G. and Cahen, D.: Elucidating the charge carrier separation and working mechanism of $CH_3NH_3PbI_{3-x}Cl_x$ perovskite solar cells. *Nature Communications*, vol. 5, p. 3461, March 2014.

[82] Lin, Q., Armin, A., Nagiri, R.C.R. and Burn, P.L.: Electro-optics of perovskite solar cells. *Nature*, 2014.

[83] Tress, W., Marinova, N., Inganäs, O., Nazeeruddin, M.K., Zakeeruddin, S.M. and Grätzel, M.: Predicting the Open-Circuit Voltage of $CH_3NH_3PbI_3$ Perovskite Solar Cells Using Electroluminescence and Photovoltaic Quantum Efficiency Spectra: the Role of Radiative and Non-Radiative Recombination. *Advanced Energy Materials*, vol. 5, no. 3, February 2015.

[84] Marinova, N., Tress, W., Humphry-Baker, R., Dar, M.I., Bojinov, V., Zakeeruddin, S.M., Nazeeruddin, M.K. and Grätzel, M.: Light Harvesting and Charge Recombination in $CH_3NH_3PbI_3$ Perovskite Solar Cells Studied by Hole Transport Layer Thickness Variation. *ACS Nano*, vol. 9, no. 4, pp. 4200–4209, March 2015.

[85] Wetzelaer, G.J.A.H., Scheepers, M., Sempere, A.M., Momblona, C., Ávila, J. and Bolink, H.J.: Trap-Assisted Non-Radiative Recombination in Organic-Inorganic Perovskite Solar Cells. *Advanced Materials*, vol. 27, no. 11, pp. 1837–1841, March 2015.

[86] Jeon, N.J., Noh, J.H., Kim, Y.C., Yang, W.S. and Ryu, S.: Solvent engineering for high-performance inorganic-organic hybrid perovskite solar cells. *Nature*, 2014.

[87] Zheng, X., Chen, B., Wu, C. and Priya, S.: Room temperature fabrication of $CH_3NH_3PbBr_3$ by anti-solvent assisted crystallization approach for perovskite solar cells with fast response and small J-V hysteresis. *Nano Energy*, vol. 17, pp. 269–278, October 2015.

[88] Tiep, N.H., Ku, Z. and Fan, H.J.: Recent Advances in Improving the Stability of Perovskite Solar Cells. *Advanced Energy Materials*, vol. 6, no. 3, February 2016.

[89] Navas, J., Sánchez-Coronilla, A., Gallardo, J.J., Martín, E.I., Hernández, N.C., Alcántara, R., Fernández-Lorenzo, C. and Martín-Calleja, J.: Revealing the role of Pb^{2+} in the stability of organic-inorganic hybrid perovskite $CH_3NH_3Pb_{1-x}Cd_xI_3$: an experimental and theoretical study. *Physical Chemistry Chemical Physics*, vol. 17, no. 37, pp. 23886–23896, September 2015.

[90] Qin, C., Matsushima, T., Fujihara, T., Potscavage, W.J. and Adachi, C.: Degradation Mechanisms of Solution-Processed Planar Perovskite Solar Cells: Thermally Stimulated Current Measurement for Analysis of Carrier Traps. *Advanced Materials*, vol. 28, no. 3, pp. 466–471, November 2015.

[91] Li, X., Dar, M.I., Yi, C., Luo, J., Tschumi, M., Zakeeruddin, S.M., Nazeeruddin, M.K., Han, H. and Grätzel, M.: Improved performance and stability of perovskite solar cells by crystal crosslinking with alkylphosphonic acid ω-ammonium chlorides. *Nature Chemistry*, vol. 7, no. 9, pp. 703–711, September 2015.

[92] Lee, B., Stoumpos, C.C., Zhou, N., Hao, F., Malliakas, C., Yeh, C.-Y., Marks, T.J., Kanatzidis, M.G. and Chang, R.P.H.: Air-Stable Molecular Semiconducting Iodosalts for Solar Cell Applications: Cs_2SnI_6 as a Hole Conductor. *Journal of the American Chemical Society*, vol. 136, no. 43, pp. 15379–15385, October 2014.

[93] Binek, A., Petrus, M.L., Huber, N., Bristow, H., Hu, Y., Bein, T. and Docampo, P.: Recycling Perovskite Solar Cells To Avoid Lead Waste. *ACS Applied Materials & Interfaces*, vol. 8, no. 20, pp. 12881–12886, May 2016.

[94] Fabini, D.: Quantifying the Potential for Lead Pollution from Halide Perovskite Photovoltaics. *The Journal of Physical Chemistry Letters*, vol. 6, no. 18, pp. 3546–3548, September 2015.

[95] Gong, J., Darling, S.B. and You, F.: Perovskite photovoltaics: life-cycle assessment of energy and environmental impacts. *Energy & Environmental Science*, vol. 8, no. 7, pp. 1953–1968, July 2015.

[96] Espinosa, N., Serrano-Luján, L., Urbina, A. and Krebs, F.C.: Solution and vapour deposited lead perovskite solar cells: Ecotoxicity from a life cycle assessment perspective. *Solar Energy Materials and Solar Cells*, vol. 137, pp. 303–310, June 2015.

[97] Hailegnaw, B., Kirmayer, S., Edri, E., Hodes, G. and Cahen, D.: Rain on Methylammonium Lead Iodide Based Perovskites: Possible Environmental Effects of Perovskite Solar Cells. *The Journal of Physical Chemistry Letters*, vol. 6, no. 9, pp. 1543–1547, April 2015.

[98] Chen, P.-Y., Qi, J., Klug, M.T., Dang, X., Hammond, P.T. and Belcher, A.M.: Environmentally responsible fabrication of efficient perovskite solar cells from recycled car batteries. *Energy & Environmental Science*, vol. 7, no. 11, pp. 3659–3665, October 2014.

[99] Even, J., Pedesseau, L. and Katan, C.: Analysis of Multivalley and Multibandgap Absorption and Enhancement of Free Carriers Related to Exciton Screening in Hybrid Perovskites. *The Journal of Physical Chemistry C*, vol. 118, no. 22, pp. 11566–11572, June 2014.

[100] Even, J., Pedesseau, L., Katan, C., Kepenekian, M., Lauret, J.-S., Sapori, D. and Deleporte, E.: Solid-State Physics Perspective on Hybrid Perovskite Semiconductors. *The Journal of Physical Chemistry C*, vol. 119, no. 19, pp. 10161–10177, April 2015.

[101] Im, J., Stoumpos, C.C., Jin, H., Freeman, A.J. and Kanatzidis, M.G.: Antagonism between Spin-Orbit Coupling and Steric Effects Causes Anomalous Band Gap Evolution in the Perovskite Photovoltaic Materials $CH_3NH_3Sn_{1-x}Pb_xI_3$. *The Journal of Physical Chemistry Letters*, vol. 6, no. 17, pp. 3503–3509, September 2015.

[102] Stroppa, A., Di Sante, D., Barone, P., Bokdam, M., Kresse, G., Franchini, C., Whangbo, M.-H. and Picozzi, S.: Tunable ferroelectric polarization and its interplay with spin-orbit coupling in tin iodide perovskites. *Nature Communications*, vol. 5, p. 5900, December 2014.

[103] Filip, M.R. and Giustino, F.: GW quasiparticle band gap of the hybrid organic-inorganic perovskite $CH_3NH_3PbI_3$: Effect of spin-orbit interaction, semicore electrons, and self-consistency. *Physical Review B*, vol. 90, no. 24, p. 245145, December 2014.

[104] Mosconi, E., Amat, A., Nazeeruddin, M.K., Grätzel, M. and De Angelis, F.: First-Principles Modeling of Mixed Halide Organometal Perovskites for Photovoltaic Applications. *The Journal of Physical Chemistry C*, vol. 117, no. 27, pp. 13902–13913, July 2013.

[105] Baikie, T., Fang, Y., Kadro, J.M., Schreyer, M., Wei, F., Mhaisalkar, S.G., Grätzel, M. and White, T.J.: Synthesis and crystal chemistry of the hybrid perovskite $(CH_3NH_3)PbI_3$ for solid-state sensitised solar cell applications. *Journal of Materials Chemistry A*, vol. 1, no. 18, pp. 5628–5641, April 2013.

[106] Even, J., Pedesseau, L., Jancu, J.-M. and Katan, C.: Importance of Spin-Orbit Coupling in Hybrid Organic/Inorganic Perovskites for Photovoltaic Applications. *The Journal of Physical Chemistry Letters*, vol. 4, no. 17, pp. 2999–3005, September 2013.

[107] Xing, G., Mathews, N., Sun, S., Lim, S.S., Lam, Y.M., Grätzel, M., Mhaisalkar, S. and Sum, T.C.: Long-Range Balanced Electron- and Hole-Transport Lengths in Organic-Inorganic $CH_3NH_3PbI_3$. *Science*, vol. 342, no. 6156, pp. 344–347, October 2013.

[108] Kawai, H., Giorgi, G., Marini, A. and Yamashita, K.: The Mechanism of Slow Hot-Hole Cooling in Lead-Iodide Perovskite: First-Principles Calculation on Carrier Lifetime from Electron-Phonon Interaction. *Nano Letters*, vol. 15, no. 5, pp. 3103–3108, April 2015.

[109] Manser, J.S. and Kamat, P.V.: Band filling with free charge carriers in organometal halide perovskites. *Nature Photonics*, vol. 8, no. 9, pp. 737–743, September 2014.

[110] Stamplecoskie, K.G., Manser, J.S. and Kamat, P.V.: Dual nature of the excited state in organic-inorganic lead halide perovskites. *Energy & Environmental Science*, vol. 8, no. 1, pp. 208–215, December 2014.

[111] Christians, J.A., Manser, J.S. and Kamat, P.V.: Multifaceted Excited State of $CH_3NH_3PbI_3$. Charge Separation, Recombination, and Trapping. *The Journal of Physical Chemistry Letters*, vol. 6, no. 11, pp. 2086–2095, May 2015.

[112] Chen, K., Barker, A.J., Morgan, F.L.C., Halpert, J.E. and Hodgkiss, J.M.: Effect of Carrier Thermalization Dynamics on Light Emission and Amplification in Organometal Halide Perovskites. *The Journal of Physical Chemistry Letters*, vol. 6, no. 1, pp. 153–158, December 2014.

[113] Trinh, M.T., Wu, X., Niesner, D. and Zhu, X.Y.: Many-body interactions in photo-excited

lead iodide perovskite. *Journal of Materials Chemistry A*, vol. 3, no. 17, pp. 9285–9290, April 2015.

[114] Hsu, H.Y., Wang, C.Y., Fathi, A., Shiu, J.W., Chung, C.C., Shen, P.S., Guo, T.F., Chen, P., Lee, Y.P. and Diau, E.W.G.: Femtosecond Excitonic Relaxation Dynamics of Perovskite on Mesoporous Films of Al_2O_3 and NiO Nanoparticles. *Angewandte Chemie*, vol. 126, no. 35, pp. 9493–9496, August 2014.

[115] Wang, L., McCleese, C., Kovalsky, A., Zhao, Y. and Burda, C.: Femtosecond Time-Resolved Transient Absorption Spectroscopy of $CH_3NH_3PbI_3$ Perovskite Films: Evidence for Passivation Effect of PbI_2. *Journal of the American Chemical Society*, vol. 136, no. 35, pp. 12205–12208, September 2014.

[116] Yang, Y., Ostrowski, D.P., France, R.M., Zhu, K., van de Lagemaat, J., Luther, J.M. and Beard, M.C.: Observation of a hot-phonon bottleneck in lead-iodide perovskites. *Nature Photonics*, vol. 10, no. 1, pp. 53–59, January 2016.

[117] Price, M.B., Butkus, J., Jellicoe, T.C., Sadhanala, A., Briane, A., Halpert, J.E., Broch, K., Hodgkiss, J.M., Friend, R.H. and Deschler, F.: Hot-carrier cooling and photoinduced refractive index changes in organic-inorganic lead halide perovskites. *Nature Communications*, vol. 6, p. 8420, September 2015.

[118] Grancini, G., Kandada, A.R.S., Frost, J.M., Barker, A.J., De Bastiani, M., Gandini, M., Marras, S., Lanzani, G., Walsh, A. and Petrozza, A.: Role of microstructure in the electron-hole interaction of hybrid lead halide perovskites. *Nature Photonics*, vol. 9, no. 10, pp. 695–701, October 2015.

[119] Klimov, V., Bolivar, P.H. and Kurz, H.: Hot-phonon effects in femtosecond luminescence spectra of electron-hole plasmas in CdS. *Physical Review B*, vol. 52, no. 7, pp. 4728–4731, August 1995.

[120] Yong, C.K., Wong-Leung, J., Joyce, H.J., Lloyd-Hughes, J., Gao, Q., Tan, H.H., Jagadish, C., Johnston, M.B. and Herz, L.M.: Direct Observation of Charge-Carrier Heating at WZ-ZB InP Nanowire Heterojunctions. *Nano Letters*, vol. 13, no. 9, pp. 4280–4287, August 2013.

[121] Hegen, T.: Stroboscopic gymnast. Photograph, 2017. Reprinted with permission from the photographer (Copyright 2017).
Available at: http://tomhegen.de/fotodesign/stroboscopic-gymnast/

[122] Megerle, U., Pugliesi, I., Schriever, C., Sailer, C.F. and Riedle, E.: Sub-50 fs broadband absorption spectroscopy with tunable excitation: putting the analysis of ultrafast molecular dynamics on solid ground. *Applied Physics B*, vol. 96, no. 2-3, pp. 215–231, June 2009.

[123] Riedle, E., Beutter, M., Lochbrunner, S., Piel, J., Schenkl, S., Spörlein, S. and Zinth, W.: Generation of 10 to 50fs pulses tunable through all of the visible and the NIR. *Applied Physics B*, vol. 71, no. 3, pp. 457–465, February 2000.

[124] Ahmed, E.: *A Near Infrared Femtosecond Laser Source for Observation of Charge Transfer Processes in Semiconductors*. Master's thesis, Stellenbosch University, March 2017.

[125] Marcus, R.A. and Sutin, N.: Electron transfers in chemistry and biology. *Biochimica et Biophysica Acta (BBA) - Reviews on Bioenergetics*, vol. 811, no. 3, pp. 265–322, August 1985.

[126] Yoshida, T., Zhang, J., Komatsu, D., Sawatani, S., Minoura, H., Pauport, T., Lincot, D., Oekermann, T., Schlettwein, D., Tada, H., Wöhrle, D., Funabiki, K., Matsui, M., Miura, H. and Yanagi, H.: Electrodeposition of Inorganic/Organic Hybrid Thin Films. *Advanced Functional Materials*, vol. 19, no. 1, pp. 17–43, January 2009.

[127] Zhang, J., Sun, L., Ichinose, K., Funabiki, K. and Yoshida, T.: Effect of anchoring groups on electrochemical self-assembly of ZnO/xanthene dye hybrid thin films. *Physical Chemistry Chemical Physics*, vol. 12, no. 35, p. 10494, 2010.

[128] Ichinose, K., Kimikado, Y. and Yoshida, T.: The Effect of Pre-treatments of F-Doped SnO_2 Substrates for Cathodic Nucleation of ZnO Crystals in Aqueous $ZnCl_2$ Solution with Dissolved O_2. *Electrochemistry*, vol. 79, no. 3, pp. 146–155, 2011.

[129] Shi, D., Qin, X., Li, Y., He, Y., Zhong, C., Pan, J., Dong, H., Xu, W., Li, T., Hu, W., Bredas, J.L. and Bakr, O.M.: Spiro-OMeTAD single crystals: Remarkably enhanced charge-carrier transport via mesoscale ordering. *Science Advances*, vol. 2, no. 4, April 2016.

[130] Fantacci, S., De Angelis, F., Nazeeruddin, M.K. and Grätzel, M.: Electronic and Optical Properties of the Spiro-MeOTAD Hole Conductor in Its Neutral and Oxidized Forms: A DFT/TDDFT Investigation. *The Journal of Physical Chemistry C*, vol. 115, no. 46, pp. 23126–23133, November 2011.

[131] Anderson, N.A., Ai, X. and Lian, T.: Electron Injection Dynamics from Ru Polypyridyl Complexes to ZnO Nanocrystalline Thin Films. *The Journal of Physical Chemistry B*, vol. 107, no. 51, pp. 14414–14421, December 2003.

[132] Falgenhauer, J., Richter, C., Miura, H. and Schlettwein, D.: Stable Sensitization of ZnO by Improved Anchoring of Indoline Dyes. *ChemPhysChem*, vol. 13, no. 12, pp. 2893–2897, June 2012.

[133] Snaith, H.J., Humphry-Baker, R., Chen, P., Cesar, I., Zakeeruddin, S.M. and Grätzel, M.: Charge collection and pore filling in solid-state dye-sensitized solar cells. *Nanotechnology*, vol. 19, no. 42, September 2008.

[134] Cho, K.T., Paek, S., Grancini, G., Roldán-Carmona, C., Gao, P., Lee, Y. and Nazeeruddin, M.K.: Highly efficient perovskite solar cells with a compositionally engineered perovskite/hole transporting material interface. *Energy Environ. Sci.*, vol. 10, no. 2, pp. 621–627, 2017.

[135] Hoke, E.T., Slotcavage, D.J., Dohner, E.R., Bowring, A.R., Karunadasa, H.I. and McGehee, M.D.: Reversible photo-induced trap formation in mixed-halide hybrid perovskites for photovoltaics. *Chem. Sci.*, vol. 6, no. 1, pp. 613–617, 2015.

[136] Motta, C., El-Mellouhi, F., Kais, S., Tabet, N., Alharbi, F. and Sanvito, S.: Revealing the role of organic cations in hybrid halide perovskites $CH_3NH_3PbI_3$. *Nature Communications*, vol. 6, no. 7026, October 2014.

[137] Endres, J., Egger, D.A., Kulbak, M., Kerner, R.A., Zhao, L., Silver, S.H., Hodes, G., Rand, B.P., Cahen, D., Kronik, L. and Kahn, A.: Valence and Conduction Band Densities of States of Metal Halide Perovskites: A Combined Experimental-Theoretical Study. *The Journal of Physical Chemistry Letters*, vol. 7, no. 14, pp. 2722–2729, July 2016.

[138] Burschka, J., Pellet, N., Moon, S.-J., Humphry-Baker, R., Gao, P., Nazeeruddin, M.K. and Grätzel, M.: Sequential deposition as a route to high-performance perovskite-sensitized solar cells. *Nature*, vol. 499, no. 7458, pp. 316–319, July 2013.

[139] Liu, M., Johnston, M.B. and Snaith, H.J.: Efficient planar heterojunction perovskite solar cells by vapour deposition. *Nature*, vol. 501, no. 7467, pp. 395–398, September 2013.

[140] Ruess, R., Benfer, F., Böcher, F., Stumpp, M. and Schlettwein, D.: Stabilization of Organic-Inorganic Perovskite Layers by Partial Substitution of Iodide by Bromide in Methylammonium Lead Iodide. *ChemPhysChem*, vol. 17, no. 10, pp. 1505–1511, March 2016.

[141] Lee, Y.H., Luo, J., Son, M.-K., Gao, P., Cho, K.T., Seo, J., Zakeeruddin, S.M., Grätzel, M. and Nazeeruddin, M.K.: Enhanced Charge Collection with Passivation Layers in Perovskite Solar Cells. *Advanced Materials*, vol. 28, no. 20, pp. 3966–3972, March 2016.

[142] Stranks, S.D., Wood, S.M., Wojciechowski, K., Deschler, F., Saliba, M., Khandelwal, H., Patel, J.B., Elston, S.J., Herz, L.M., Johnston, M.B., Schenning, A.P.H.J., Debije, M.G., Riede, M.K., Morris, S.M. and Snaith, H.J.: Enhanced Amplified Spontaneous Emission in Perovskites Using a Flexible Cholesteric Liquid Crystal Reflector. *Nano Letters*, vol. 15, no. 8, pp. 4935–4941, August 2015.

[143] Shah, J.: *Ultrafast Spectroscopy of Semiconductors and Semiconductor Nanostructures*, vol. 2. Springer, 1999.

[144] Saba, M., Quochi, F., Mura, A. and Bongiovanni, G.: Excited State Properties of Hybrid Perovskites. *Accounts of Chemical Research*, vol. 49, no. 1, pp. 166–173, January 2016.

[145] Wehrenfennig, C., Liu, M., Snaith, H.J., Johnston, M.B. and Herz, L.M.: Charge-

carrier dynamics in vapour-deposited films of the organolead halide perovskite $CH_3NH_3PbI_{3-x}Cl_x$. *Energy & Environmental Science*, vol. 7, no. 7, pp. 2269–2275, June 2014.

[146] Johnston, M.B. and Herz, L.M.: Hybrid Perovskites for Photovoltaics: Charge-Carrier Recombination, Diffusion, and Radiative Efficiencies. *Accounts of Chemical Research*, vol. 49, no. 1, pp. 146–154, December 2015.

[147] Saba, M., Cadelano, M., Marongiu, D., Chen, F., Sarritzu, V., Sestu, N., Figus, C., Aresti, M., Piras, R., Geddo Lehmann, A., Cannas, C., Musinu, A., Quochi, F., Mura, A. and Bongiovanni, G.: Correlated electron-hole plasma in organometal perovskites. *Nature Communications*, vol. 5, p. 5049, September 2014.

[148] Piatkowski, P., Cohen, B., Kazim, S., Ahmad, S. and Douhal, A.: How photon pump fluence changes the charge carrier relaxation mechanism in an organic-inorganic hybrid lead triiodide perovskite. *Physical Chemistry Chemical Physics*, vol. 18, no. 39, pp. 27090–27101, 2016.

[149] de Quilettes, D.W., Vorpahl, S.M., Stranks, S.D., Nagaoka, H., Eperon, G.E., Ziffer, M.E., Snaith, H.J. and Ginger, D.S.: Impact of microstructure on local carrier lifetime in perovskite solar cells. *Science*, vol. 348, no. 6235, pp. 683–686, May 2015.

[150] Stranks, S.D., Eperon, G.E., Grancini, G., Menelaou, C., Alcocer, M.J.P., Leijtens, T., Herz, L.M., Petrozza, A. and Snaith, H.J.: Electron-Hole Diffusion Lengths Exceeding 1 Micrometer in an Organometal Trihalide Perovskite Absorber. *Science*, vol. 342, no. 6156, pp. 341–344, October 2013.

[151] Nie, W., Tsai, H., Asadpour, R., Blancon, J.-C., Neukirch, A.J., Gupta, G., Crochet, J.J., Chhowalla, M., Tretiak, S., Alam, M.A., Wang, H.-L. and Mohite, A.D.: High-efficiency solution-processed perovskite solar cells with millimeter-scale grains. *Science*, vol. 347, no. 6221, pp. 522–525, January 2015.

[152] Shi, D., Adinolfi, V., Comin, R., Yuan, M., Alarousu, E., Buin, A., Chen, Y., Hoogland, S., Rothenberger, A., Katsiev, K., Losovyj, Y., Zhang, X., Dowben, P.A., Mohammed, O.F., Sargent, E.H. and Bakr, O.M.: Low trap-state density and long carrier diffusion in organolead trihalide perovskite single crystals. *Science*, vol. 347, no. 6221, pp. 519–522, January 2015.

[153] Zhou, H., Chen, Q., Li, G., Luo, S., Song, T.-B., Duan, H.-S., Hong, Z., You, J., Liu, Y. and Yang, Y.: Interface engineering of highly efficient perovskite solar cells. *Science*, vol. 345, no. 6196, pp. 542–546, August 2014.

[154] Yamada, Y., Nakamura, T., Endo, M., Wakamiya, A. and Kanemitsu, Y.: Photocarrier Recombination Dynamics in Perovskite $CH_3NH_3PbI_3$ for Solar Cell Applications. *Journal of the American Chemical Society*, vol. 136, no. 33, pp. 11610–11613, August 2014.

[155] Milot, R.L., Eperon, G.E., Snaith, H.J., Johnston, M.B. and Herz, L.M.: Temperature-Dependent Charge-Carrier Dynamics in $CH_3NH_3PbI_3$ Perovskite Thin Films. *Advanced Functional Materials*, vol. 25, no. 39, pp. 6218–6227, October 2015.

[156] Savenije, T.J., Ponseca Jr., C.S., Kunneman, L., Abdellah, M., Zheng, K., Tian, Y., Zhu, Q., Canton, S.E., Scheblykin, I.G., Pullerits, T., Yartsev, A. and Sundström, V.: Thermally Activated Exciton Dissociation and Recombination Control the Carrier Dynamics in Organometal Halide Perovskite. *The Journal of Physical Chemistry Letters*, vol. 5, no. 13, pp. 2189–2194, July 2014.

[157] D'Innocenzo, V., Kandada, A.R.S., De Bastiani, M., Gandini, M. and Petrozza, A.: Tuning the Light Emission Properties by Band Gap Engineering in Hybrid Lead Halide Perovskite. *Journal of the American Chemical Society*, vol. 136, no. 51, pp. 17730–17733, December 2014.

[158] Guo, Z., Manser, J.S., Wan, Y., Kamat, P.V. and Huang, L.: Spatial and temporal imaging of long-range charge transport in perovskite thin films by ultrafast microscopy. *Nature Communications*, vol. 6, p. 7471, June 2015.

[159] Paulke, A., Stranks, S., Kniepert, J., Kurpiers, J., Wolff, C., Schön, N., Snaith, H., Brenner, T. and Neher, D.: Charge carrier recombination dynamics in perovskite and polymer solar cells. *Applied Physics Letters*, vol. 108, no. 113505, 2016.

[160] Svantesson, K.G. and Nilsson, N.G.: The temperature dependence of the Auger recombination coefficient of undoped silicon. *Journal of Physics C: Solid State Physics*, vol. 12, no. 23, pp. 5111–5120, February 2001.

[161] Kioupakis, E., Yan, Q., Steiauf, D. and Van de Walle, C.G.: Temperature and carrier-density dependence of Auger and radiative recombination in nitride optoelectronic devices. *New Journal of Physics*, vol. 15, no. 12, December 2013.

[162] Li, S.S.: *Semiconductor Physical Electronics*. Springer US, Boston, MA, 1993.

[163] Hader, J., Moloney, J.V. and Koch, S.W.: Supression of carrier recombination in semiconductor lasers by phase-space filling. *Applied Physics Letters*, vol. 87, no. 20, November 2005.

[164] Marchioro, A., Teuscher, J., Friedrich, D. and Kunst, M.: Unravelling the mechanism of photoinduced charge transfer processes in lead iodide perovskite solar cells. *Nature*, 2014.

[165] Xu, J., Buin, A., Ip, A.H., Li, W., Voznyy, O., Comin, R., Yuan, M., Jeon, S., Ning, Z., McDowell, J.J., Kanjanaboos, P., Sun, J.-P., Lan, X., Quan, L.N., Kim, D.H., Hill, I.G., Maksymovych, P. and Sargent, E.H.: Perovskite-fullerene hybrid materials suppress hysteresis in planar diodes. *Nature Communications*, vol. 6, p. 7081, May 2015.